

# Search for the Supersymmetric Partner to the Top Quark using Recoils Against Strong Initial State Radiation

A DISSERTATION PRESENTED  
BY  
SIYUAN SUN  
TO  
THE DEPARTMENT OF PHYSICS

IN PARTIAL FULFILLMENT OF THE REQUIREMENTS  
FOR THE DEGREE OF  
DOCTOR OF PHILOSOPHY  
IN THE SUBJECT OF  
PHYSICS

HARVARD UNIVERSITY  
CAMBRIDGE, MASSACHUSETTS  
MAY 2017

©2014 – SIYUAN SUN  
ALL RIGHTS RESERVED.

# Search for the Supersymmetric Partner to the Top Quark using Recoils Against Strong Initial State Radiation

## ABSTRACT

The ATLAS experiment at Large Hadron Collider (LHC) searches for experimental evidence of many new beyond the standard model physics at the TeV scale. As we collect more data at the LHC we continue to extend our sensitivity to these new phenomenon, particularly probing increasingly more massive new particles. Despite this progress there are still regions of parameter space where constraints remain weak. One common cause of this lack of sensitivity is because the new particle has a very small mass splitting between it and its decay products. The particle then has little energy left over to give momenta to its decay products and the low momenta decay products are difficult to experimentally detect. These regions of small mass splitting are called *compressed* regions. We are able to gain sensitivity to these difficult regions by searching for new particles produced in conjunction with strong initial state radiation (ISR). The strong initial state radiation boosts the new particle's decay products and gives them momentum.

This thesis covers the search for the supersymmetric partner to the top quark (stop) in the region when the stop and its decay products are nearly degenerate in mass. No searches prior to 2016 was sensitive to this region. We were able to exclude stops up to a mass of 525 GeV in this region with the 2015 and 2016 ATLAS dataset. I will demonstrate a new and more accurate technique for identifying

whole initial state radiation systems instead of a single ISR jet. As the LHC provides more data and traditional search methods rule out parameter space at higher masses, it becomes more important that we also gain sensitivity to these compressed regions that are still unconstrained at low masses. I will show that this initial state radiation identification technique is completely generalizable and useful for many other searches that target small mass splittings.

# Contents

o	INTRODUCTION	I
1	THEORETICAL MOTIVATION	8
1.1	The Standard Model . . . . .	8
1.2	Introduction to Super-Symmetry . . . . .	II
2	EXPERIMENTAL APPARATUS	16
2.1	The CERN Accelerator Complex and the Large Hadron Collider . . . . .	17
2.2	The ATLAS Detector . . . . .	20
2.2.1	Inner Detector . . . . .	23
2.2.2	The Calorimeter . . . . .	27
2.2.3	The Muon Spectrometer . . . . .	32
3	OBJECT RECONSTRUCTION AT ATLAS	37
3.1	Inner Detector Track Reconstruction . . . . .	37
3.2	Vertex Reconstruction . . . . .	39
3.3	Hadronic Jets . . . . .	41
3.3.1	Hadronic Jet Reconstruction . . . . .	41
3.3.2	Jet Calibration and Systematics . . . . .	43
3.3.3	Pileup Jet Rejection and Jet Vertex Tagger . . . . .	46
3.3.4	Jet Quality and Jet Cleaning . . . . .	48
3.3.5	Identifying Jets Originating from Heavy Flavor Hadrons . . . . .	50
3.4	Electron and Photons . . . . .	52
3.4.1	Electron and Photon Reconstruction . . . . .	52
3.4.2	Electron Identification and Quality . . . . .	54
3.4.3	Photon Identification and Quality . . . . .	55
3.4.4	Electron and Photon Energy Calibration . . . . .	55
3.5	Muons . . . . .	57
3.5.1	Muon Inner Detector and Muon Spectrometer Track Reconstruction . .	57
3.5.2	Muon Combined Reconstruction . . . . .	59
3.5.3	Muon Quality . . . . .	60
3.5.4	Muon Reconstruction Efficiency and Momentum Calibration . . . . .	62
3.6	Missing Transverse Momentum . . . . .	65
3.6.1	$E_T^{\text{miss}}$ Reconstruction . . . . .	66

3.6.2	Track $E_T^{\text{miss}}$ Reconstruction . . . . .	67
3.6.3	$E_T^{\text{miss}}$ Performance . . . . .	68
<b>4</b>	<b>TRIGGER</b>	<b>70</b>
4.1	Level 1 $E_T^{\text{miss}}$ trigger . . . . .	72
4.2	HLT $E_T^{\text{miss}}$ trigger . . . . .	72
4.3	Improvements to the $E_T^{\text{miss}}$ Trigger in Run 2 . . . . .	74
<b>5</b>	<b>PHYSICS OBJECT DEFINITIONS</b>	<b>76</b>
5.1	Electron Definition . . . . .	78
5.2	Muon Definition . . . . .	79
5.3	Jet Definitions . . . . .	80
5.3.1	Calorimeter Jets . . . . .	80
5.3.2	$b$ -tagged Jets . . . . .	81
5.4	Photon Definition . . . . .	82
5.5	$E_T^{\text{miss}}$ Definitions . . . . .	83
5.5.1	Calorimeter-based $E_T^{\text{miss}}$ . . . . .	83
5.5.2	Track-based $E_T^{\text{miss}}$ . . . . .	83
5.6	Resolving overlapping objects . . . . .	84
<b>6</b>	<b>MONTE CARLO SIMULATION OF PHYSICS PROCESSES AT ATLAS</b>	<b>85</b>
6.1	Signal Monte Carlo Generation . . . . .	86
6.2	SM Background Monte Carlo Generation . . . . .	88
6.2.1	Standard Model $t\bar{t}$ Monte Carlo Generation . . . . .	88
6.2.2	Standard Model Single Top Monte Carlo Generation . . . . .	90
6.2.3	Standard Model $W + \text{jets}$ and $Z + \text{jets}$ Monte Carlo Generation . . . . .	92
6.2.4	Standard Model $t\bar{t}+V$ Monte Carlo Generation . . . . .	92
6.2.5	Standard Model $t\bar{t} + \gamma$ Monte Carlo Generation . . . . .	93
6.2.6	Standard Model Diboson Monte Carlo Generation . . . . .	93
6.3	Detector Simulation . . . . .	93
6.4	Pile-Up Simulation . . . . .	94
<b>7</b>	<b>GENERAL ANALYSIS STRATEGY</b>	<b>95</b>
7.1	General R-Parity Conserving SUSY Search Strategy . . . . .	95
7.2	General Strategies in Compressed Regions . . . . .	97
<b>8</b>	<b>RECURSIVE JIGSAW RECONSTRUCTION</b>	<b>101</b>
8.1	Introduction to Recursive Jigsaw Algorithm on Events with $E_T^{\text{miss}}$ . . . . .	101
8.2	Recursive Jigsaw Method of Identifying Initial State Radiation . . . . .	103
8.3	Performance of Initial State Radiation Identification Algorithm . . . . .	105
8.4	Kinematic Variables of Initial State Radiation and Sparticle Systems . . . . .	107

<b>9</b>	<b>COLLISION DATA SAMPLES</b>	<b>109</b>
9.1	Data Periods and Good Run List . . . . .	109
<b>10</b>	<b>EVENT PRESELECTION</b>	<b>112</b>
10.1	Zero Lepton Pre-Selection . . . . .	114
10.2	One Lepton Pre-Selection . . . . .	115
<b>II</b>	<b>SIGNAL REGION DEFINITION</b>	<b>117</b>
II.1	Physical Intuition on how Signal Region Selections Reject SM Background . . . . .	118
II.2	Signal Region Kinematic Selection . . . . .	123
II.3	Signal Region Expected Yields and Kinematic Distributions . . . . .	126
II.4	Signal Region Background Composition . . . . .	126
<b>12</b>	<b>STANDARD MODEL BACKGROUNDS</b>	<b>130</b>
12.1	Common Background Estimation and Validation Techniques . . . . .	130
12.2	Dominant Background: Standard Model $t\bar{t}$ . . . . .	133
12.2.1	Two Kinematically Distinct Populations of $t\bar{t}$ . . . . .	133
12.2.2	Predicting the amount of $t\bar{t}$ in Signal Region using a One Lepton Control Region . . . . .	135
12.2.3	Validating $t\bar{t}$ Predictions in Signal Region using a Zero Lepton Validation Region . . . . .	140
12.3	Subdominant Backgrounds . . . . .	144
12.3.1	Standard Model W+Jets . . . . .	144
12.3.2	Standard Model Single Top . . . . .	146
12.3.3	Standard Model $t\bar{t}+Z$ . . . . .	151
12.3.4	Standard Model Z+Jets . . . . .	155
12.3.5	Standard Model Diboson . . . . .	155
12.3.6	Standard Model QCD Multijet and all Hadronic $t\bar{t}$ . . . . .	155
<b>13</b>	<b>SYSTEMATIC UNCERTAINTIES</b>	<b>162</b>
13.0.1	Experimental Uncertainties . . . . .	166
13.0.2	Theoretical Uncertainties . . . . .	172
<b>14</b>	<b>STATISTICAL ANALYSIS</b>	<b>180</b>
14.1	Introduction to Log Likelihood Fitting . . . . .	180
14.2	Overview of Fitting to Control Regions and Signal Regions . . . . .	183
14.3	Parameterization of Systematics as Gaussian Constraints . . . . .	186
14.4	Background Only Fit and Background Estimation . . . . .	187
14.5	Exclusion Fit and Exclusion Limit Calculation . . . . .	188
14.6	Discovery Fit and Discovery Significance Calculation . . . . .	189

15	RESULTS	191
16	INTERPRETATION OF RESULTS	195
17	CONCLUSION	200
APPENDIX A SANITY CHECKS		204
REFERENCES		209



# Acknowledgments

,

# 0

## Introduction

The Standard Model of Elementary Particles (SM) provides a concrete description of the dynamics and interactions of all known elementary particles with the exception of gravity. In the SM, matter is composed of three generation of fermions with spin  $1/2$  while interactions are governed by gauge symmetries and mediated by spin  $1$  gauge bosons.

The last piece of the SM, the Higgs boson was discovered in 2012 at the large hadron collider. The

complex scalar Higgs field spontaneously break the electroweak (EW) symmetry by acquiring a vacuum expectation value (VEV). This process of electroweak symmetry breaking (EWSB) gives mass to the  $W$  and  $Z$  gauge bosons. The fermions also acquire their mass through Yukawa interactions between the Higgs and fermion fields.

Although the Brout-Englert-Higgs mechanism ensure that the SM theory will remain viable as a perturbative physical theory up to the Planck scale, current experimental evidence suggests that the SM is not a complete theory of nature. SM leaves several important fundamental questions unanswered. These include but is not limited to the nature of Dark Matter (DM), the apparent matter/anti-matter asymmetry in the universe, why does SM particles have the mass spectrum that they do, the potential unification of EW and strong interactions at high energy scales, the nature of neutrino mass and the hierarchy problem regarding the naturalness of the Higgs mass. The answers to these open questions are the major physics goals of many different physics experiments across disciplines including the energy frontier, intensity frontier and experiments in astrophysics.

One proposed solution to many of these questions is the introduction of a new spacetime symmetry called supersymmetry. Supersymmetry imposes a new symmetry between fermions and bosons allowing one to transform into the other and a supersymmetric Lagrangian is invariant under such transformations. In this way, the supersymmetric extension to the SM (SUSY) predicts the existence of complete set of new particles composed of a yet undiscovered superpartner to every known SM particle. SUSY is one possible solution to the hierarchy problem of the Higgs as large contributions to the Higgs potential are canceled between particles and their superpartners at high mass scales. Some supersymmetric models also unify the strong and electroweak force at high energies, generates

more cp violation necessary to generate the matter/antimatter asymmetry and produces plausible dark matter candidates. Plus when SUSY is imposed as a local symmetry, general relativity (GR) is automatically included. The resulting theories are referred to as supergravity and offers a potential to uniting GR with quantum mechanics.

SUSY is expected to be a spontaneously broken symmetry. Many different SUSY symmetry breaking mechanism have been proposed but they all make the superpartners much more massive than their SM counterparts and explains why we have yet to see any superpartners in previous high energy experiments including the Tevatron and LEP.

A major goal of the Large Hadron Collider (LHC) experiment is to search for the predicted superpartners at an unprecedeted energy scheme. If SUSY is the solution to the hierarchy problem and restores naturalness to the Higgs mass calculation then the superpartner to the top quark (stop) is expected to be no heavier than a few TeV. The stop's mass is strongly constrained due to the large coupling between the SM top quark and the Higgs ( $\lambda_t \sim 0.94$ ). As such, searches for the stop at the LHC is especially interesting because the stop's mass may be low enough to be accessible at the energy scale of the LHC.

This thesis concerns the search for stops in an traditionally experimentally difficult region. One of the decay mode of the stop is to decay into its partner, the top quark, and the superpartner to the neutral electroweak boson, the neutralino. Traditional searches often targets events with large missing transverse energy ( $E_T^{\text{miss}}$ ), the experimental signatures of neutralinos because such large amounts of  $E_T^{\text{miss}}$  is difficult to produce with SM processes alone. However, when the stop mass is close to that of the top mass plus the neutralino mass, both the top and neutralino gain very little momenta

from the decay. The invisible neutralinos in turn generate very little  $E_T^{\text{miss}}$ . This leaves only the visible tops which are mimicked by standard model ttbar. The fact that SM ttbar can have a production cross-section anywhere from 50 to 300 times that of the stop even if the stop mass is low, around 250 to 400 GeV, means that searches for stops in this diagonal region have been hampered due to the difficulty of distinguishing between stop signal and ttbar background in this region of phase space.

This thesis demonstrates a new method of searching for stops in the compressed region by isolating events with strong initial state radiation (ISR). The stop decay products can gain additional momenta if the entire stop system is boosted by ISR. The correlation between ISR  $p_T$  and stop decay product  $p_T$  tend to be extremely strong in this region precisely because the stop decay products gain little momenta from the stop decays in compress region. we turn a critical weakness inherent to this region of phase space into a strength.

Specifically there exists a strong correlation in both direction and magnitude between ISR  $p_T$  and  $E_T^{\text{miss}}$  in signal. The neutralinos should inherit exactly  $m_{\tilde{t}}/m_t$  fraction of the original ISR  $p_T$  if the stop has exactly enough mass to create a top and neutralino at rest and the  $E_T^{\text{miss}}$  and ISR systems should be exactly back to back. This two-dimensional correlation allows us to separate signal from ttbar background and overcome the difference in production cross-section.

As part of this analysis we developed an accurate ISR identification system that is able to identify whole ISR systems composed of multiple jets. The algorithm works by first finding the axis of maximum back to back  $p_T$  call the thrust axis. The ISR and sparticle boost represents the single largest back to back kick in events with strong ISR. Therefore, the thrust axis should mimic the axis of back to back boost between the ISR and sparticle systems in events with strong ISR. Once we find the

thrust axis, we divide the event into an ISR hemisphere and an stop hemisphere according to the thrust axis. All objects in the hemisphere contains the  $E_T^{\text{miss}}$  is considered to have originated from a stop decay as the neutralinos must travel in the same direction as the original stops and all objects in the hemisphere opposite the  $E_T^{\text{miss}}$  is considered to have originated from ISR.

The ISR identification algorithm is completely general and can be used to identify ISR for SM processes as well as other searches. The performance of this ISR identification algorithm is covered in detail in chapter 8. In summary, we see that we can achieve a 9 percent uncertainty on the reconstructed ISR pt for both stop and ttbar events with at least 400 GeV of true ISR  $p_T$ . This uncertainty includes any detector uncertainty due to the reconstruction of jets,  $E_T^{\text{miss}}$  and other physics objects.

Using the 2015 and 2016  $\sqrt{s} = 13$  TeV dataset, we were able to exclude stops with masses between 225 and 600 GeV. In between 250 and 400, we are able to achieve expected exclusion p-values less than  $5 \times 10^{-4}$  in a region with no previous sensitivity.

Its important to note that the same problem of low  $p_T$  decay products and low  $E_T^{\text{miss}}$  arises in many other searches if the mass splittings are small or at a particular value where the decay products gains very little momenta. Such regions of phase space are referred to in general as "compressed regions" and occurs in many different searches for SUSY and other exotic particles. The same problem and solution demonstrated in this thesis can be applied to searches to Higgsinos, Charginos, and even dark matter particles unrelated to SUSY. Plus the accurate ISR identification algorithm can be used not only in searches for new physics but offers a new method for directly measuring the amount of ISR produced in conjunction with SM particles. Potential applications includes measur-

ing SM ttbar's  $t\bar{t} p_T$  without the need for reconstructing individual tops.

The thesis is organized as follows. Chapter 1 presents an overview of the standard model and theoretical motivations for supersymmetry. Chapter 2 describes the experimental setup of the LHC accelerator and ATLAS detector. Chapter ?? and chapter 4 details the reconstruction and calibration of physics objects from detector signature and the ATLAS trigger system. Physics objects used in the analysis is defined in chapter ???. Chapter ?? describes the process used in generating the Monte Carlo simulations of stop signal and SM background processes.

Chapter ?? concerns general strategy used in traditional SUSY searches and the general strategy of using strong initial state radiation (ISR) to separate signal from background in compressed region analyses. We present a new algorithms that uses the axis of maximum back to back  $p_T$  to identify ISR in chapter ???. The algorithm is based on a more general set of algorithms called recursive jigsaw reconstruction that uses exterminations to classify objects in events with missing information such as in the case of  $E_T^{\text{miss}}$  and large multiplicity of objects. The precision of the ISR identification algorithm is also demonstrated on both signal and background.

Chapter 9 - 11 describes the 2015 and 2016 LHC dataset that is used for this analysis and the kinematic selections used to define the signal region. The chapters also develop physical intuition on each signal region selection and how they reject background.

The different SM backgrounds that remain in the signal region are described in detail in chapter 12. This chapter also cover the different methods used to estimate each background, goes especially into detail on the dominate background SM ttbar. A large portion is devoted to building intuition on the unique kinematic properties of the backgrounds in the signal region. This physical intuition

is used to explain how the control regions are designed in order accurately estimate the backgrounds and minimize systematic uncertainties.

Chapter ?? describe each of the experimental and theoretical systematics associated with signal and background. Systematic uncertainty is divided into two categories, experimental uncertainties due to limitations of detector resolution and object reconstruction algorithms and theoretical uncertainties on the calculation of Monte Carlo simulations.

Chapter 14 summarizes the statistical methods used to extract the signal strength. Finally chapter ?? and ?? shows the result of the search and give the exclusion limits on stop parameter space.

# 1

## Theoretical Motivation

### 1.1 THE STANDARD MODEL

The standard model (SM) describes our current understanding of the interactions of all known elementary particles. SM is composed of 3 parts; fermions with spin 1/2 that make up the visible matter in our universe; vector bosons with spin 1 that mediates the interactions between fermions; and the scalar spin 0 Higgs boson that gives mass to the massive fermions and some vector bosons.

The fermions are organized in two groups, the quarks and leptons, with three families of increasing mass. The force mediators, the photon,  $W/Z$  boson, and gluon are respectively responsible for the electromagnetic, weak, and strong interactions. A diagram listing all known particles is shown in figure 1.1.

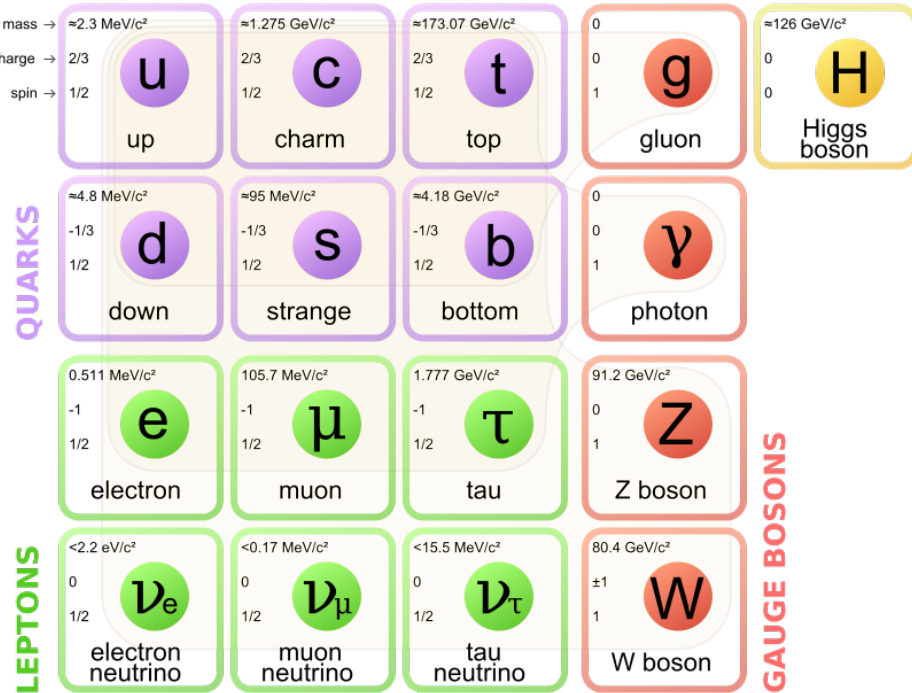


Figure 1.1: List of standard model elementary particles

Interactions in the SM are described by non-abelian Yang-Mills gauge theory with the gauge group  $SU(3)_C \times SU(2)_L \times U(1)_Y$  where  $SU(3)_C$  corresponds to the strong interaction and  $SU(2)_L \times U(1)_Y$  corresponds to the electroweak interactions. SM particles can be organized by the representations of the gauge groups. The left handed component of the fermions form an  $SU(2)_L$  doublet while the right handed components form an  $SU(2)_L$  singlet. Effectively this means only the

left handed component of SM fermions interacts via the weak interaction.

In addition to EW interactions, the quarks also interact via the strong interaction described by the  $SU(3)_C$  symmetry. These quarks carry color charge in addition to their electromagnetic charges. The gluons which mediate the strong interactions also carry color charge. The self interaction of the gluon causes the coupling strength of the strong coupling constant  $\alpha_s$  to diverge at low energies. This phenomena called confinement ensures that no free quarks are confined to be within composite color singlet states in the form of hadrons. At the same time, the running of  $\alpha_s$  approaches zero at high energy forming a phenomenon known as asymptotic freedom.

For energetic particles like those produced in proton-proton collisions at the LHC, colored partons will radiate additional collinear gluons and quark/anti-quark pairs in a parton shower. These partons will in-turn form color-singlet hadrons once the energy scale is lower then IR-cutoff scale due to confinement. The result is a jet of color-neutral baryons and mesons localized in a narrow cone in the direction of the initial colored parton.

The generators of the gauge groups correspond to the massless spin 1 vector bosons. However, the  $W^\pm$  and  $Z$  bosons acquire mass through spontaneous electroweak symmetry breaking using the Higgs mechanism. This is accomplished using an additional complex  $SU(2)_L$  doublet of spin zero field, the Higgs field. The Higgs has a nonzero vacuum expectation value (VEV) at the minimum of its quadratic potential shown in equation 1.1. When  $\lambda > 0$  and  $m_H^2 < 0$ ,  $\langle H \rangle = \sqrt{-m_H^2/2\lambda}$ .

$$V(H) = m_H^2 |H|^2 + \lambda |H|^4 \quad (1.1)$$

This breaks the  $SU(2)_L \times U(1)_Y$  electroweak symmetry and leaves only the  $U(1)_{em}$  electromagnetism invariant. Meanwhile, the other gauge bosons from  $SU(2)_L \times U(1)_Y$  gains a longitudinal degree of freedom from degrees of freedom associated with the Higgs doublet and thereby gaining mass. The photon,  $W^\pm$  and  $Z$  bosons are therefore linear combinations of the original  $SU(2)_L$  and  $U(1)_Y$  generators. The Higgs boson also gives fermions their mass through Yukawa couplings.

After symmetry breaking, only one neutral scalar component of the Higgs doublet is left. This is the massive Higgs boson observed in July 2012 at the LHC.

## 1.2 INTRODUCTION TO SUPER-SYMMETRY

Current combined measurement of the Higgs boson at ATLAS and CMS gives an observed Higgs mass of  $125.09 \pm 0.21(\text{stat}) \pm 0.11(\text{syst})$  GeV.<sup>29</sup> Plus  $\langle H \rangle \sim 174$  GeV due to experimental measurements of the properties of the weak interactions. This implies that the parameters  $\lambda$  and  $m_H^2$  in the Higgs potential in equation 1.1 have the values of 0.126 and  $-(92.9 \text{ GeV})^2$  assuming SM is the correct effective field theory.

However theoretical calculations gives enormous quantum corrections to  $m_H^2$ .<sup>43</sup> For example, the correction to  $m_H^2$  from a loop containing a Dirac fermion  $f$  with mass  $m_f$  is given in equation 1.3. The Feynman diagram associated with the fermion loop is shown in figure ??

$$\Delta m_H^2 = -\frac{|\lambda_f|^2}{8\pi^2} \Lambda_{UV}^2 + \dots \quad (1.2)$$



**Figure 1.2:** One-Loop corrections due to a Dirac fermion  $f$  and a scalar  $\tilde{f}$  to the Higgs mass parameter  $m_H^2$

$\lambda_f$  is the Yukawa coupling between the fermion and the Higgs and  $\Lambda_{UV}$  is the ultraviolet cutoff used to regulate the loop integral.  $\Lambda_{UV}$  can be interpreted as around the energy scale of new physics. Since the scale of new physics maybe orders of magnitudes larger then the electroweak scale, the quadratic dependence of  $m_H^2$  on  $\Lambda_{UV}$  makes the Higgs potential extremely sensitive to new physics and fine tuning between the Higgs bare-mass and the corrections is needed to keep the observed  $m_H^2 = -(92.9 \text{ GeV})^2$ . This sensitivity to high mass scales for the Higgs potential is referred to as the hierarchy problem. Additional terms also exists in the correction but they grow at most logarithmically in  $\Lambda_{UV}$ .

Supersymmetry (SUSY) solves this problem by proposing that there exist a new space-time symmetry with respect to the transformation  $\mathcal{Q}$  that turns fermions into bosons and bosons into fermions.

$$\mathcal{Q} |Boson\rangle = |Fermion\rangle \quad \mathcal{Q} |Fermion\rangle = |Boson\rangle \quad (1.3)$$

The supersymmetric Lagrangian is invariant under transformations of  $\mathcal{Q}$  and  $\mathcal{Q}^\dagger$ . In order for this to be satisfied, SUSY proposes the existence of a supersymmetric partner (superpartner) to every known SM particle which is related to each other by the  $\mathcal{Q}$  transformation and differ from each other by spin  $1/2$ . If SUSY was an exact symmetry then, the SM particle and its superpartner must have the same mass as  $\mathcal{Q}$  does not change mass. However, we have yet to discover even a single superpartner to the SM. Therefore, SUSY must be broken at low energy scales and the superpartners have significantly more mass than their SM counter parts.

Supersymmetry symmetry breaking can occur in many ways that are beyond the scope of this document. For example in Gauge-mediated supersymmetry breaking, some scalar fields in the SUSY Lagrangian gains a vacuum expectation value due to their potential energy shape. This symmetry breaking gives mass to some fermions and their super-partners called messengers. The messengers are too heavy to be directly detectable, but they give mass to the superpartners of the SM via loop interactions. SM gauge symmetry ensures that the loop correction to the SM gauge bosons are zero to all orders of magnitudes, but the same protection is not afforded to their superpartners, the gauginos, which gains mass through one-loop diagrams involving virtual messenger particles. Likewise, the scalar partners to SM fermions gain mass through two-loop diagrams involving virtual messengers and SM gauge bosons. These loop contributions leads to heavier superpartners relative to their SM counter parts. More details on SUSY symmetry breaking can be found in <sup>43</sup>.

For now we will look at some phenomenological consequences of the existence of heavy superpartners. For example, if a complex scalar particle  $\tilde{f}$  with mass  $m_{\tilde{f}}$  exists and couples to the Higgs with the term  $-\lambda_S |H|^2 |\tilde{f}|^2$  then correction due to the loop diagram in figure 1.2 is given in equation

I.5.

$$\Delta m_H^2 = \frac{\lambda_s}{16\pi^2} [\Lambda_{UV}^2 - 2m_f^2 \ln \Lambda_{UV}/m_f + \dots] \quad (I.4)$$

This correction also contains a quadratically divergent term that has an opposite sign to equation I.3. The two quadratic contributions to  $m_H^2$  will cancel if  $|\lambda_f|^2 = \lambda_s$  and we are left with only a term that is proportional to  $\ln \Lambda_{UV}/m_f$ . In fact, this cancellation of quadratically divergent term will occur not only for the 1 loop case, but for all orders of magnitude in perturbation theory if supersymmetry exists.

The term that remains after cancellation is proportional to equation ??.

$$\Delta m_H^2 \sim m_f^2 \left[ \frac{\lambda_s}{16\pi^2} \ln \Lambda_{UV}/m_f \right] \quad (I.5)$$

It's important to note that while the correction is now not so strongly dependent on  $\Lambda_{UV}$  because of the natural log, the correction term is also directly proportional to  $m_f^2$ . This implies that the superpartners masses cannot be too large, otherwise the correction to  $m_H^2$  is again too large. Setting  $\Lambda_{UV}$  to approximately at the Planck scale  $M_P$  and  $\lambda_s \sim 1$ , we find that  $m_f$  for the lightest supersymmetric particle should not be heavier than the TeV scale<sup>43</sup> if SUSY is the solution to the hierarchy problem. In particular, we know that the superpartner to the top quark has a coupling to the Higgs of order 1 due to  $\lambda_s = |\lambda_f|^2 \sim 0.94^2$ . This makes the stop potentially within reach of the energy of the LHC.

Supersymmetry also introduces many new interactions not found in the SM. Some of these inter-

actions directly violate total lepton and baryon numbers. If such interactions existed then the half life of a proton may be a tiny fraction of a second. However, proton decay experiments have shown that the proton half-life exceeds  $10^{32}$  years. A new discrete symmetry called *R-parity* is introduced to remove these B and L violating terms from the supersymmetric Lagrangian.

The quantity  $P_R$  defined in equation 1.6 and must multiply to 1 for all interaction vertexes for R-parity to be conserved.  $P_R$  equals 1 for all SM particles and equals  $-1$  for all superpartners.

$$P_R = (-1)^{3(B-L)+2s} \quad (1.6)$$

R-parity conservation has several important phenomenological consequences. In R-parity respecting SUSY, superpartners are always produced in pairs. Superpartners must always decay into other superpartners forming a long decay chain of SUSY particle to SUSY particle that ultimately end in the lightest supersymmetric particle (LSP) which is absolutely stable. If the LSP is electrically and color neutral, then it is an attractive dark matter candidate as a weakly interacting, stable particle. We assume R-parity is conserved and the LSP is a neutralino for this analysis.

# 2

## Experimental Apparatus

The study of standard model (SM) physics at the TeV scale and search for potentially new physics beyond the standard model (BSM) is the highlight of current physics programs at the Large Hadron Collider (LHC). The LHC is a circular superconductor hadron-hadron accelerator capable of accelerating and colliding both protons and lead ions. The LHC is built in the previous LEP tunnels between 45 to 170m underground near the city of Geneva at the Organization for European Nuclear

Research or CERN.

During 2015 to 2016, the LHC collided protons with a center of mass energy of  $\sqrt{13}$  TeV. The LHC has already surpassed its design peak instantaneous luminosity by reaching peak instantaneous luminosities of  $1.34 \times 10^{34} \text{ cm}^{-2} \text{ sec}^{-1}$ .

The LHC uses 4 major particle detectors located at its 4 interaction points to study the result of these collisions. Two of these, ATLAS and CMS are hermetic  $4\pi$  general purpose detectors that study a wide variety of SM and BSM physics including SUSY. ATLAS and CMS are located at the opposite end of the ring to ensure equal luminosity and serve as validations to one another. The ALICE detector specializes in collisions of heavy ions. LHCb specializes in physics involving the bottom quark.

In addition to the 4 major particle detectors, three smaller experiments, TOTEM, MoEDAL and LHCf, study proton-proton scattering cross sections, diffractive processes, and cosmic ray physics.

This analysis uses data collected by the ATLAS detector in 2015 and 2016. A summary of the LHC accelerator complex and the ATLAS detector will be given in this chapter.

## 2.1 THE CERN ACCELERATOR COMPLEX AND THE LARGE HADRON COLLIDER

Before collision in one of the LHC experiments, protons are first accelerated through a series of accelerators that form the CERN accelerator complex shown in figure 2.1. Hydrogen atoms are ionized and the resulting protons are first accelerated to 50 MeV by the Linear Accelerator 2 (LINAC<sub>2</sub>). Then the protons are injected into a series of circular accelerators, the Proton Synchrotron Booster

(PSB), the Proton Synchrotron (PS) and Super Proton Synchrotron (SPS) which further increases the proton energy to 1.4, 25 and 450 GeV respectively. The protons are arranged into bunches composed of approximately  $1.1 \times 10^{11}$  protons each and injected into the LHC. During 2015 and 2016, the LHC operated with both 50 ns and 25 bunch spacings and can nominally accommodate up to 2808 bunches in a single run.

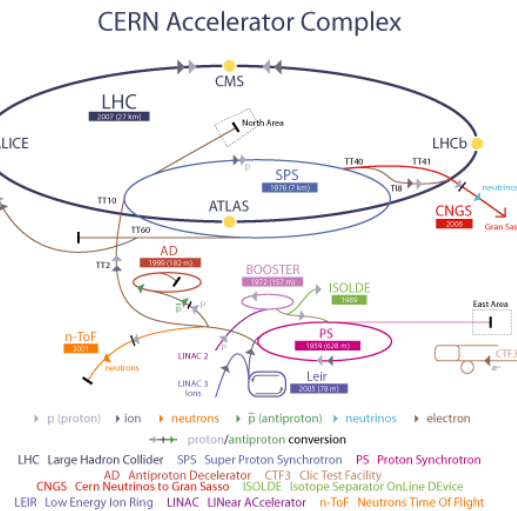


Figure 2.1: The Large Hadron Collider complex. (Taken from <sup>35</sup>)

The LHC shares the same geometry as LEP with eight arc and eight straight sections. The main

LHC body consist of 1232 dipole Niobium Titanium superconducting magnets that are used to generate the 8.33 Tesla magnetic field necessary to bend the 7 TeV proton beams. The LHC uses a two-in-one magnet design shown in figure 2.2 both as a cost saving measure and because of the limited space in the tunnels. The two-in-one magnet design uses a single cryogenic system and vacuum vessel for both proton beams.

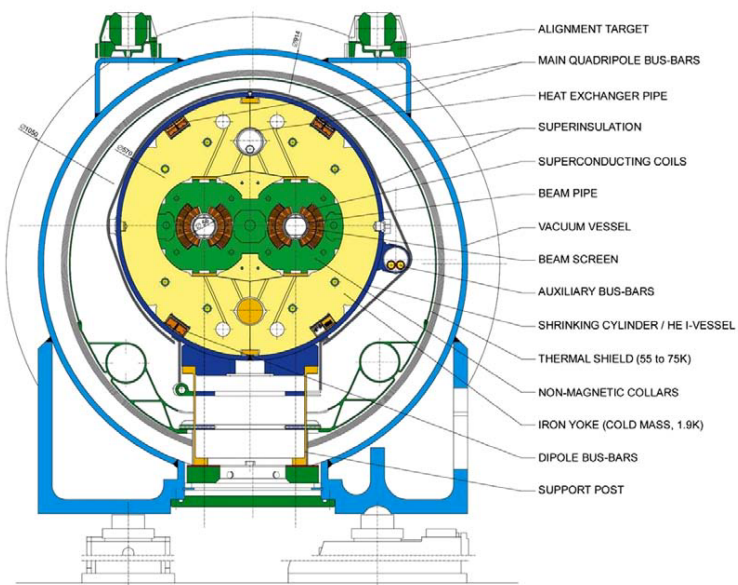


Figure 2.2: Cross-Sectional View of a Large Hadron Collider Dipole Magnet. Figure taken from <sup>35</sup>

392 quadrupole magnets are placed after approximately every three dipole sections to stabilize and focus the beam using the principle of strong focusing. Higher order sextupoles and octupoles magnets provide further corrections.

The beams are accelerated using a 400 MHz superconducting radio frequency (RF) cavity system. Two independent RF systems are used for the two beams heading in opposite directions. Each RF

system consist of eight cavities. The total accelerating field inside the cavity is 5 MV/m and each cavity delivers 2 MV of accelerating voltage. The beams are bent back to repeatedly receive acceleration via the same cavity.

Further upgrades planed in the Phase 1 shutdown between 2019 and 2021 are projected to further double the instantaneous luminosity and allow the LHC to reach its designed center of mass collision energy of  $\sqrt{14}$  TeV.<sup>3</sup>

## 2.2 THE ATLAS DETECTOR

The ATLAS Detector shown in figure 2.3 is a general purpose detector that is designed to both search for new physics at the TeV scale and precision measurement of SM parameters.<sup>32</sup> The ATLAS detector is composed of several subdetector arranged layer by layer in concentric cylinders surrounding the interaction point. The hermitic detector cover nearly the entire  $4\pi$  solid angle around the interaction point.

Each subdetector system specialize in the detection of a specific subset of particles that are expected to result from collisions provided by the LHC. Starting from the interaction point and moving out, the detector can be divided into the inner tracker, the electromagnetic calorimeter, the hadronic calorimeter and the muon spectrometer. The detector signatures left by different particles can be seen in figure 2.4.

Details on the reconstruction of physics objects can be found in chapter ???. A brief description of detector signatures will be given here in order to motivate the purpose of each subdetector system.

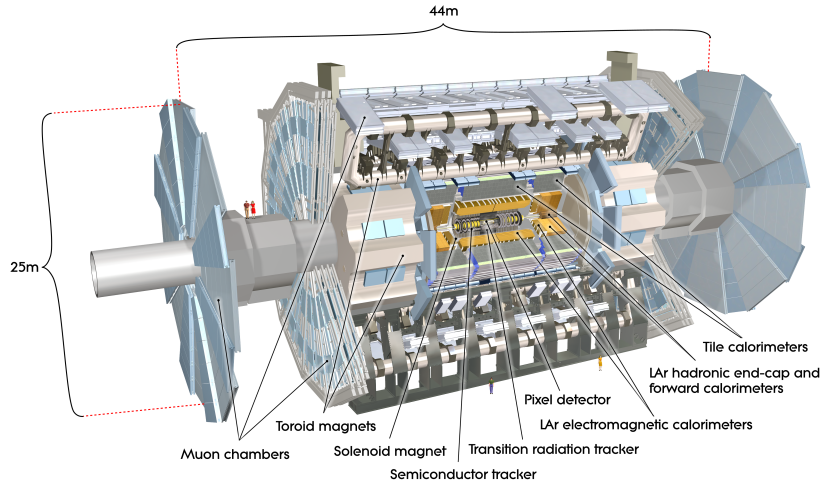


**Figure 2.3:** Cutaway view of the ATLAS detector with different sub-detector systems labeled. Figure taken from <sup>32</sup>

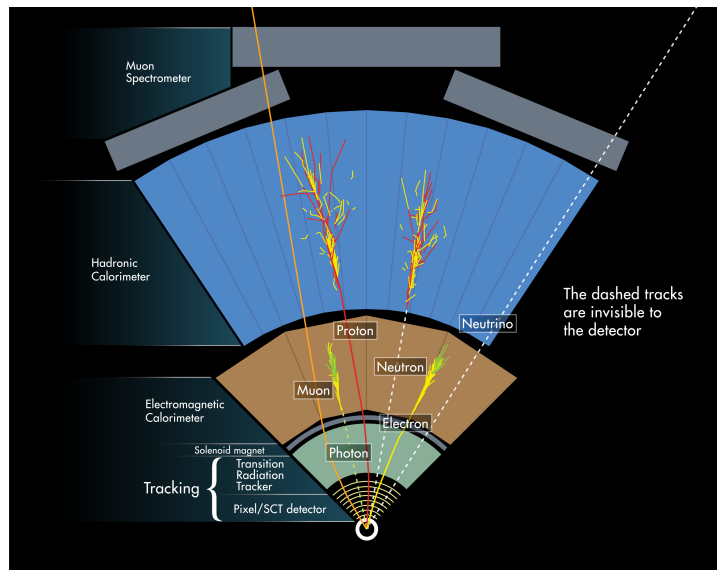


**Figure 2.4:** Artistic representation of different detector signatures left by particles in ATLAS. Figure taken from <sup>45</sup>

The inner tracker measure the position of charged particles as they fly through the detector.

These positions measurements are then connected to form a track that follows the flight path of the charged particle. A 2 Tesla axial magnetic field bath the inner detector volume and is provide by

the central solenoid superconducting magnet. The magnetic field bends any charged particle in the inner tracker. The momenta of the charged particle can be identified by the amount of bend in the track relative to the particle charge and mass.

The calorimeters measure the energy of all charged and neutral particles that interact via the electromagnetic and strong force. The particle interact with the dense absorbing material via a number of interactions. The dominant interaction for electromagnetically charged particles such as the electron is photon emission through bremsstrahlung and ionization. Neutral high energy photons interact primarily by pair producing electrons. Any emitted photon and electron will pair produce electrons emit photon until the resulting particles no longer have enough energy to continue the process. This cascade of particles is called a particle shower. Hadronic particles that interact via the strong force will also form analogous hadronic showers.

The shower particles deposit energy in the layers of the calorimeter with an *active* material. The number of shower particles are then measured by the active material resulting in a signal. The ATLAS calorimeter alternates between absorber and active material layers. Thereby measuring the longitudinal and lateral shower shape and shower depth by combining information from the different layers. Showers from electromagnetic objects such as photons and electrons form denser narrow profiles while showers from strongly interacting particles form board showers that penetrate deep into the hadronic calorimeter.

Muons are the only charged SM particle that are expected to be able to fully penetrate the calorimeter in-tact. They in turn leave a track in the muon spectrometer. This track can be matched to the inner detector track forming a combined muon track that traverses the entire detector. A set of barrel

and endcap toroid magnets provide the magnetic field to the muon spectrometer and adding to the momenta measurement of muons. Fields vary depending on location but on average an integrated field of  $2.5\text{ Tm}$  and  $4\text{ Tm}$  are expected for muons traversing through the barrel and endcap.

The combination of these different detector signatures is combined to identify and reconstruct the many different particles produced in a particle collision. Electrons leave an electromagnetic shower in the calorimeter with an associated track. Unconverted photons leave an electromagnetic shower without an associated track. Hadrons fragment into jets and leave a hadronic shower in both the inner detector and hadronic calorimeter with perhaps a number of associated ID tracks. Muons are reconstructed from a combined ID and MS track with limited energy deposited in the calorimeter. Taus either decay leptonically or semileptonically to an electron or muon or decays hadronically to pions and leave a narrow hadronic shower in the calorimeter with one or three associated tracks. Particles that interact via only the weak force i.e. neutrinos do not interact with the ATLAS detector. They escape the detector completely and their presence are inferred through the conservation of transverse momenta.

The following subsections are dedicated to covering each subdetector in further detail.

### 2.2.1 INNER DETECTOR

The inner detector consists of three independent sub-detectors. Two silicon semiconductor detectors; the Pixel detector and the Semiconductor Tracker (SCT) form the inner part of the tracking volume and the Transition Radiation Tracker (TRT) covers the outer part. The three sub-detectors operate independently of one another and offers a precise and robust pattern recognition system

used to reconstruct the tracks of charged particles. In addition to reconstructing tracks, the ID also provides the information precise impact parameter measurements and primary and secondary vertex reconstruction. The whole inner detector is immersed in a 2 T axial magnetic field produced by a solenoidal superconducting magnet.

The layout of the inner detector can be seen in figure 2.5. A summary of the geometry and coverage of each ID subdetector is given in table ??.

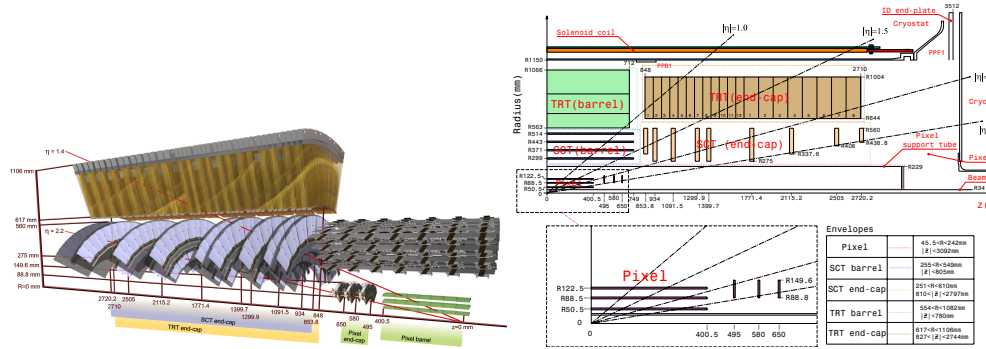


**Figure 2.5:** (a) Cutaway view of the ATLAS inner detector. (b) Radial View of the ATLAS inner detector (Figure Taken from <sup>32</sup>)

More detail on each sub-detector technology is given below.

## PIXEL DETECTOR AND THE INSERTABLE B-LAYER

The Pixel detector consists of three layers of high resolution pixel sensors in the cylindrical barrel and three wheels of pixel sensors in the endcap. Another inner most layer of pixel sensors called the Insertable B-Layer (IBL) was added directly on top of the new beryllium beam pipe in the first long shutdown between 2012 and 2015. The new beam pipe decreases the amount of multiple scattering before the inner tracker.

The original 3 layer Pixel detector contain of 80.4 million readout channels spread over 1744 Pixel modules. Each module house a sensor tile with an area of  $63.4 \times 25.4 \text{ mm}^2$ . The sensors are composed of  $250 \mu\text{m}$  thick n-type silicon wafer pixels with a size of  $50 \times 400 \mu\text{m}^2$ . The modules are read out by 16 front-end electronic chips with 2880 read out channel each.

The pixels have an intrinsic accuracy of  $10 \mu\text{m}$  in the bending  $\phi$  direction and  $115 \mu\text{m}$  accuracy in the non-bending  $z$  direction in the barrel and  $\phi$  direction in the endcap.

Installed in 2014, the Insertable B-Layer (IBL) contributes another 12 million channels to the Pixel system in Run 2.<sup>IBL,27</sup> Located directly on top of the beam pipe at 3.3 cm from the beam axis, the IBL is the new most inner layer of the Pixel detector (the previous innermost B-Layer was at 5 cm). The IBL is composed of 14 staves tilted at  $14^\circ$  in  $\phi$ . A schematic representation of IBL stave relative to the beam pipe can be seen in figure 2.6. Each stave is equipped with 32 FE-I4 front-end chip bonded to silicon sensors. Each FE-I4 chip contain 26880 pixel cells with  $50 \times 240 \mu\text{m}$  pitch.

The improvement in both the tracking lever arm and spacial resolution represent approximately a factor of 2 impact parameter resolution and a factor of 4 gain in b-tagging light jet rejection power.

## SEMICONDUCTOR TRACKER

The SCT is composed of 4 coaxial layers of concentric cylinders in the barrel and 9 disks in each endcap and contributes at least an additional 4 layers of high precision position measurements to tracks originating from the IP in the intermediate radial range. The entire SCT consists of approximately 6.3 million readout channels on over 4088 modules. A barrel module is equiped with a sensor with a size of  $64.0 \times 63.6 \text{ mm}^2$  in the transverse plane. The barrel sensor are made of  $285 \mu\text{m}$  thick silicon

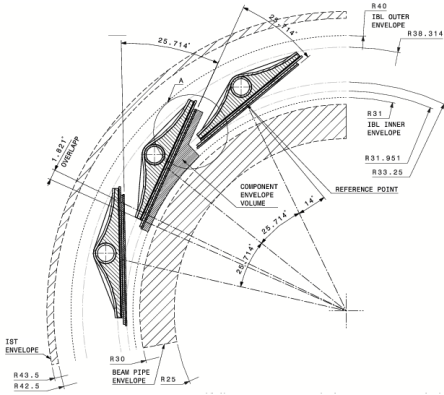


Figure 2.6: Schematic of the ATLAS Insertable B-Layer (IBL) (Figure Taken from <sup>IBL</sup>)

wafer and contain 768 strips, achieving a barrel strip-pitch of 80  $\mu\text{m}$ . The endcap module contain sensors that are trapezoidal in shape with strip pitch that vary from 54  $\mu\text{m}$  to 90  $\mu\text{m}$ .

The sensors are mounted on a back to back fashion at angle of 40 mrad relative to one another. This allows the measurement of non-bending direction along with improved spacial resolution in the bending  $\phi$  direction.

The intrinsic accuracy per SCT module, dictated by the strip pitch, is 17  $\mu\text{m}$  in the bending  $\phi$  direction and 580  $\mu\text{m}$  in the non-bending z direction in the barrel and R direction in the endcap.

## TRANSITION RADIATION TRACKER

The TRT is the outermost component of the ID and contribute approximately 351000 readout channels. Each channel correspond to a 4 mm diameter polyimide straw drift tube with a 31 $\mu\text{m}$  gold plated tungsten anode wire, providing an intrinsic accuracy of 130  $\mu\text{m}$ . The number of channels is low compared to the silicon detectors but the TRT is able to compensate for this by providing a

long lever arm to the track measurement and high hit multiplicity.

In the barrel region, the straws are 144 cm long and arranged parallel to the beam axis in 73 layers

. In the end-cap region, straws are 37 cm long and arranged in 160 radial layers in wheels. A typical track will traverse 36 straws in the barrel, because the tubes are arranged a matrix with each layer offset from one another.

The dielectric material used to interleave the straws induces transition radiation in traversing charged particles. The low energy transition radiation photons are absorbed by the Xenon-based gas mixture in the straws, thereby providing much larger signal amplitudes than minimum-ionizing charged particles. This can be used to distinguish electrons from pions based on the energy deposition.

In 2015 and 2016 operations, approximately 1/3 to 2/3 of the TRT barrel and 1/7 of the TRT end-cap is filled with an Argon gas mixture instead of Xenon due to leaks. This adversely affects electron identification efficiency by a few percent and is taken into account by a scale factor electron identification in simulation.

### 2.2.2 THE CALORIMETER

The ATLAS calorimeter provide near full solid angle coverage of the interaction point up to an  $\eta$  of 4.9. The calorimeter system is composed of two parts the electromagnetic calorimeter (ECAL) and hadronic calorimeter (HCAL). These two detector technology use scintillating tiles and liquid argon (LAr) as active materials. The design resolution for electromagnetic objects is  $\sigma_E/E = 10\%/\sqrt{E} \oplus 0.2\%$ . Measurements from pions give a hadronic energy resolution of  $\sigma_E/E = (56.4 \pm 0.4)/\sqrt{E} \oplus$

$(5.4 \pm 0.1)$  in the barrel region to  $\sigma_E/E = (94.2 \pm 1.6)/\sqrt{E} \oplus (7.5 \pm 0.4)$  in the forward regions.

The cutaway view of the ATLAS calorimeter can be seen in figure 2.7 and a summary of the calorimeter geometry is given in table ??

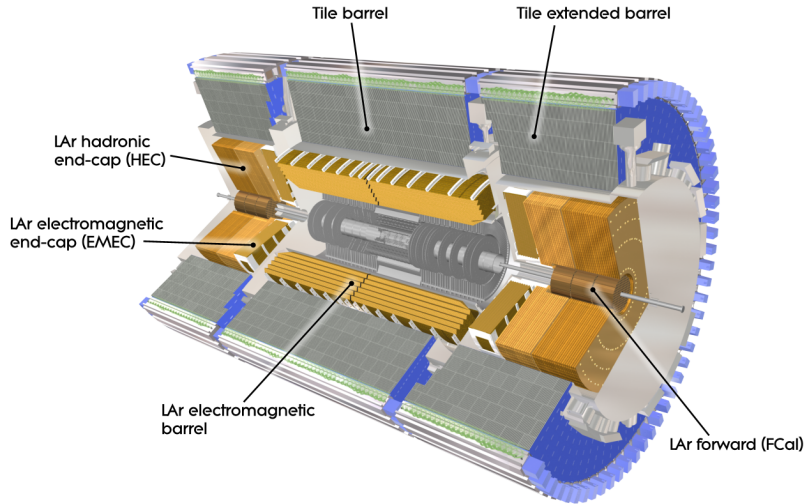


Figure 2.7: Layout of the ATLAS calorimeter. (Figure taken from <sup>32</sup>)

## ELECTROMAGNETIC CALORIMETER

The ATLAS ECAL is sampling calorimeter with lead absorber plates and liquid argon (LAr) active material arranged in an accordion geometry covering up to an  $\eta$  of 3.2. The accordion design provides full crack-less coverage in  $\varphi$  and integrates more charge along the longitudinal direction of the shower.

The ECAL is split into a barrel and two endcap components with a transition region of  $1.37 < |\eta| < 1.52$  in between. The barrel component is divided into two 3.2 m long half-barrel sections with an inner and outer radius of 2.8 m and 4 m respectively. The endcap is divided into two coaxial

wheels each 63 cm thick with an outer wheel covering  $1.375 < |\eta| < 2.5$ , and an inner wheel covering the region  $2.5 < |b| < 3.2$ .

The barrel ECAL is also segmented longitudinally into 3 layers with an additional presampler layer in front in certain regions. The presampler is from a thin liquid-argon layer 11mm in depth and is designed to determine the energy loss from material upstream of the calorimeter. The first layer after the presampler has a depth of  $4.3 X_0$  and a fine granularity of  $\Delta\eta \times \Delta\phi = 0.003 \times 0.1$ . The high granularity allows for precision measurement of EM showers and can distinguish between the shower shape of electron/photons from those of  $\pi^0 \rightarrow \gamma\gamma$  decays. The middle layer absorbs most of the energy of the EM shower and are made up of cells with  $\Delta\eta \times \Delta\phi = 0.025 \times 0.025$  with a depth of  $16 X_0$ . The back layer has cell sizes of  $\Delta\eta \times \Delta\phi = 0.05 \times 0.025$  a depth of  $2 X_0$ . The back layer is designed to only collect the tails of the EM showers and used to distinguish between EM and hadronic showers.

The endcap ECAL is also divided into three longitudinal layers similar to the barrel. The front layer has a depth of  $4.4 X_0$  and varies in cell size from  $\Delta\eta \times \Delta\phi = 0.003 \times 0.1$  to  $\Delta\eta \times \Delta\phi = 0.006 \times 0.1$ . The middle layer has cells with the same size as the barrel with  $\Delta\eta \times \Delta\phi = 0.025 \times 0.025$  and a similar depth. The back layer has a twice coarser granularity in  $\eta$  with  $\Delta\eta \times \Delta\phi = 0.05 \times 0.25$ . A presampler also exists for the endcap with each presampler module consisting of two 2mm thick LAr layers.

The segmentation of the ATLAS ECAL can be seen in figure 2.8.

The total thickness of the ECAL is at least  $22 X_0$  in the barrel and  $24 X_0$  in the endcap for electrons and photons and approximately 1.5 nuclear interaction length for hadronic objects.

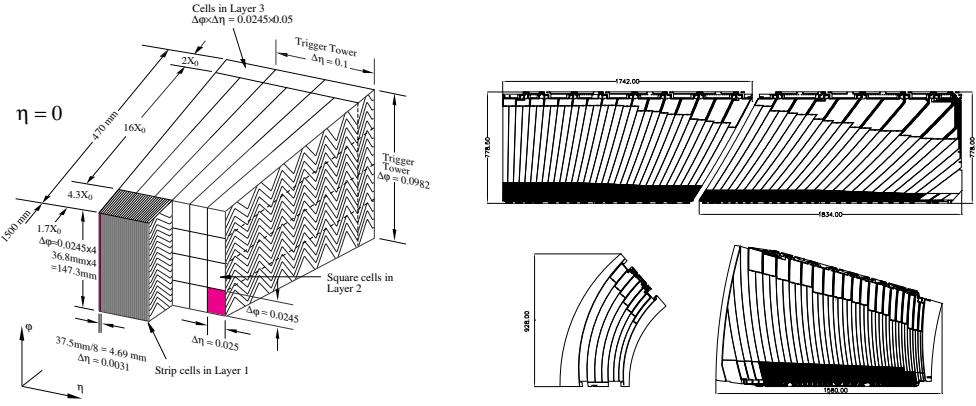


**Figure 2.8:** (a) The three layers of the EM module with the accordion geometry show. (b) Orientation of EM cells in the barrel and endcap relative to the IP. Cells are orientated to point back to the IP. (Figures taken from <sup>32</sup>)

## HADRONIC CALORIMETER

The ATLAS HCAL is directly outside the ECAL and is responsible for containing and measuring the energy of hadronic showers. The HCAL consists of 3 separate detectors covering different  $\eta$  regions, the tile calorimeter, the LAr endcap calorimeter (HEC) and the LAr forward calorimeter (FCal).

The tile calorimeter is a sampling calorimeter using steel absorbers and scintillating tiles as active material. The barrel tile calorimeter covers an  $\eta$  range of  $|\eta| < 1.0$  and two extended barrel tile calorimeter covers the  $0.8 < |\eta| < 1.7$  region. Both barrel and extend barrel calorimeters are divided in  $\phi$  into 64 modules each with  $\Delta\phi = 0.1$ . Each module is segmented in the radial direction with 3 layers. The 3 layers have an approximate thickness of 1.5, 4.1 and 1.8 nuclear interaction lengths ( $\lambda$ ) in the barrel and 1.5, 2.6, and 3.3  $\lambda$  in the extended barrel. Two sides of the scintillating tiles are read out by two separate photomultiplier tubes.

A Schematic view of a tile calorimeter module can be seen in figure 2.9

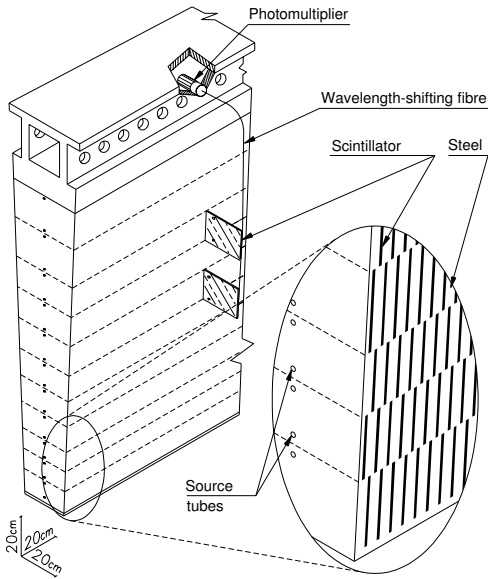


**Figure 2.9:** The tile calorimeter module with steel absorber, tile scintillators and photomultiplier readout. (Figures taken from <sup>32</sup>)

The HEC uses LAr as the active material and copper as the absorber material with copper plates interleaved with LAr gaps. The HEC is located directly behind the ECAL endcap and share the ECAL cryostat. Covering an  $\eta$  range of  $1.5 < |\eta| < 3.2$  the HEC overlaps slightly with the tile calorimeter and FCAL in order to minimize a drop in material density. Geometrically the HEC consists of two independent wheels per endcap with each wheel segmented in  $\varphi$  into 32 wedge shaped modules. Each HEC module is composed of cells with a size of  $\Delta\eta \times \Delta\varphi = 0.1 \times 0.1$  for the  $|\eta| < 2.5$  region and  $\Delta\eta \times \Delta\varphi = 0.2 \times 0.2$  in higher eta regions. The HEC model is also segmented longitudinally into two sections making a total of 4 layers. The combined depth of all 4 layers is approximately 10 interaction lengths.

The FCal is an LAr sampling calorimeter that extends the  $\eta$  coverage of the HCAL to 4.9. A compact design with very small LAr gaps was chosen for this high flux region. The FCal is segmented in the longitudinal direction with 3 distinct modules. The absorber material is copper for the first module and tungsten in the last two. The copper absorber is optimized for EM measurements while the tungsten is predominantly designed for hadronic interactions. The 3 modules combined achieves a depth of 10 nuclear interaction length.

### 2.2.3 THE MUON SPECTROMETER

The muon spectrometer consist of three layers of precision tracking chambers to track the path of muons in the bending  $\eta$  direction. The precision tracking chambers is composed mainly of the Monitored Drift Tube (MDT) detector with the Cathode Strip Chamber (CSC) detector used in the forward region. Alongside the precision trackers are fast trigger chambers, the Resistive Plate Chambers (RPC) in the barrel and the Thin Gap Chambers (TGC) in the endcap.

The configuration of the muon system is shown in figure 2.10

Eight air core superconducting toroid magnets in the barrel and eight superconducting toroid magnets in the endcaps provide 1.0 Tm to 7.5 Tm of bending power in the MS volume. The barrel magnets cover an  $|\eta|$  range of 1.4 and the endcap magnets cover an  $|\eta|$  range from 1.6 to 2.7. The area between  $1.4 < |\eta| < 1.6$  is called the transition region and has a mixed magnetic field from both the barrel and endcap. The endcap magnets are offset from the barrel magnets by 22.5 degrees in the  $\phi$  direction to allow a smoother magnetic field in this region. The configuration of the magnets is shown in figure 2.11

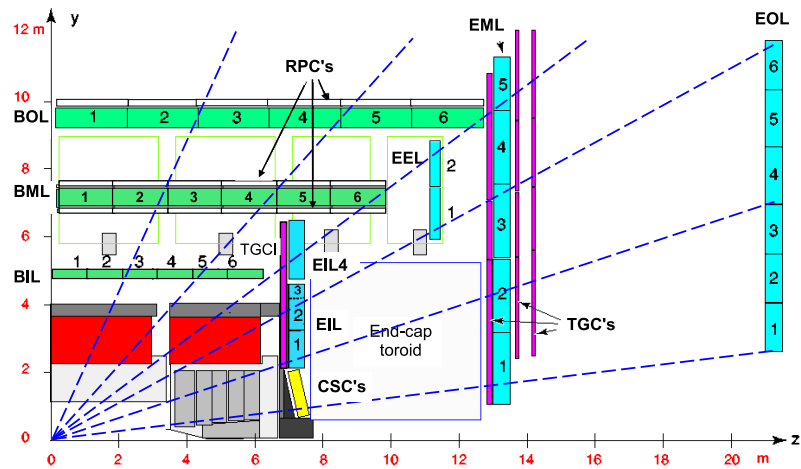


**Figure 2.10:** Cutaway view of the ATLAS Muon Spectrometer. (Figure taken from <sup>32</sup>)

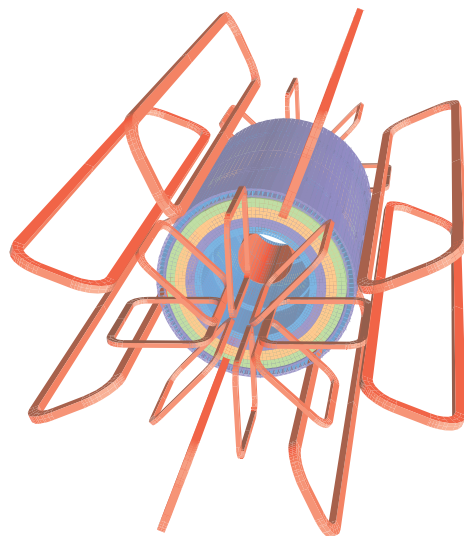


**Figure 2.11:** Geometry of the barrel and endcap toroid magnets. The cylinder represents the calorimeter. (Figure taken from <sup>32</sup>)

The MS is designed to be able to detect muon candidates with a wide range of momenta from 3 GeV to 3 TeV with standalone muon momentum resolution of  $\sigma_{p_T}/p_T = 10\%$  at a  $p_T$  of 1 TeV. The open design of the MS minimizes multiple scattering after the calorimeter and gives a large lever arm for high momentum resolution.

## MUON PRECISION TRACKING

The ATLAS MS system consists of 3 stations of muon precision tracking chambers at approximately 5 m, 7.5 m and 10 m radii in the barrel and 7.4 m, 14 m and 21.5 m in  $z$  the endcap covering an  $|\eta| < 2.7$ . Each chamber consists of 3 to 8 layers of MDT tubes. The only exception to this is the very high rate region in the inner endcap at high  $\eta$  which uses CSC technology.

MDT tubes are 3cm diameter aluminum tubes filled with Ar/CO<sub>2</sub> gas mixture with a tungsten-rhenium anode wire. Each tube has an intrinsic resolution of 80  $\mu\text{m}$  corresponding to a resolution of 35  $\mu\text{m}$  per chamber and offer measurements in the bending  $\eta$  direction.

CSC are multiwire proportional chambers with one layer of anode wires in the bending plane and two layers of cathode strips. The position of the track is obtained by interpolation between the signal on neighboring cathode strips. The CSC wire signals are not read out. The strips are perpendicular to one another with 5.31mm (5.56mm) pitch in the bending plane and 12.5 mm (21.0 mm) for small (large) chambers. This offers an 60  $\mu\text{m}$  resolution per plane in the bending plane and about 5 mm resolution in the non-bending plane.

The structure of MDT tubes and CSC chambers can be seen in figure 2.13 and 2.13 .

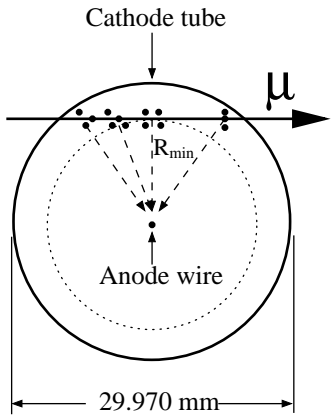


Figure 2.12: Schematic Representation of MDT tubes (Figures taken from <sup>32</sup>)

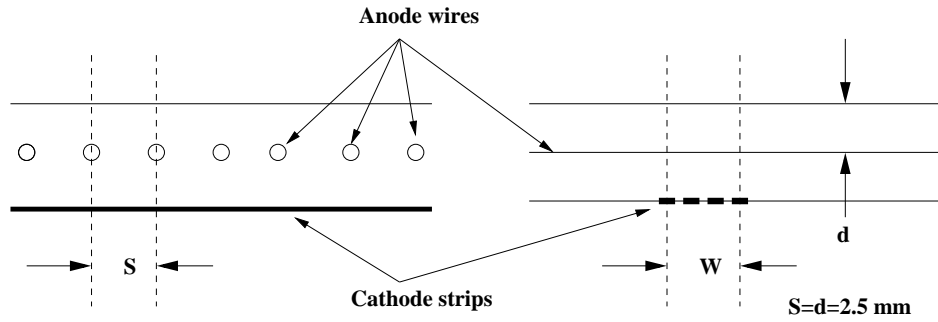


Figure 2.13: Schematic Representation of CSC chambers. (Figures taken from <sup>32</sup>)

## MUON TRIGGER CHAMBERS

The ATLAS MS also features a system of fast trigger chambers consisting of three stations of Resistive Plate Chambers (RPC) in the barrel and 4 stations of Thin Gap Chambers (TGC) in the endcap. The MS triggering system provide triggering up to an  $\eta$  of 2.4. The RPCs are placed below and above the middle MDT station and outside the outer MDT barrel station. The TGC stations are arranged with one station in front of the inner endcap precision tracking wheel and 3 stations split in front and behind the middle endcap MDT wheel. The trigger searches for fast coincidences between

the layers along the expected trajectory of a muon. Different maximum deviation from the straight path is allowed for triggers with different thresholds momenta.

In Run 2, muon triggers in the endcap also require coincidences in the inner layer of the TGC to reduce rates of fake triggers due to particles interacting with beam shielding in the forward region.

A schematic of the muon trigger system is given in figure 2.14.

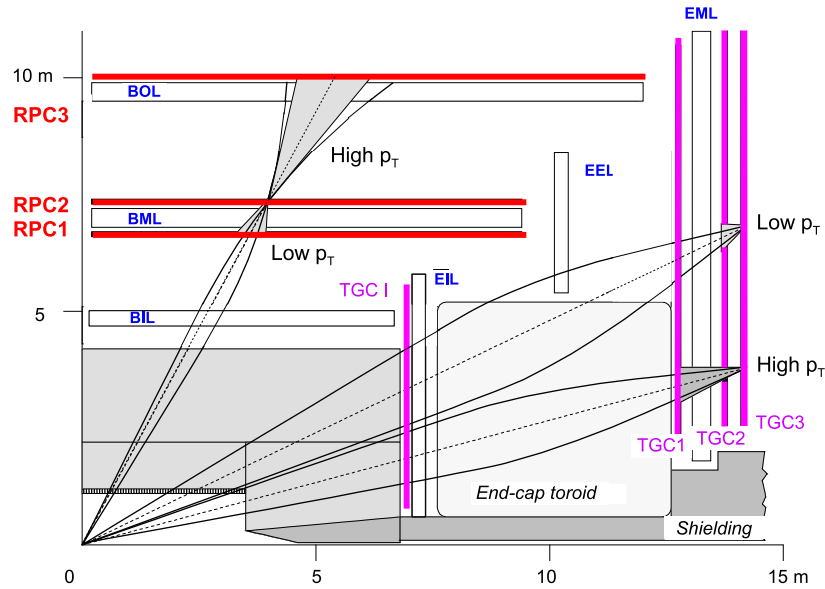


**Figure 2.14:** Schematic of the ATLAS muon trigger system. The coincidence windows for muons of different  $p_T$  is shown. (Figure taken from <sup>32</sup>)

# 3

## Object Reconstruction at ATLAS

### 3.1 INNER DETECTOR TRACK RECONSTRUCTION

Many reconstructed physics objects depend on tracking information in the inner detector (ID). ID track information is combined with the EM calorimeter and Muon spectrometer to identify and measure the momenta of electrons and muons. Hadronic jets use ID tracks to determine if the jet originated from a heavy flavored hadron with b-quarks or only light flavored hadrons. ID tracks are

also crucial to identify whether objects originate from the interesting hard scattering interaction or a less interesting pileup interaction.

Two types of inner detector tracks are reconstructed, primary tracks and secondary tracks. Primary tracks originate from the interaction point (IP) and are meant to reconstruct the trajectories of charged particles originating directly from the proton proton collisions. Secondary tracks target charged particles originating in the ID from secondary decays and interactions such as  $\gamma \rightarrow e^+e_-$  conversions.

Primary tracks are reconstructed in inside out fashion using the *NEWT* algorithm.<sup>33</sup> First seed segments are created from triple space points in the silicon layers. Each pixel cluster correspond to a single 3D space point. Two SCT clusters on the same layer must be combined to form a 3D space point because each SCT cluster only provide 2D position information.

The space point seeds can come from all pixel (PPP), all SCT (SSS) or two Pixel and two SCT (PPS) space points. PSS space points are rejected due to high fake rates.

Starting from the original seed, track reconstruction is performed layer by layer through the inner detector. Hits are added to the track one layer at a time from the inside out. Any ambiguities for shared hits are resolved using a strategy that penalizes less precise tracks. Merged clusters in the pixel are split using a set of trained neural networks.

Secondary tracks are reconstructed from the outside in. Segments in the TRT are reconstructed and then extended inwards by adding silicon hits.

### 3.2 VERTEX RECONSTRUCTION

On average around 25 proton-proton interactions occur in every beam crossing in Run 2. There different proton proton interactions are spread out  $Z$  coordinate in the detector because the finite bunch length at the LHC. We can reconstruct the charged particle tracks that originate from the different p-p interactions. By tracing back multiple charged particle tracks to the beam line we are able to reconstruct the original interaction position. We are able to separate objects that originate from the interesting hard scattering p-p interaction from other pileup interactions by reconstructing all the interaction vertexes in the same event.

A subset of reconstructed ID tracks are first selected and used to reconstruct the vertexes. In Run 2 tracks must satisfy:

$$p_T > 400 \text{ MeV}$$

$$|\eta| < 2.5$$

number of silicon hits  $\geq 9$  if  $|\eta| \leq 1.65$  or  $\geq 11$  if  $|\eta| > 1.65$

IBL hits + B Layer hits  $\geq 1$

maximum 1 shared module (1 shared pixel hit or 2 shared SCT hit)

pixel holes = 0

SCT holes  $\leq 1$

A vertex seed is found by searching for the global maximum in the  $Z$  coordinate of reconstructed tracks. The vertex position is found by using a fitting algorithm called the *adaptive vertex fitting* algorithm<sup>14,36</sup> that is robust to having additional noise and outlier tracks. Adaptive fitting determines

the vertex position using a least squared fitting method, but gives the outlier tracks lower weights in the fit.

The central position is fitted iteratively with each new fit a new vertex center is found and new set of weights is found. The weighting function changes every iteration according to a predeterminate way ultimately approaching a step function where a track has either 0 or 1 weight. The final set of tracks selected is fitted to determine the final position and uncertainty of the vertex.

This method of lowering the weight of outlier tracks in each fit and decrease the weight in iteration after iteration is called *determinist annealing*.<sup>36</sup> The procedure is analogous to repeatedly heating and cooling metal in a forge to make the crystal lattice in the metal more regular. At each iteration the heated temperature is lower then the last finally arriving at the final product.

After determining the vertex position, all tracks within  $7\sigma$  of the vertex is considered to be associated with the vertex. The conservative estimate of  $7\sigma$  is used to avoid one energetic vertex being split into two during reconstruction. Tracks incompatible with the vertex are then used to form a new vertex seed. This process is repeated until all tracks are clustered into vertexes or no additional vertexes can be found. Vertexes are required to have at least two associated tracks.

The vertex with the highest total momenta summed over all associated tracks is labeled the primary vertex and is identified as the vertex of the hard scattering interaction. All other vertexes are referred to as pileup vertexes.

### 3.3 HADRONIC JETS

Energetic partons carrying color charge that are produced in the initial hard scattering will quickly hadronize and then fragment into additional hadrons. The result is a shower of charged and neutral hadrons referred to as parton shower. The parton shower leaves a roughly conical energy deposit in the electromagnetic and hadronic calorimeter and multiple associated tracks in the inner tracker. Some energy may even be deposited in the muon spectrometer if the initial hadron is energetic enough. This detector signature is referred to as a jet.

Identification and reconstruction of hadronic jets is very important for many different detector signatures but especially for our analysis. Of key importance is the correct reconstruction of the energy of the initial hadron. The reconstruction of jets and the calibration of the jet's energy is described in sections 3.3.1 and 3.3.2 below. Also important is the rejection of jets resulting from proton-proton interactions that are not from the hard scattering and identifying jets resulting from heavy flavour b-quarks described in section 3.3.3 and ??.

#### 3.3.1 HADRONIC JET RECONSTRUCTION

Hadronic jets are reconstructed by clustering energy deposits in the calorimeter. This procedure involves multiple steps that are described below.

First, clusters of energy deposits are formed by clustering all topologically connected calorimeter cells around seed cells that pass the  $4\sigma$  signal above noise threshold. These 3D clusters are referred to as topological clusters (topo-clusters).<sup>2,12</sup> For each cluster, neighboring cells around the seed cell

are added to the cluster if they pass  $2\sigma$  signal over noise threshold. Next any cells neighboring any of the cluster cells with above  $2\sigma$  signal over noise ratio is also added. This step is repeated until no neighboring cells pass the  $2\sigma$  signal over noise threshold. At this stage, one last round of neighboring cells is added regardless of the amount of signal to noise ratio in those cells.

Topo-clusters are then grouped into jets according to the  $\text{anti} - k_t$  algorithm. The  $\text{anti} - k_t$  algorithm groups objects according to the distance measure  $d_{ij}$  defined in equation ?? with parameter  $p = -1$ . All objects within  $d_{ij}$  less than  $d_{iB} = k_{Ti}^{2p}$  are grouped into a single jet.

$$d_{ij} = \min(k_{Ti}^{2p}, k_{Tj}^{2p}) \frac{(\Delta\eta_{ij}^2 + \Delta\phi_{ij}^2)}{R^2} \quad (3.1)$$

The algorithm can best be explained by examining an example case. If a hard object  $i$  exists and is surrounded by only soft objects  $j$  then  $d_{ij}$  equals  $k_{ij}^{2p} (\frac{\Delta R^2}{R^2})$  for all  $j$  and  $\Delta R = \Delta\eta^2 + \Delta\phi^2$ .  $d_{ij}$  will always be less than any  $d_{ij}$  if both  $i$  and  $j$  are both soft and have the same  $\Delta R$  as  $i$  and  $j$ . Therefore, the  $\text{anti} - k_t$  algorithm effectively groups hard objects first before soft objects. A perfectly conical jet of radius  $R$  will be formed if no other hard objects are found within a cone of  $2R$ . If two hard objects exist within  $R < \Delta R_{i,2} < 2R$  of one another then two jets will be formed with energy cells split between the two. If two hard objects exist within  $\Delta R_{i,2} < R$  then they will both be grouped to within a single jet.

The  $\text{anti} - k_t$  algorithm is both infrared and collinear safe. Meaning the algorithm is insensitive to the radiation of additional soft particles and the collinear splitting of initial partons. Additional soft partons do not change the shape of the jets but the jet shape is flexible to accommodate the presence

of other hard radiation.

ID Tracks are associated with jets according to a *ghost association* procedure.<sup>26</sup> Tracks with the same direction and location as real ID tracks but infinitesimally low  $p_T$  are allowed to be clustered by the  $anti - k_t$  algorithm. If these tracks are assigned to the jet by the  $anti - k_t$  algorithm then the real track is associated with the jet. In this way, we can determine which tracks are associated with the track without disturbing the clustering of calorimeter energy. The same procedure of clustering infinitesimally low  $p_T$  objects is used to determine jet area.

### 3.3.2 JET CALIBRATION AND SYSTEMATICS

Both the electromagnetic and hadronic calorimeters on ATLAS are sampling calorimeters. The energy from the shower deposited in the absorber material is effectively lost because the absorber does not actively record a signal. Therefore the energy measured using the active material must be scaled up to compensate for this loss. For this reason and others including leakage of energy outside of the calorimeter edges and deposition of energy below the energy thresholds, reconstructed jets must be calibrated to determine the original hadron's energy.

A variety of both MC based and data based methods are used to calibrate hadronic jets. Figure 3.6 shows the steps in jet calibration for Run 2.<sup>3</sup>

First the individual topo-clusters in the jet are calibrated using MC to the energy scale of EM showers.<sup>3</sup> This corresponds to the EM calibration scheme. Next the origin of the reconstructed jet is set to the primary vertex instead of the default detector center.

A correction for energy deposited by pileup interactions are then applied.<sup>3</sup> The correction is

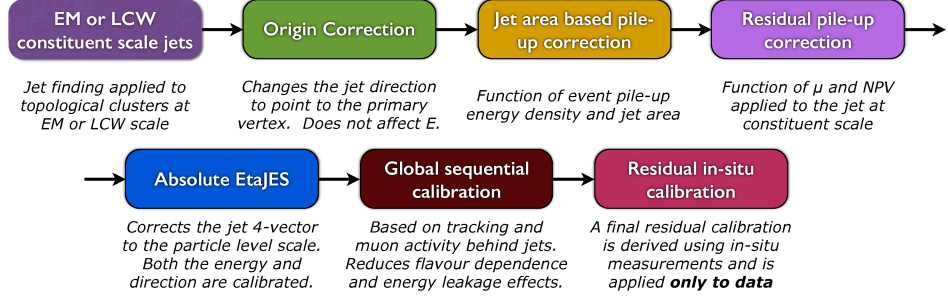


**Figure 3.1:** Flow chart of the steps involved in jet calibration

based on the measurement of average energy originating from pileup  $\varrho$  multiplied by the measured jet area. The pileup energy density is defined in equation 3.2 and determined by measuring the median energy density of  $R = 0.4 k_t$  jets found in the central  $|\eta| < 2.0$  part of the calorimeter. The  $k_t$  algorithm preferentially cluster soft objects first instead of hard objects like the  $anti - k_t$  algorithm and is more sensitive to soft pileup radiation. No  $p_T$  thresholds are applied to the reconstructed  $k_t$  jets as we are trying to measure soft objects.

$$\varrho = \text{median}\left\{\frac{p_{T_i}^{k_t \text{ jet}}}{A_i^{k_t \text{ jet}}}\right\} \quad (3.2)$$

It is noted that the jet energy response still has a dependence on pileup after this area based correction has been applied. The sources of this dependence is attributed to the incomplete cancelation of in-time and out-of-time pileup.<sup>ii</sup> For example, events with a low number of reconstructed vertexes ( $N_{PV}$ ) but in a run with high average number of interactions per bunch crossing ( $\langle \mu \rangle$ ) may receive relatively large amounts of out-of-time pileup compared to in-time pileup. This effect is also parameterized using MC by using the constants  $\alpha$  and  $\beta$ .

The area based pileup energy correction is subtracted along with two other residual corrections.

The total pileup correction to jet  $p_T$  is given in equation ??.

$$p_T^{corr} = p_T - \varrho \times A - \alpha \times (N_{PV} - 1) - \beta \times \langle \mu \rangle \quad (3.3)$$

In the next step, the jet energy scale (JES) is applied. JES is a scale factor which relates the reconstructed jet energy with the true jet energy. JES is calibrated using a number of MC and data driven methods. The JES is derived from an inclusive jet MC after pileup and origin corrections are applied.

An up to 8 percent difference between the energy responses of gluon and light quark jets remains after the above JES calibration.<sup>ii</sup> The difference is due to a number of reasons including the factor of  $\approx 2$  difference in color charge between quarks and gluons. A Global Sequential Correction scheme (GSC) is applied to account for this deference and correct for other detector based issues.<sup>io</sup> GSC corrections uses information on the topology of energy deposits, associated inner detector tracks and activity in the muon spectrometer behind the jet. ID Tracking information is used to reduce the flavour dependence of the calorimeter response to jets because gluon initiated jets tend to have a wider profile and more tracks. Muon spectrometer information is used to better estimate high energy jets which penetrate the full depth of the calorimeter. Information on the relative amount of calorimeter energy deposited in specific layers is used to improve the jet energy resolution.

Lastly further corrections to the jet energy response are obtained by measuring the balance between jets and some other reference objects such as a photon, a  $Z$  boson or other jets directly in data.<sup>7,6</sup> The  $p_T$  balance between jets and the reference objects are measured in data and compared

to the MC. A residual correction is applied by the data over MC ratio based on equation ???. Systematic uncertainties on the jet energy responses including those on the jet energy scale and jet energy resolution are also derived using these data driven methods.

$$\frac{R_{data}}{R_{MC}} = \frac{\langle p_T^{jet} / p_T^{ref} \rangle_{data}}{\langle p_T^{jet} / p_T^{ref} \rangle_{MC}} \quad (3.4)$$

### 3.3.3 PILEUP JET REJECTION AND JET VERTEX TAGGER

It is imperative to be able to distinguish between jets origination from the hard scattering interaction (hard scattering jets) and those originating from other proton-proton interactions (pileup jets) in the high luminosity environment. Pileup jets may originate from both the on average 25 additional p.p. interactions in the same bunch crossing or from interactions in other beam crossing. We distinguish between the hard scattering jets from pileup jets using a discriminant known as jet vertex tagger (JVT).<sup>5</sup>

For our analysis we require a jet vertex tagger value greater than 0.59. This corresponds to a 92 percent efficiency for jets originating from the hard scattering interaction and a 2 percent fake rate from pileup jets, if the jet has  $|\eta| < 2.4$  and  $p_T < 60$  GeV.

The JVT discriminant is based on two variables  $corrJVF$  and  $R_{pT}$  defined in equations ?? and 3.6.

$$corrJVF = \frac{\sum_i p_T^{trk_i}(PV_o)}{\sum_l p_T^{trk_l}(PV_o) + \frac{\sum_{n \geq 1} \sum_l p_T^{trk_l}(PV_n)}{k \pi_{trk}^{PU}}} \quad (3.5)$$

$$R_{pT} = \frac{\sum_i p_T^{trk_i}(PV_o)}{p_T^{jet}} \quad (3.6)$$

The *corrJVF* variable roughly corresponds to the fraction of a jet's ID track  $p_T$  that originate from the hard scattering vertex.  $\sum_i p_T^{trk_i}(PV_o)$  is the sum of all jet's associated track  $p_T$  that originate from the primary vertex  $PV_o$ . The quantity  $p_T^{PU} = \sum_{n \geq 1} \sum_l p_T^{trk_l}(PV_n)$  is the total amount of a jet's associated track  $p_T$  that originates from pile up interactions.  $p_T^{PU}$  is divided by  $k n_{trk}^{PU}$  to correct for the fact that  $\langle k n_{trk}^{PU} \rangle$  will increase linearly with the number of pileup vertexes  $n_{trk}^{PU}$ . This makes the variable *corrJVF* roughly independent to the number of reconstructed vertexes. The value  $k$  is set to an arbitrary 0.01 and the discriminating power of JVT was found to be independent of the choice of  $k$ .

$R_{pT}$  is defined as the total track  $p_T$  of all associated tracks that originate from the primary vertex  $PV_o$  divided by the fully calibrated jet  $p_T$ . The calibrated jet  $p_T$  includes pileup subtraction.  $R_{pT}$  peaks sharply at zero for pileup jets. On the other hand,  $R_{pT}$  corresponds to roughly the charged  $p_T$  fraction in hard scattering jets.

The JVT discriminate constructs a 2D likelihood based on these variables. The JVT discriminate determines the probability that a jet will be a hard scattering jet using the k-nearest neighbor (kNN) multivariate technique<sup>37</sup> trained on a  $20 < p_T < 50$  GeV and  $|\eta| < 2.4$  MC sample of hard scattering and pileup jets. The k-nearest neighbor (kNN) algorithm is robust relative to local fluctuations in sparsely populated regions.

### 3.3.4 JET QUALITY AND JET CLEANING

Several variables are useful in discriminating between real hadronic jets and fake jets not coming from proton-proton interactions. The sources of fake jets include noise in the LAr and Tile calorimeters, beam induced backgrounds and cosmic raw showers. These variables can be divided into three broad categories: variables quantifying the EM and hadronic calorimeter energy ratio, ID track based variable sand variables based on the pulse shape of the LAr calorimeters. Detailed descriptions of the variables used can be found in<sup>13</sup> a brief summary will be given here.

Energy ratio variables can reject calorimeter noise and beam induced backgrounds and energy deposited from cosmic rays. Jets originating from beam induced backgrounds tend to concentrate more energy in a few longitudinal layers compared to jets from proton-proton collisions. Multiple variables corresponding to the fraction of jets energy deposition in any one section along the expected direction of the shower relative to the total energy deposition are useful in discriminating against fake jets.

Energy ratio variables include:

$f_{EM}$ : ratio of EM calorimeter energy to total jet energy

$f_{HEC}$ : ratio of HEC calorimeter energy to total jet energy

$f_{max}$ : maximum energy fraction in any single calorimeter layer

ID track based variables are useful because tracks can be matched to the primary vertexes in good jets. Fake jets have low fraction of tracks which can be matched to primary vertexes.

list of track based variables include:

$f_{ch}$ : ratio of the scalar sum of ID track  $p_T$  where ID track must originate from the primary vertex to jet  $p_T$ . approximately the fraction of jet energy carried by charged particles.

$f_{ch}/f_{max}$ : ratio of  $f_{ch}$  and  $f_{max}$ , the maximum energy fraction in any single calorimeter layer

Pulse shape in the LAr should be consistent with those of a particle shower in good jets. A quality variable  $Q_{cell}^{LAr}$  measures the quadratic difference between expected and actual pulse shapes in each LAr cell. Quality variables based on the fraction of cells in a jet with poor quality and the average quality is found to provide discrimination power against LAr noise.

LAr pulse shape variables include:

$\langle Q \rangle$ : weighted average of pulse quality of LAr cells ( $Q_{cell}^{LAr}$ ) in a jet. Normalized to  $0 < \langle Q \rangle < 1$ .

$f_Q^{LAr}$ : Fraction of energy in cells with poor quality pulse shapes in EM LAr Calorimeter

$f_Q^{HEC}$ : Fraction of energy in cells with poor quality pulse shapes in hadronic endcap calorimeters (HEC) which also use LAr technology.

$E_{neg}$ : total energy of all cells with negative energy

A jet satifying any one of the following criteria is considered a **BadLoose** jet. If any baseline jet in the event is found to be **BadLoose** then the entire event is rejected. This procedure is called jet cleaning and ensures that the  $E_T^{\text{miss}}$  reconstruction is not done with a noisy calorimeter or any bad quality jets.

A jet is considered a **Loose** jet if is not identified as a **BadLoose** jet. This is the jet quality tag used for signal jets in most ATLAS analysis including this analysis.

$$f_{EM} > 0.5 \text{ and } |f_Q^{HEC}| > 0.5 \text{ and } \langle Q \rangle > 0.8$$

$$E_{neg} > 60 \text{ GeV}$$

$f_{EM} > 0.95$  and  $f_Q^{LAr} > 0.8$  and  $\langle Q \rangle > 0.8$  and  $|\eta| < 2.8$

$f_{max} > 0.99$  and  $|\eta| < 2.0$

$f_{EM} < 0.05$  and  $f_{ch} < 0.05$  and  $|\eta| < 2$

$f_{EM} < 0.05$  and  $|\eta| \geq 2$

### 3.3.5 IDENTIFYING JETS ORIGINATING FROM HEAVY FLAVOR HADRONS

Hadrons containing b-quarks have long lifetimes, around 1.5 ps or a  $c\tau$  of around 450  $\mu\text{m}$ . The long flight distance allows use to reconstruct tracks that are inconsistent with originating from the primary vertex and perhaps reconstruct secondary vertexes characteristic of b-hadron decays. The typical b-hadron decay consist of at least one vertex displaced from the point of initial hard scattering.

Three separate algorithms have been setup to distinguish jets origination from b-hadrons (b-jets) from light quark and c-hadron (c-jets). A brief description will be given on the logic of each algorithm. The details can be found in <sup>17</sup> and <sup>9</sup>.

The first algorithm is based on track impact parameters for high quality tracks that are associated with jets. The discriminate is computed as a sum of the log likelihood ratio of each accepted track in the vertex or  $\sum_i \ln(\frac{p_b}{p_{light}})$ , where i sums over all accepted tracks in the jet and  $p_b$  is the PDF for a b-jet and  $p_{light}$  is the PDF for a light jet. The PDF uses transverse and longitudinal impact parameters  $d_0$  and  $z_0$  as observables and are derived from MC.

The second algorithm seeks to reconstruct the secondary vertex associated with the b-hadron decay. This algorithm has the advantage that if a secondary vertex is consistent with the decays of

long lived hadrons that do not contain b-jets such as  $K_s$  or  $\Lambda$  or photon conversions then the vertex maybe rejected. For example, secondary vertexes with a mass greater then 6 GeV are inconsistent with b decays and are rejected. Variables based on the secondary location and the total energy of the secondary vertex and the mass of the secondary vertex can all be used to discriminate b-jets from light-jets and c-jets.

The third algorithm attempt to reconstruct the full b-hadron decay chain and is called the decay chain multi-vertex reconstruction algorithm. The algorithm uses a Kalman filter to determine the common line on which the primary vertex and the bottom and charm vertexes lie.

The output of the three algorithms are all combined into a multivariate discriminant called MV2. MV2 uses a boosted decision tree (BDT) algorithm<sup>37</sup> to gain better separation power for different jet flavors then any one single algorithm is able to achieve. This analysis uses the MV2oc10 discriminant to tag b-jets. MV2oc10 is selected as it gives the best balance between light jets and c-jet rejection the given b-tagging efficiency.

The distribution of the MV2oc10 discriminant for light, charm and b-hadrons can be seen in figure 3.2. We make a selection at  $MV2c10 > 0.6459$  which corresponds to approximately 77% b-tagging efficiency with a factor of 134 reject rate for light jets. The b-tagging efficiencies and mis-tag rates have been calibrated by the ATLAS flavor tagging group.

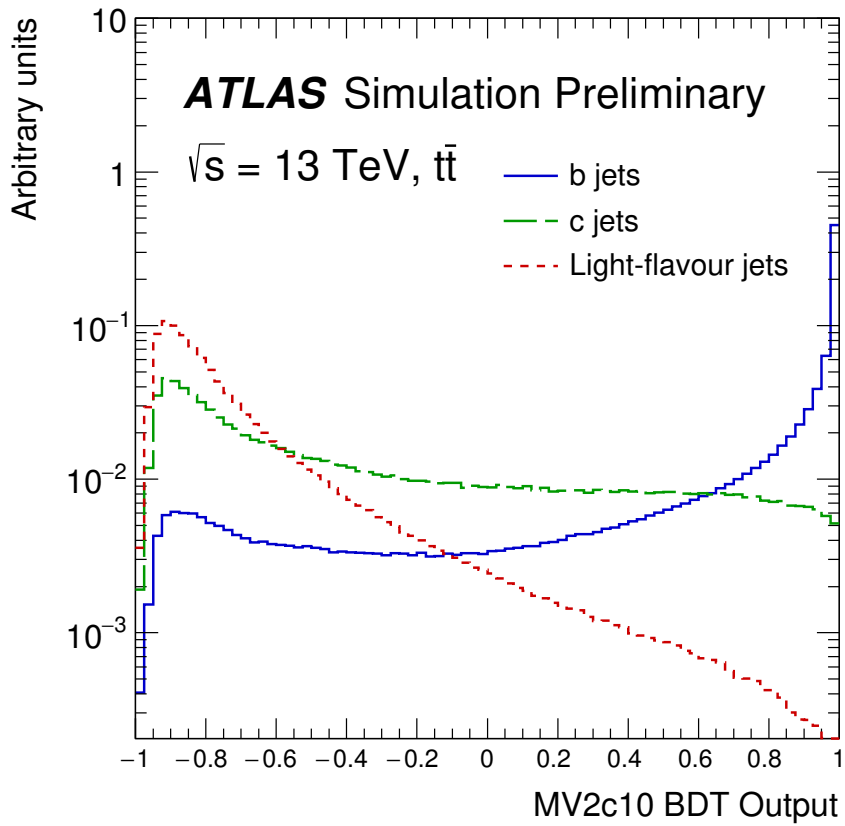


**Figure 3.2:** Distribution of the MV20c10 multivariate discriminate used for tagging b-jets.

### 3.4 ELECTRON AND PHOTONS

#### 3.4.1 ELECTRON AND PHOTON RECONSTRUCTION

Both electron and photon reconstruction starts from clusters of energy deposits in the electromagnetic calorimeter. The EM calorimeter is first divided into a grid of towers each with the size of  $\Delta\eta \times \Delta\phi = 0.025 \times 0.025$ . The energy of all cells in the longitudinal layers inside each tower is summed

into the total tower energy.

The EM clusters are seeded by towers with energy above a certain threshold. A sliding-window algorithm then groups the energy towers near the seed into EM clusters.<sup>15,28</sup> The window width is  $3 \times 7$  towers in the barrel and  $5 \times 5$  towers in the endcap. The reconstructed cluster therefore has a size of  $\Delta\eta \times \Delta\phi = 0.075 \times 0.175$  in the barrel and  $0.125 \times 0.125$  in the endcap. The same window size is used for electrons and photons to ensure better cancelation of systematics when using electrons to measure photon response.<sup>15</sup> The window position is adjusted so that the reconstructed cluster energy is the local maximum. The different cluster sizes were optimized for the different energy distribution in the barrel and endcap calorimeters while minimizing pileup and noise contributions.<sup>15</sup>

Identified clusters are then matched to reconstructed ID track using track and cluster position. ID tracks are required to have a minimum number of pixel and total silicon hits. Clusters are considered an electron candidate if a single well-reconstructed ID track that originates from a vertex is found. The cluster is considered an unconverted photon candidate if no tracks are found. The cluster is considered a converted photon candidates if two opposite signed tracks that are collinear, originate from the interaction point, and are consistent with electrons are present. The cluster is also considered a converted photon if a single track is present but the track lacks hits in the IBL of the pixel detector.

Furthermore, electron and photon candidates must satisfy a set of criteria. These variables include descriptions of the EM shower shapes, amount of hadronic activity behind the EM calorimeter and properties of associated tracks. More details on electron and photon identification are given in section 3.4.2 and ??.

### 3.4.2 ELECTRON IDENTIFICATION AND QUALITY

Electron identification in Run 2 is based on a likelihood algorithm that depends on a list of kinematics variables including EM shower shape, EM vs hadronic activity ratio, activity in the TRT and properties of the associated track. The list of variables included in the likelihood can be found in <sup>16</sup>. A multivariate technique is used to ensure the PDF estimation is robust in low statistics regions in the high dimensional space. Probability density functions (PDF) are formed for electrons and non-electron backgrounds for a set of discriminating variables used on MC. The probability of the candidate being an electron is calculated using the two PDFs.

Electron identification is split into categories *very loose*, *loose*, *medium*, and *tight*. Each operating point is a sub-set of another. For example, all tight electrons are also medium electrons and so on. 25 GeV tight electrons have an efficiency of 78 percent and fake rate of 0.3 percent. 25 GeV loose electrons have an efficiency of 90 percent and fake rate of 0.8. The efficiency increases with  $E_T$  while the fake rate decreases. <sup>16</sup>

Because some shower shape distributions tend to broaden with the number of pileup collisions, the cut on the likelihood discriminant is loosened as a function of the number of vertices. This is done to preserve the identification efficient at high pileup and does not drastically increase the amount of background. <sup>16</sup>

### 3.4.3 PHOTON IDENTIFICATION AND QUALITY

Photon identification is based on the shower shape and the amount of hadronic activity behind the EM cluster. The energy deposited in the cells in the first and second layer of the EM calorimeter are important for distinguishing the EM shower originating from photons and those originating the neutral mesons such as  $\pi_0$ . A detailed list of the discriminating variables used can be found in<sup>18</sup>.

The requirements are different for converted and unconverted photon candidates to account for the different expected shower shapes. The requirements are differ in pseudorapidity intervals to account for the varying amount of material upstream of the calorimeter. The requirements were optimized using a multivariate technique.<sup>37</sup>

Two working points are included a loose and a tight selection. The loose ID exploits the variables only in the EM calorimeter and in the hadronic calorimeter layer and is typically used for the trigger and for background studies. The tight ID uses the full granularity of the EM calorimeter, including the fine segmentation of the first sampling layer, and tightens requirements on the variables used in the loose selection. The tight working point is the one generally recommended for physics analysis and photons used in this analysis are tight photons.

### 3.4.4 ELECTRON AND PHOTON ENERGY CALIBRATION

Electron and photon energy must also be calibrated because of the non-compensating nature of the EM calorimeter. At the same time, the correctly estimating the amount of material upstream of the calorimeter is also important. Typically a 100 GeV electron will deposit between a few percent

to 20 percent of its energy before it reaches the calorimeter.<sup>15</sup> Also about 5 percent of the electron energy may be deposited outside of the cluster. Electron and photon calibration accounts for all these affects to get an estimate of the true electron and photon energy. The calibration procedure follow the steps indicated in figure 3.3.

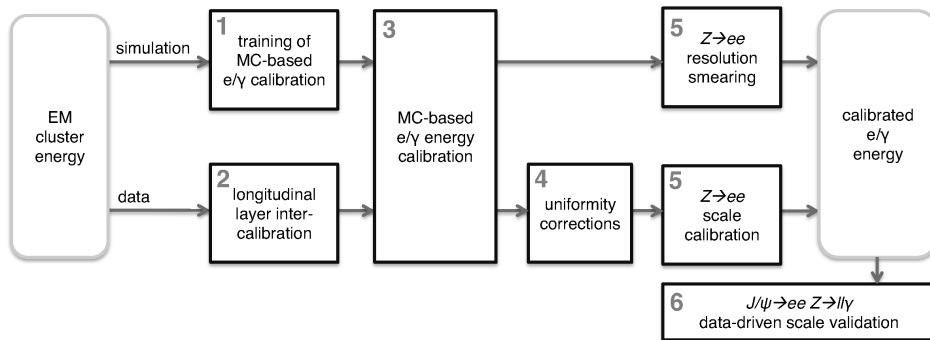


**Figure 3.3:** Flow chart of the steps involved in the calibration of the energy response of electrons and photons<sup>28</sup>

The EM clusters are first calibrated to the original electron or photon energy using a multivariate technique<sup>37</sup> based on MC simulations.<sup>15,28</sup> The MC based calibration uses information on the EM cluster properties such as the longitudinal shower shape and information from any associated ID track. The response is different for electrons, converted photons and unconverted photons.

The longitudinal layers of the EM calorimeter must be calibrated relative to one another. Specifically, the relative energy response of the presampler and the first and second layer must be validated by using data. These cannot be done at the cluster level as clusters sum over all longitudinal layers. The intercalibration of the first and second layers of the EM calorimeter is performed with  $Z \rightarrow \mu\mu$  decays. This is because the muon energy deposit in the calorimeter are relatively insensitive to the amount of material upstream of the EM calorimeter. The presampler energy scale is calibrated using

W and Z decays. The ratio of data to MC in the presampler energy detected in electrons from W and Z to electron decays is used as a scale factor. This accounts for mismodeling of the amount of material in front of the presampler.

A number of corrections are then applied to account for differences between simulation and data such as regions with non-optimal HV and geometrical affects. Finally a correction is applied to ensure that the  $Z \rightarrow ee$  modeling in simulation agrees with data. The same scale factors derived for electrons from  $Z \rightarrow ee$  is applied to photons but additional photon-specific systematic uncertainties are also applied.

Cross-checks of the electron and photon calibration is performed with  $J/\psi \rightarrow ee$  and  $Z \rightarrow ll\gamma$  events in data after all energy corrections are applied.

## 3.5 MUONS

### 3.5.1 MUON INNER DETECTOR AND MUON SPECTROMETER TRACK RECONSTRUCTION

Muons are first reconstructed independently in the inner detector (ID) and muon spectrometer (MS). Later information from the ID, MS and calorimeter are combined form different types of reconstructed muons. The type of reconstructed muon depend on the type of information available to be combined.<sup>30</sup>

Muon tracks in the ID are reconstructed using the same algorithm for reconstructing all charged particles summarized in section 3.1.

Muon tracks reconstructed in the MS start by form segments in each individual muon chamber.

A Hough transform is used to search for hits aligned in the bending  $\eta$  plane of the detector.<sup>38</sup> The MDT segments are reconstructed by performing a straight line fit. The RPC or TGC hits are associated with the MDT segment and measure the coordinate in the non-bending  $\phi$  plane. Segments in the CSC are constructed using a combinatorial search in  $\eta$  and  $\phi$  planes. Segment reconstruction require that the segments are loosely compatible with a track originating from the collision point.

Muon spectrometer track candidates are built by fitting together the segments from different muon detector layers. The algorithm start from seed segments from the middle layer of the MS because the middle layer has more TGC and RPC hits available. The algorithm searches for other segments in the other layers by matching their relative positions and direction. Segments are added to the track candidate if they satisfy a set of criteria based on hit multiplicity and fit quality. Afterwards seed segments from the middle layer have been exhausted, segments in the inner and outer layers are also used as seeds to search for their own tracks.

At least two matching segments are required to build a track, except in the barrel to endcap transition region. In the transition region, a single high quality segment with both MDT and trigger hits can be considered a track.

At this point, the same segment can be in several track candidates. Overlap removal is then performed to either assign the segment to a single track or allow the segment to be shared between two tracks. Tracks that share two segments in the inner and middle layer are allowed if there are no shared hits in the outermost layer. This preserves the high efficiency of reconstructing two close by muons which can result from the two-body-decays of low-mass particles.

Once the track candidate is identified, the hits associated with each track candidate are fitted us-

ing a global  $\chi^2$  fit. Hits with large  $\chi^2$  are removed and the track is refitted without the outlier hits.

Additional hits consistent with the track trajectory can also be added to the track. Again the track is refitted if any new hits are added. A track candidate is accepted if the fitted  $\chi^2$  satisfies the selection criteria.

### 3.5.2 MUON COMBINED RECONSTRUCTION

Four different types of muons are reconstructed by combining information from the ID, MS, and calorimeters. The four different types of muons are defined below based on what subdetector information is used to reconstruct them.

Combined muons: Combine muons combine reconstructed ID and MS tracks using a global refit that uses all the hits from the ID and MS tracks. MS hits may be added or removed from the track to improve the fit quality. The matching between MS and ID tracks are done mostly in an outside in fashion. The MS track is used to extrapolate inwards and is matched to an ID track with energy loss in the calorimeter taken into account. The inside out matching approach where the ID track is extrapolated outwards is also used a complementary method.

Segment tagged muons: An ID track is combined with a MS segment in the MDT or CSC to form a segment tagged muon. The ID track is used to extrapolate to the MS to find matching segments. Segment tagged muons add reconstruction efficiency to muons that are either so low  $p_T$  that they pass only a single layer of muon detector or regions in the MS with gaps in coverage due to for example support structures.

Calorimeter tagged muons (Calo-tagged): Calo-tagged muons are built by combining an ID track with calorimeter energy deposits that are consistent with a minimum ionizing particle. Calo-tagged muons has the lowest purity rate of all reconstructed muons. However it recovers some efficiency in regions with none or low MS coverage such as the central  $|\eta| < 0.1$  region. The  $|\eta| < 0.1$  region is occupied by cabling and servicing to the calorimeter and inner detector and only has partial MS coverage. The calo-tagged muon identification algorithm is optimized for the  $|\eta| < 0.1$  region and a momentum range of  $15 < p_T < 100$  GeV.

**Extrapolated muons:** In extrapolated muons the muon trajectory is reconstructed using only the MS track and a loose requirement of compatibility with the interaction point. Extrapolated muons are used mainly to extend acceptance passed the coverage of the ID in the  $2.5 < |\eta| < 2.7$  region.

### 3.5.3 MUON QUALITY

Reconstructed muons are flagged as loose, medium or tight in terms of quality. The quality selections identify prompt muons originating from the interaction point and reject backgrounds which mainly consist of muons originating from leptonic pion and kaon decays.

The pion and kaon decays in-flight forming a muon in the inner detector that then gets reconstructed as a track in the MS. The ID track of the muon will have a distinct *kink* topology. The resulting combined track will have both poor fit quality and poor matching between ID and MS track momenta. Combined muon use the following variables to distinguish between high and low quality muons:

$q/p$  significance:  $q/p$  significance measure the compatibility of the ratio of charge and momentum ( $q/p$ ) of the the muons given by the ID and MS tracks. The quantity is normalized to the uncertainty on ( $q/p$ ) from the two tracks.

$\rho^t$ :  $\rho^t$  is the difference in  $p_T$  of the ID and MS tracks divided by the  $p_T$  of the combined track

fit  $\chi^2$ : The  $\chi^2$  of the fit to the combined track normalized to the degrees of freedom

Quality selections also require at least one Pixel hit and at least five SCT hits with fewer than three Pixel or SCT holes. If the track is located between  $\eta$  of 0.1 and 1.9, we also require at least 10 percent of TRT hits originally assigned to the track are still included in the final fit. Requirements

on MS hits are also made for combined muons. These requirements on track hits ensure a robust momentum measurement.

Muon quality are split into four categories; *Loose*, *Medium*, *Tight*, and *High- $p_T$* . Loose, medium and tight muons are inclusive of one another, where all tight muons are also included in the looser categories. Most analysis including this one uses medium muons to identify signal muons. We use signal muons in multiple one lepton control regions to estimate backgrounds. We use loose muons to veto on muons in the zero lepton signal and validation regions because of the higher muon reconstruction efficiency.

High- $p_T$  muons sacrifices reconstruction efficiency for better momentum resolution in muons with  $p_T > 100$  GeV and are used mainly for heavy resonances searches such as  $W\ell$  and  $Z\ell$ . We do not use high- $p_T$  muons and will not discuss their identification in detail. Detailed description of the loose, medium and tight muon categories are given below.

**Medium muons:** Medium muons are considered the default muons used in analysis at ATLAS. The identification algorithm is designed to minimize systematic uncertainties on momentum measurement and reconstruction efficiency. Only combined and extrapolated muons are accepted. Combined muons must have  $\geq 3$  hits in at least two separate layers. The only exception is in the central  $|\eta| < 0.1$  region where tracks can have at least one MDT layer but no more than one MDT hole is allowed. Extrapolated muons must have at least three MDT/CSC layers and are allowed only in the forward  $2.5 < |\eta| < 2.7$  region which lies outside of ID coverage.  $q/p$  significance must be less than 7 in combined muons to ensure good agreement between ID and MS and reject decay-in-flight muons originating from hadrons.

**Loose muons:** Loose muons identification is designed to maximize reconstruction efficiency while still ensuring high quality tracks. All combined and extrapolated muons must satisfy the same requirements as the medium muons. On top of this calo-tagged and segment tagged muons are also allowed in the  $|\eta| < 0.1$  region to increase efficiency. The majority of loose

muons are still combined muons with approximately 97.5% of all loose muons being combined muons in the  $|\eta| < 2.5$  region. The rest consist of 1.5% calo-tagged and 1% segment tagged muons.

**Tight muons:** Tight muons are optimized to maximizes muon purity but costs some reconstruction efficiency. Only combined muons with hits in at least two muon stations and satisfy the medium definition are accepted. The combined track fit's normalized  $\chi^2$  must also be less than 8. A two dimensional cut in  $q/\ell$  and  $q/p$  significance is also applied. The 2D cut is tighter for low  $p_T$  muons to have better background rejection in a regime where misidentification probability is higher.

### 3.5.4 MUON RECONSTRUCTION EFFICIENCY AND MOMENTUM CALIBRATION

Muon reconstruction efficiency and muon momenta calibrations are determined by studying narrow resonances decaying into muon pairs in data. A brief summary is given below and more details can be found in<sup>30</sup>.

Muon reconstruction efficiency is measured in data by using a tag and probe method using  $J/\psi \rightarrow \mu\mu$  or  $Z \rightarrow \mu\mu$  events. A well reconstructed muon (medium quality that fires the trigger) is considered the tag. Then a muon reconstructed using a different system to the one studied for example an bare ID track is considered the probe. We search to see if the probe is reconstructed as a muon. We can reject background processes by selecting for events who's tag and probe have an invariant mass and other kinematic features that are consistent with the narrow resonance .

The efficiency for medium and tight muons is a combination of two tag and probe measurements. First the probability of reconstructing a  $X$  muon is tested using a calo-tagged muon as the probe where  $X$  is a medium or tight muon. This essentially measure the probability of identifying

a MS track of sufficient quality given an ID track+calo-tagged muon exists. Then the probability of an ID track of sufficient quality is measured using the MS track as a probe. The total efficiency is given by equation 3.7.

$$\epsilon(X) = \epsilon(X|ID) \cdot \epsilon(ID) = \epsilon(X|CT) \cdot \epsilon(ID|MS) \quad (3.7)$$

We assume that  $\epsilon(ID) = \epsilon(ID|MS)$  or that the ID and MS track reconstruction occur independently of one another. We also assume that the X muon has the same probability of being reconstructed regardless of whether a calo-tagged muon was reconstructed or only an ID track was reconstructed  $\epsilon(X|ID) = \epsilon(X|CT)$ .

Run 2 muon reconstruction efficiency for loose and medium are shown in figure 3.4.

Muon momentum is calibrated to  $J/\psi \rightarrow \mu\mu$  or  $Z \rightarrow \mu\mu$  events in data. The  $p_T$  of individual tracks are corrected to account for any inaccuracies in the detector description such as the magnetic field, dimensions of the detector and the amount of energy loss in the calorimeters. Correction parameters are extracted using a likelihood fit to data with templates derived from MC. MS/ID alignment is also studied using special runs with no magnetic field. The correction parameters differ for different sections of  $\eta$  and  $\phi$  regions because of the different amount of magnetic fields and independent alignment performed in each section.

On top of the total correction to the central value of the  $p_T$ , the momenta resolution is also estimated using data. The MC is smeared such that the reconstructed di-muon mass peak agrees between data and MC. The muon momenta resolution is described according to equation 3.8

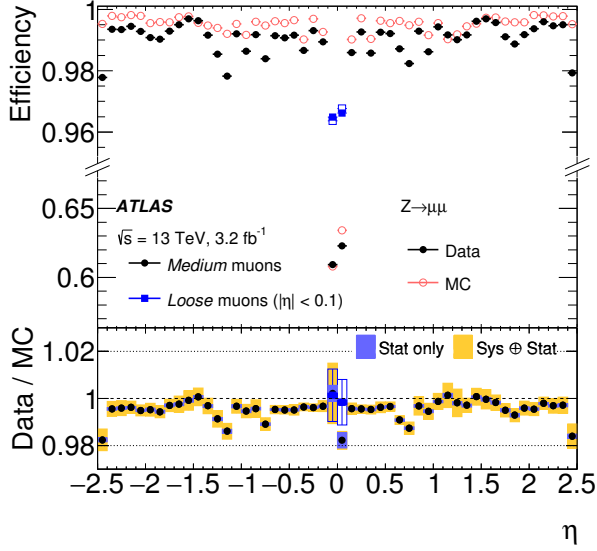


**Figure 3.4:** Muon reconstruction efficiency for loose and medium muons.<sup>30</sup> Loose and medium muons are identical except in the  $|\eta| < 0.1$  region where loose muons also accept calo-tagged and segment tagged muons to recover efficiency.

$$\frac{\sigma(p_T)}{p_T} = r_o/p_T \oplus r_i \oplus r_2 \cdot p_T \quad (3.8)$$

$r_o/p_T$  accounts for fluctuations in the energy loss in the calorimeter material.  $r_i$  describes multiple scattering, local disturbances in the magnetic field and displacement of hits.  $r_2 \cdot p_T$  describes the spacial resolution on the detector hits and any potential mis-alignment in the MS. Uncertainty with all 3 parameters  $r_o$ ,  $r_i$  and  $r_2$  are all extracted using a likelihood fit to  $J/\psi \rightarrow \mu\mu$  or  $Z \rightarrow \mu\mu$  events in data.

The affect of muon momenta calibration on the MC description of  $J/\psi \rightarrow \mu\mu$  and  $Z \rightarrow \mu\mu$  mass peaks can be seen in figure 3.5.

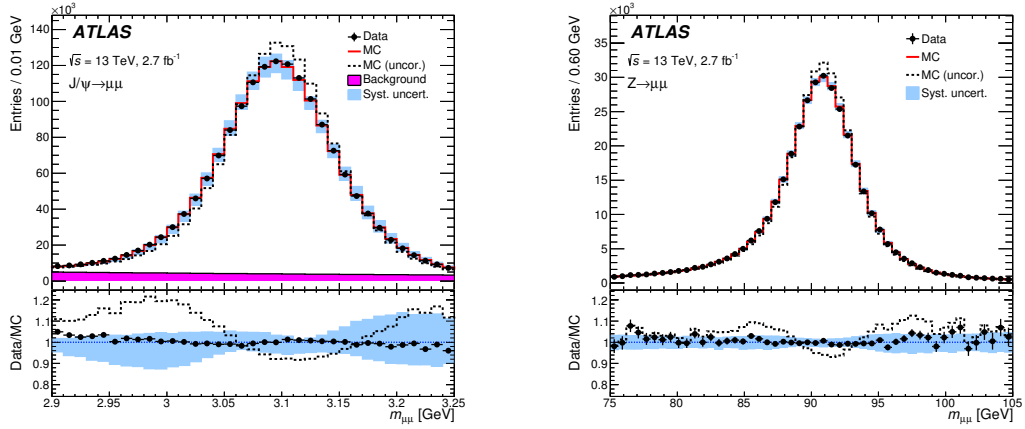


**Figure 3.5:** Dimuon invariant mass before and after muon momenta calibration in data and MC.<sup>30</sup>

### 3.6 MISSING TRANSVERSE MOMENTUM

Stable or metastable particles which only interact via the weak force and gravity cannot be directly detected at ATLAS. In the standard model, these particles correspond to neutrinos. In BSM models, there maybe many other weakly interacting particles such as WIMP, gravitons, and in the case of SUSY, stable neutral LSPs such as in this case neutralinos.

The presence of weakly interacting particles are inferred through conservation of transverse momentum. The total transverse momentum is zero in the initial colliding partons at the LHC. Therefore, any momentum imbalance in the transverse plane relative to the beam axis must be due to undetected particles in the final state.

### 3.6.1 $E_T^{\text{miss}}$ RECONSTRUCTION

We reconstruct the  $E_T^{\text{miss}}$  according to equation 3.9. The first term is a negative vector sum of hard fully calibrated objects and a term representing the soft objects in the interaction.

$$E_T^{\text{miss}} = -\left(\sum_{\text{hard objects}} E_T + \sum_{\text{soft}} E_T\right) \quad (3.9)$$

Fully calibrated hard objects are used to build the  $E_T^{\text{miss}}$  in this analysis. These objects include muons, electrons, photons and jets that satisfy their respective baseline selections. Hadronic taus are not independently reconstructed and calibrated. Hadronic taus will most likely be reconstructed as hadronic jets in the  $E_T^{\text{miss}}$  building for our analysis. Baseline object definition can be found in the physics object definitions in table ?? . An overlap removal algorithm have been applied to the baseline objects to remove any potential duplicate objects.

We use a track based method called Track Soft Term (TST)<sup>8</sup> to reconstruct the contribution from soft objects. TST build the  $E_T^{\text{miss}}$  that is not associated with any hard objects by summing the  $p_T$  of ID tracks.

TST has the advantage of being relatively robust against pileup interactions because TST only use ID tracks that are matched with the primary vertex. However TST cannot measure the contribution to  $E_T$  from neutral particles because neutral particles do not leave tracks in the ID. TST is the standard method of estimating  $E_T^{\text{miss}}$  at ATLAS in Run 2 due to the high pileup conditions.

Only tracks with  $p_T > 400$  MeV are accepted and a number of track quality requirements are

applied. The track quality requirement follows recommendations from the ATLAS tracking performance group and include a minimum of 7 silicon hits and requirement on the impact parameter  $d_0$ . Any tracks within a  $\Delta R$  of 0.05 of an electron or photon cluster, the ID tracks of muons, and any ID tracks matched to jets are removed to avoid double counting of hard objects. Further details on TST can be found in <sup>8</sup>.

$E_T^{\text{miss}}$  reconstructed in using this method is the standard  $E_T^{\text{miss}}$  used throughout all signal, control and validation regions in this analysis and is simply referred to as  $E_T^{\text{miss}}$ . For the rest of this section, we specify this method of reconstructing  $E_T^{\text{miss}}$  as the TST  $E_T^{\text{miss}}$  to distinguish it from an alternative method of reconstructed  $E_T^{\text{miss}}$  called track  $E_T^{\text{miss}}$  described in section 3.6.2.

### 3.6.2 TRACK $E_T^{\text{miss}}$ RECONSTRUCTION

Track  $E_T^{\text{miss}}$  forms a complementary method of reconstructing  $E_T^{\text{miss}}$ . Track  $E_T^{\text{miss}}$  is reconstructed using a negative vector sum of all accepted ID tracks. ID tracks must pass the same requirement on ID tracks described in section 3.6.1 for the TST but no attempt is made at removing tracks that are associated with hard objects. The one except to this is tracks associated with an electron. Because of the high number of interaction expected between an electron and the material in the ID, electron tracks are replaced with the electron calorimeter cluster measurement instead.

Track  $E_T^{\text{miss}}$  is very robust against pileup conditions ATLAS has very good vertex resolution but neglects the presence of neutral particles. Track  $E_T^{\text{miss}}$  is also limited by  $\eta$  coverage of the ID which only extends to an  $|\eta| < 2.5$ . We use track  $E_T^{\text{miss}}$  as a cross check on the object based  $E_T^{\text{miss}}$  reconstruction described in 3.6.1. Both object based and track based  $E_T^{\text{miss}}$  must agree loosely in direction for

our analysis.

### 3.6.3 $E_T^{\text{miss}}$ PERFORMANCE

$E_T^{\text{miss}}$  performance maybe measured using a number of processes include  $Z \rightarrow ll$ ,  $W \rightarrow b$  and ttbar.

$Z \rightarrow ll$  produced with additional jets is considered the gold standard. Very little intrinsic  $E_T^{\text{miss}}$  is produced in the  $Z \rightarrow ll$  plus jets process. This presents a good opportunity to study the affect of the  $E_T^{\text{miss}}$  soft term calculation since no hard invisible particles exist. All other terms inherently depends on the resolution of other reconstructed hard objects and therefore the only variable intrinsic to  $E_T^{\text{miss}}$  reconstruction is the soft term.  $W \rightarrow b$  is used to study a topology with an high- $p_T$  neutrino and therefore intrinsic  $E_T^{\text{miss}}$  and ttbar is used to study topologies with a large number of jets.

Results from  $Z \rightarrow ll$  performance study<sup>8</sup> will be summarized here. The  $W \rightarrow b E_T^{\text{miss}}$  and ttbar study will not be covered here but further detail can be found in<sup>8</sup>.

$Z \rightarrow \mu\mu$  events are selected by requiring exactly two same flavor, opposite signed muons with  $p_T > 25$  GeV. The dilepton invariant mass must be within 25 GeV of the  $Z$  mass.

Distribution of the  $E_T^{\text{miss}}$  resolution in  $Z \rightarrow \mu\mu$  events , defined as the root-mean-squared (RMS) of the  $E_T^{\text{miss}}$  distribution is shown in figure ???. The  $E_T^{\text{miss}}$  resolution degrades both with the total amount of  $E_T$  in the event and the number of reconstructed vertexes.

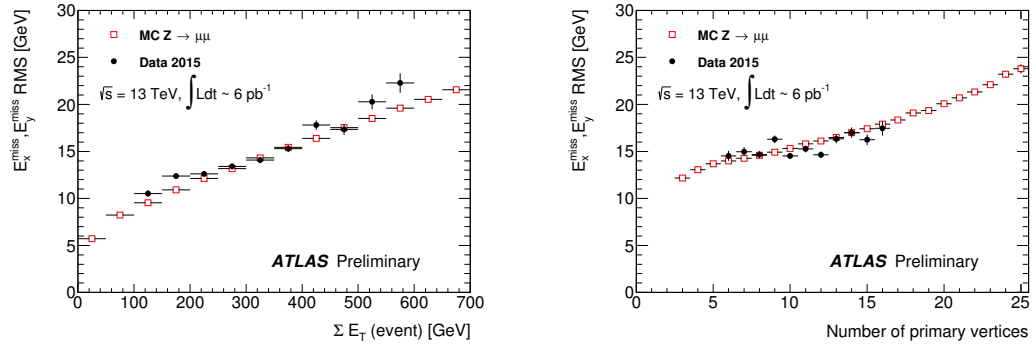


**Figure 3.6:** (a) Distribution of the TST  $E_T^{\text{miss}}$  resolution relative to the total  $E_t$  of reconstructed objects in  $Z \rightarrow \mu\mu$  events. (b) Distribution of the TST  $E_T^{\text{miss}}$  resolution relative to the number of reconstructed vertexes in  $Z \rightarrow \mu\mu$  events.  $E_T^{\text{miss}}$  resolution degrades as  $E_T$  and pileup increases.

# 4

## Trigger

Due to the large volume of data produced at the LHC, an efficient and robust triggering system is essential in deciding which events are potentially interesting and recorded for later study. The ATLAS trigger system is divided into two levels in Run 2. The first-level trigger (Level 1 or L1 trigger) is hardware based and uses a subset of detector information to quickly reduce the rate of accepted events from the initial 40 MHz to 100 kHz. Afterwards, the software based high-level trigger (HLT) fur-

ther reduces the rate of events to 1 kHz. Any events passing the HLT are recorded by ATLAS for further reconstructed and offline analysis.

Object reconstruct at the HLT is done only to the precision required by the executed trigger algorithms. These *online reconstruction* tend to be less precise than the offline reconstruction algorithms described in chapter 3, but the algorithms are significantly faster.

A schematic showing the different components are shown in figure 4.3. Only components relevant to the triggers used in this analysis will be discussed in detail. Further detail can be found in<sup>31</sup>.

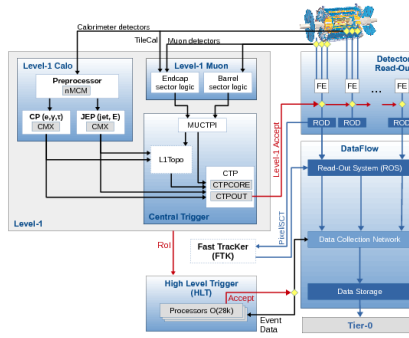


Figure 4.1: Schematic representation of the ATLAS trigger system and information flow.<sup>31</sup>

We use the lowest un-prescaled  $E_T^{\text{miss}}$  trigger in this analysis. This corresponds to the HLT\_XE70\_MHT\_LiXE50 trigger in 2015, HLT\_XE90\_MHT\_LiXE50 for 2016 data taking period A-D3, HLT\_XE100\_MHT\_LiXE50 for the period D4-F1 and HLT\_XE110\_MHT\_LiXE50 for period F2 and onward. The HLT trigger thresholds increase multiple times in 2015 and 2016 to accommodate the increasing instantaneous luminosity but all the triggers used are evaluated using the same algorithm. All HLT triggers that we

use are seeded by the L1\_XE50 trigger.

A summary of the L1 and HLT  $E_T^{\text{miss}}$  triggers used in this analysis is given in section 4.1 to ??

#### 4.1 LEVEL I $E_T^{\text{miss}}$ TRIGGER

The L1  $E_T^{\text{miss}}$  trigger is based on the vector sum of  $E_T$  in the calorimeter and is part of the L1Calo trigger system<sup>21</sup> shown in figure 4.3. The process starts with trigger towers in the electromagnetic and hadronic calorimeters. Trigger towers are more coarse than those used in offline reconstruction: Most are  $0.1 \times 0.1$  in  $\Delta\eta \times \Delta\phi$ . The trigger towers are calibrated at the electromagnetic energy scale (EM scale) which correctly reconstructs EM shower energy but underestimates hadronic showers.

These trigger towers are then built into *jet elements* composed of  $2 \times 2$  EM trigger towers and combined with the  $2 \times 2$  hadronic trigger towers directly behind the EM towers. The jet elements are then fed to the Jet/Energy-sum Processor (JEP). The JEP calculates the global sums of  $E_t$  and  $E_T^{\text{miss}}$  by summing the  $E_x$ ,  $E_y$ , and scalar  $E_t$  of all jet elements. If the total  $E_T^{\text{miss}} = |-\sqrt{E_x^2 + E_y^2}|$  is above a certain value the event passes the  $E_T^{\text{miss}}$  trigger and is passed to the HLT. For this analysis, the threshold is 50 GeV for the L1\_XE50  $E_T^{\text{miss}}$  trigger.

#### 4.2 HLT $E_T^{\text{miss}}$ TRIGGER

The reconstruction of  $E_T^{\text{miss}}$  for the HLT also begins with identifying topo-clusters in the calorimeters. Much like offline topo-clusters described in section 3.3.1. Seed cells with greater than  $4\sigma$  signal over noise thresholds are first identified and neighboring cells with greater than  $2\sigma$  thresholds are

added. Neighboring cells with greater than  $2\sigma$  are continually added until no neighboring cell pass the  $2\sigma$  threshold. At this point, one final round of neighboring cells are added regardless of energy thresholds.

Jet reconstruction and calibration are also similar to offline jet reconstruction described in section 3.3.1. Jets are reconstructed using the  $\text{anti}-k_t$  algorithm from topo-clusters. Jet calibration also follow the same basic offline procedure in section 3.3.2 and include pileup subtraction. However, HLT jet calibration and offline calibration procedures do differ in many ways including different pile-up corrections, track-based correction and certain in-situ corrections. Overall this leads to poorer jet resolutions at the HLT level. Some of these corrections were added in 2016 to further improve the agreement between online and offline jet reconstruction. Details can be found in <sup>20</sup>.

The  $E_T^{\text{miss}}$  is calculated directly by calculating the vector sum of the negative transverse momentum of all reconstructed jets. Only contributions from the calorimeter is taken into account in the  $E_T^{\text{miss}}$  calculation and muon tracks are not included. This method of calculating the  $E_T^{\text{miss}}$  from calibrated jets is referred to as missing  $H_T$  (MHT).

We apply 70, 90, 100, or 110 GeV thresholds to our HLT  $E_T^{\text{miss}}$  trigger depending on the data taking period. Trigger turn on curves can be seen in figure 4.2. Trigger thresholds increases over time because the instantaneous luminosity increases.

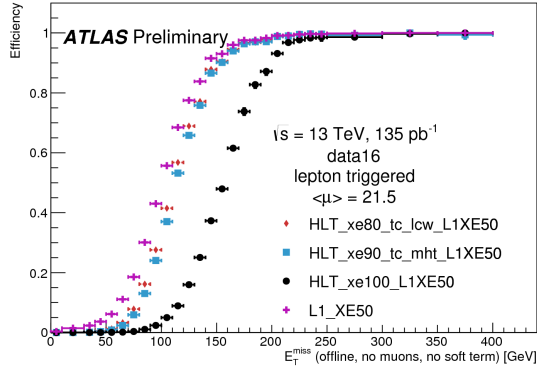


**Figure 4.2:** ATLAS trigger turn on curves for MHT  $E_T^{\text{miss}}$  triggers with several different thresholds.

### 4.3 IMPROVEMENTS TO THE $E_T^{\text{miss}}$ TRIGGER IN RUN 2

A significant improvement to pileup mitigation was made to the LiCalo trigger system for Run 2.<sup>31</sup>

The ATLAS Liquid Argon Calorimeter integrates its signal over a time window of 600 ns. This corresponds to 24 bunch crossing, if bunches are separated by 25 ns. Energy deposition from collisions occurring in neighboring bunches (referred to as out-of-time pileup) will be registered as signal. This results in a higher average amplitude in collisions at the beginning of a bunch train than those at the end of a bunch train.

This dependence of the average amplitude or *pedestal* on bunch-crossing location was corrected offline but not at the trigger level in Run 1. However in Run 2, a dynamic bunch-by-bunch pedestal correction was implemented at the trigger level. This lead to a significant reduction in L1  $E_T^{\text{miss}}$  trigger rate as shown in figure ??.

This improvement to the LAr energy calibration also improves the jet energy calibration at the

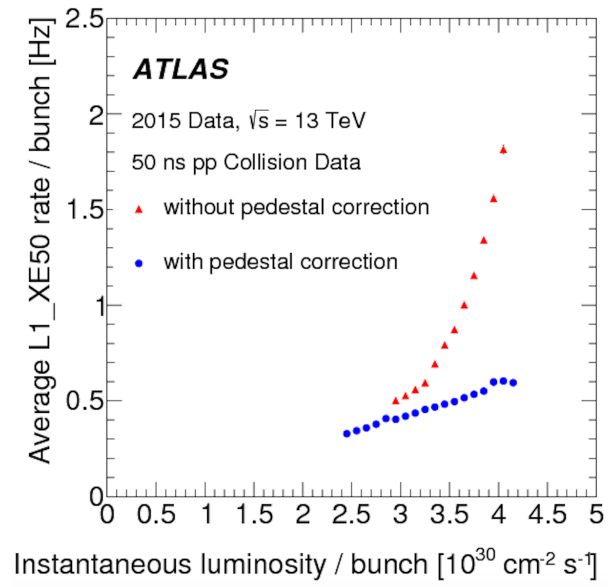


**Figure 4.3:** Improvement to the L1\_XE50 rate with new dynamic pedestal correction for out-of-time pileup.<sup>31</sup>

HLT. This not only improves HLT  $E_T^{\text{miss}}$  trigger performance but also improves the performance of other HLT calorimeter triggers such as those on total  $E_T$ .<sup>20</sup>

# 5

## Physics Object Definitions

We require a certain set of quality cuts for all reconstructed physics objects used in this analysis. In general, we have a looser set of cuts on *baseline* objects and a tighter set of cuts on *signal* objects. The object selection is inclusive meaning that the tighter signal objects must also pass the looser baseline object selection.

Baseline objects are used to reconstruct the  $E_T^{\text{miss}}$  and are also used to veto events. These appli-

cations benefit the most from having a higher reconstruction efficiency. The quality of lepton momenta resolution are less important in this case since we are not performing any measurements on the lepton except only tagging their presence. The same is true for the  $E_T^{\text{miss}}$  calculation where we want to perform the calculation on calibrated hard objects instead of relying on the soft term calculation.

In general, signal objects are used in the analysis in places where we need to ensure robust energy/momenta reconstruction or just the presence of well reconstructed objects.

For example signal electrons and muons are used in the 1 lepton control regions where the leptons are used to calculate things like the transverse mass of the  $W$  boson but baseline electrons and muons are used to veto events for the 0 lepton control region.

Signal jets are used in the 0 lepton signal and validation regions and 1 lepton control regions. Signal photons are used in the single photon control region used to estimate the ttV background.

Overlapping objects are resolved at the baseline level using the algorithm described in section 5.6. The  $E_T^{\text{miss}}$  is reconstructed using baseline objects that passed overlap removal according to the algorithm described in section 3.6.

All object definitions used follow the ATLAS performance group recommendations and SUSY group standards for MC<sub>15c</sub> samples ([SUSYTools-00-08-54](#) and [AnalysisBase-2.4.28](#)). Details on each object is given below.

## 5.1 ELECTRON DEFINITION

Baseline electron candidates are selected using the `VeryLooseLH` quality definition. The energy clusters associated with the electron are required to have an  $E_T = E_{cl}/\cosh \eta > 7 \text{ GeV}$  and be within an  $\eta$  range of  $|\eta_{cl}| < 2.47$ . Electrons in the transition region between EM barrel and endcap calorimeters ( $1.37 < |\eta| < 1.52$ ) also called the crack region are accepted as long as they satisfy the `VeryLooseLH` criteria.

We use the gradient loose criteria for electron isolations. The isolation parameter changes depending on the lepton  $p_T$  in gradient isolation, ensuring a balance between efficiency and fake rate at all lepton  $p_T$  values.

Table 5.1 summarizes the baseline electron definition criteria.

**Table 5.1:** Baseline Electron selection criteria. The overlap removal is described in more detail in section 5.6.

Cut	Value
Acceptance	$p_T > 7 \text{ GeV},  \eta_{clust}  < 2.47$
Quality	<code>VeryLooseLH</code>
Isolation	<code>Gradient Loose</code>
Overlap: $e$ rejected if	$0.2 < \Delta R(e, jet) < 0.4$

Signal electrons require the tight likelihood `TightLH` quality requirement. The minimum  $p_T$  is also increased to  $20 \text{ GeV}$ . Table ?? summarizes the signal electron definition.

**Table 5.2:** Signal Electron selection criteria. The overlap removal is described in more detail in section 5.6.

Cut	Value
Acceptance	$p_T > 20 \text{ GeV},  \eta_{\text{clust}}  < 2.47$
Quality	<b>TightLH</b>
Isolation	<b>Gradient Loose</b>
Overlap: $e$ rejected if	$0.2 < \Delta R(e, \text{jet}) < 0.4$

## 5.2 MUON DEFINITION

Baseline muon candidates must pass the **Loose** quality criteria. Baseline muons must also have a  $p_T > 6 \text{ GeV}$ , and be within  $|\eta| < 2.7$ . Baseline muon selections are summarized in table 5.3.

We use the gradient loose criteria for muon isolations. The isolation parameter changes depending on the lepton  $p_T$  in gradient isolation, ensuring a balance between efficiency and fake rate at all lepton  $p_T$  values.

**Table 5.3:** Selection criteria for baseline muons. The overlap removal is described in more detail in section 5.6.

Cut	Value
Acceptance	$p_T > 6 \text{ GeV},  \eta  < 2.7$
Quality	<b>Loose</b>
Isolation	<b>Gradient Loose</b>
Overlap: $\mu$ is rejected if	$\Delta R(\mu, \text{jet}) < 0.4$

Signal muon candidates must pass the **Medium** quality criteria. Signal muons must have a  $p_T > 20 \text{ GeV}$ , and be within  $|\eta| < 2.7$ . Signal muon selections are summarized in table 5.4.

**Table 5.4:** Selection criteria for signal muons.

Cut	Value
Acceptance	$p_T > 20 \text{ GeV},  \eta  < 2.7$
Quality	Medium
Isolation	Gradient Loose
Overlap: $\mu$ is rejected if	$\Delta R(\mu, \text{jet}) < 0.4$

### 5.3 JET DEFINITIONS

#### 5.3.1 CALORIMETER JETS

Jets are reconstructed from topological clusters using the  $\text{anti} - k_t$  jet algorithm<sup>7</sup> with a distance parameter of  $R = 0.4$ . The jets are calibrated use the EM+JES calibration scheme and global sequential calibration is enabled. Area-based pileup corrections are also applied. More details on jet reconstruction and calibration can be found in section 3.3.

Baseline jets must have  $p_T > 20 \text{ GeV}$  with no  $\eta$  requirement. Jets that pass this loose selection are considered when resolving overlapping objects and building  $E_T^{\text{miss}}$ . A jet vertex tagger value greater than 0.59 is also required to reject pileup jets not originating from the hard scattering interaction for jets with  $|\eta| < 2.4$  and  $p_T < 60 \text{ GeV}$ . The 0.59 JVT working point corresponds to a 92% efficiency for jets originating from the hard scattering interaction and a 2% fake rate from pileup, if the jet has  $|\eta| < 2.4$  and  $p_T < 60 \text{ GeV}$ .

After overlap removal, if any baseline jets are tagged as being `BadLoose` quality jets then the entire event is vetoed. This is because the presence of a bad quality jet probably also means poor  $E_T^{\text{miss}}$

reconstruction for the event. Details on jet quality can be found in section 3.3.4

Baseline jets are summarized in table 5.5.

**Table 5.5:** Selection criteria for baseline jets.

Cut	Value
Acceptance	$p_T > 20 \text{ GeV}$ , no $\eta$ requirement
JVT	$> 0.59$ if $p_T < 60 \text{ GeV}$ and $ \eta  < 2.4$ , no requirement if $p_T > 60 \text{ GeV}$ or $ \eta  > 2.4$
Quality	if any jet is <b>BadLoose</b> then veto whole event
Overlap	See section 5.6

Signal jets are required to have  $p_T > 20 \text{ GeV}$  and  $|\eta| < 2.8$  plus all selections applied to the baseline jets. Jet quality must satisfy the **Loose** criteria defined in section 3.3.4.

Signal jets are summarized in table 5.6.

**Table 5.6:** Selection criteria for signal jets.

Cut	Value
Acceptance	$p_T > 20 \text{ GeV}$ , $ \eta  < 2.8$
JVT	$> 0.59$ if $p_T < 60 \text{ GeV}$ and $ \eta  < 2.4$ , no requirement if $p_T > 60 \text{ GeV}$ or $ \eta  > 2.4$
Quality	<b>Loose</b>
Overlap	See section 5.6

### 5.3.2 $b$ -TAGGED JETS

A subset of jets are identified as originating from a  $b$ -hadron using the MV2c10  $b$ -tagging algorithm described in section 3.3.5.  $b$ -jet candidates must be within ID coverage with  $|\eta| < 2.5$ . Any jet with

$MV2c10 > 0.6459$  is a b-tagged jet. The selection chosen corresponds to approximately 77% b-tagging efficiency with a factor of 134 reject rate for light jets and a factor of 6 rejection of c-jets.

#### 5.4 PHOTON DEFINITION

Baseline photons are used only for  $E_T^{\text{miss}}$  calculation. Baseline photons must have  $p_T > 25 \text{ GeV}$  and  $|\eta| < 2.37$  and pass the `Tight` quality selection. Photon reconstruction and calibrated are summarized in section 3.4.

The photon definition is summarized in table 5.7

**Table 5.7:** Baseline photon selection criteria.

Cut	Value
Acceptance	$p_T > 25 \text{ GeV},  \eta  < 2.37$
Quality	<code>Tight</code>

Signal photons are used only in the  $t\bar{t}\gamma$  control region used to model the  $t\bar{t}V$  background. Signal photons must pass the requirements in Table 5.8. The high  $p_T > 130 \text{ GeV}$  requirement is to ensure that the event has near 100 percent trigger efficiency for the photon trigger `HLT_g120_loose`.

**Table 5.8:** Signal photon selection criteria.

Cut	Value
Acceptance	$p_T > 130 \text{ GeV},  \eta  < 2.37$
Quality	<code>Tight</code>
Isolation	<code>FixCutLoose</code>

## 5.5 $E_T^{\text{miss}}$ DEFINITIONS

### 5.5.1 CALORIMETER-BASED $E_T^{\text{miss}}$

The  $E_T^{\text{miss}}$  is calculated as the negative vector sum of the  $E_T$  of all fully calibrated baseline objects including baseline muons, electrons, photons and jets after overlap removal. An extra term is added to the  $E_T^{\text{miss}}$  to account for energy in the event that is too soft to be associated to any of the selected objects. This soft term is calculated using inner detector tracks that are matched to the primary vertex and is relatively robust against pileup interactions. Details on the  $E_T^{\text{miss}}$  reconstruction can be found in section 3.6.

### 5.5.2 TRACK-BASED $E_T^{\text{miss}}$

An complementary method of determining the  $E_T^{\text{miss}}$  using only tracking information is used to discriminate against events with fake  $E_T^{\text{miss}}$  resulting from mis-reconstructed calorimeter jets. The track based  $E_T^{\text{miss}}$  or  $E_T^{\text{miss,track}}$  is the negative vector sum of all ID track  $p_T$ .  $E_T^{\text{miss,track}}$  is very robust against pileup but does not include the contribution to  $E_T$  from neutral particles. None the less, a loose agreement in direction between  $E_T^{\text{miss,track}}$  and calorimeter-based  $E_T^{\text{miss}}$  was found to be an effective discriminate against multijet QCD background. Details on  $E_T^{\text{miss,track}}$  reconstruction can be found in section 3.6.2.

## 5.6 RESOLVING OVERLAPPING OBJECTS

Overlap removal between accepted physics objects must be performed in order to avoid double counting of objects such as the same calorimeter energy being assigned to a jet and an electron. The distance metric  $\Delta R = \sqrt{\Delta\phi^2 + \Delta\eta^2}$  is used to define overlapping objects. Objects too close in  $\Delta R$  are considered overlapping and all except one object will be removed. The following guidelines are used for removing overlapping objects.

- If an electron and jet are located with  $\Delta R < 0.2$  then the object is considered an electron and the jet is removed; unless the jet is b-tagged using the 85% working point rather than the 77% working point used in the signal regions in which case the jet is kept and the electron is removed.
- If a muon and jet are located with  $\Delta R < 0.4$ , then the object is considered a jet and the muon is removed; unless the jet has less than three tracks (with  $p_T > 500$  MeV), in which case the jet is removed while the muon is kept.
- If an electron and jet are located with  $0.2 \leq \Delta R < 0.4$ , then the object is considered a jet and the electron is removed.

Overlap removal is performed on baseline objects before the  $E_T^{\text{miss}}$  is reconstructed.

# 6

## Monte Carlo Simulation of Physics

### Processes at ATLAS

Simulated event samples are used to model the signal and background processes in this analysis. A full list of the samples that are used is given in Appendix ??.

Process	Generator	fragm./hadron.	PDF set	UE Tune	Cross section ord.
SUSY Signal	MADGRAPH5_AMC@NLO	PYTHIA 8	NNPDF2.3	A14	LO
$t\bar{t}$	POWHEG-BOX v2	PYTHIA 6	CT10	PERUGIA 2012	NLO
Single top	POWHEG-BOX v2	PYTHIA 6	CT10	PERUGIA 2012	NLO
$W/Z+jets$	SHERPA 2.2.1	SHERPA	NNPDF3.0NNLO	Default	NLO
Diboson	SHERPA 2.2	SHERPA	CT10	Default	LO
$t\bar{t} + V$	MADGRAPH5_AMC@NLO	PYTHIA 8	NNPDF3.0NNLO	A14	NLO

Table 6.1: Overview of the nominal simulated samples.

## 6.1 SIGNAL MONTE CARLO GENERATION

For the stop signal, the matrix element (ME) of the hard scattering interaction are calculated using MADGRAPH5\_AMC@NLO. Up to two additional QCD partons are included in the ME calculation, making the total hard scattering process  $pp \rightarrow t\bar{t} + j + j$ . The ME calculation is performed to leading order accuracy (LO).

The stop decays are treated differently depending on the mass splitting between the stop and its decay products. The resulting decays are be seen in the Feynman diagrams shown in figure 6.1.

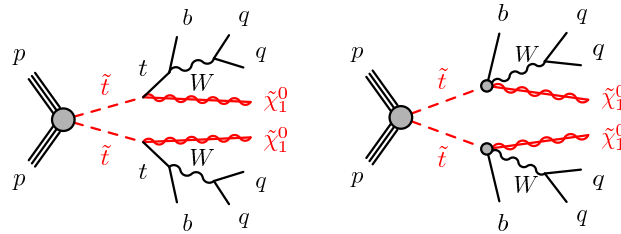


Figure 6.1: The decay topologies of the signal models considered depending on the mass splitting between  $\tilde{t}$  and  $\tilde{\chi}_1^0$ , a real top maybe produced in the 2 body decay  $\tilde{t} \rightarrow t\tilde{\chi}_1^0$ , or virtually through a three body decay  $\tilde{t} \rightarrow bW\tilde{\chi}_1^0$

If  $m_{\tilde{t}} - m_{\tilde{\chi}_1^0} \geq m_T$ , then the top can be produced on shell. PYTHIA 8 perform 2 body  $\tilde{t} \rightarrow T\tilde{\chi}_1^0$  decay and subsequent decays of the top.  $m_T$  is set to 172.5 GeV. This process has the advantage

in that it is much computationally faster when compared to decaying the stops as part of the ME calculation. However it has the disadvantage of effectively assuming that the stop width is zero. The zero stop width assumption was found to differ from the true stop width case by less than 5 percent in the distributions of all relevant kinematic variables. The nominal stop width in the simplified model is  $1/10$  the width of the top and so the stop width represent only a small smearing on the distribution of  $m_T$  and  $E_T^{\text{miss}}$  compared of the one produced by the top width.

If  $m_{\tilde{t}} - m_{\tilde{\chi}_1^0} < m_T$ , then the top must be produced off shell. PYTHIA 8 cannot perform the 3 body  $\tilde{t} \rightarrow bW\tilde{\chi}_1^0$  or 4 body  $\tilde{t} \rightarrow bff\tilde{\chi}_1^0$  decays where the "f" stands for the fermions that result from a  $W$  decay. Instead we use MadSpin to perform the  $\tilde{t} \rightarrow bff\tilde{\chi}_1^0$  decay. MadSpin can perform 3 body and 4 body decays with off shell virtual particles as long as the decay are ultimately a series of 2 body decays. MadSpin performs the decays in a timely manner compared to calculated the decay within the ME. In this case, MadSpin cannot calculate the spin correlations between the two stops but this is not a problem because the stops are scalar particles so no spin correlations exist between the two.

In addition to the ME calculation and stop decays, the parton shower (PS) and hadronization of jets are simulated with PYTHIA 8 with the EvtGen vi.2.0 program as afterburner. The matching between the matrix element and parton shower jets is preformed with the CKKW-L prescription. The matching scale is set to  $1/4$  the mass of the stop..

The internal structure of the proton is modeled with the NNPDF3.0NNLO parton distribution function (PDF) set with A14 set as the underlying event tuned parameters (UE tune).<sup>23</sup> The A14 tune optimizes over 10 parameters that vary the amount of ISR, FSR and multiple parton interactions. The variations are reduced to a 5 variable subset that is found to cover experimental observ-

ables.<sup>4</sup> Variable 1 mainly cover variation in the modeling of the underlying events. Variable 2 mainly cover variation in jet structure and variable 3a, 3b and 3c cover different variations of ISR and FSR production. All 5 variations are used to quantify the theoretical uncertainties associated with parton shower and multiple parton interactions and are added in quadrature.

Signal cross sections are calculated to next-to-leading order in the strong coupling constant with the resummation of soft gluon emission added to next-to-leading-logarithmic accuracy (NLO+NLL).<sup>25</sup> An envelope of cross section predictions is produced using different PDF sets and factorization and renormalization scales. The nominal cross section and the uncertainty are then taken from the median and 1 sigma fluctuations around the median within the envelope.

A 2D grid of signal samples is generated to cover the stop and neutralino mass phase space that we maybe sensitive to. Stop masses between 200 and 700 GeV are generated separated in  $m_{stop}$  by 50 GeV. For each Stop mass, five different  $\Delta m = m_{\tilde{t}} - m_{\tilde{\chi}_1^0}$  are simulated:  $\Delta m = m_{\tilde{t}} - 82.5$  GeV,  $m_{\tilde{t}} - 52.5$  GeV,  $m_{\tilde{t}} - 22.5$  GeV,  $m_{\tilde{t}} - 7.5$  GeV,  $m_{\tilde{t}} + 0.5$  GeV,  $m_{\tilde{t}} + 15.5$  GeV,  $m_{\tilde{t}} + 27.5$  GeV. An extra row of  $m_{\tilde{t}} = 225$  GeV samples is also produced to quantify the bound of sensitivity at low stop masses.

## 6.2 SM BACKGROUND MONTE CARLO GENERATION

### 6.2.1 STANDARD MODEL $t\bar{t}$ MONTE CARLO GENERATION

The nominal ttbar samples are generated using Powheg-Boxv.2. The matrix element calculation is computed to NLO accuracy and includes the  $pp \rightarrow t\bar{t} + j$  process where the  $j$  is an one additional

emitted parton. The top quark mass is set to 172.5 GeV and the proton substructure is modeled by the NLO CT10 PDF set<sup>41</sup> for the hard scattering process. The hard scattering renormalization and factorization scales are set to the generator default of  $\sqrt{(m_T)^2 + (p_{T\top})^2}$ .

PYTHIA6 version 6.427 simulates the parton shower, hadronization and underlying event. We use the Perugia 2012 tune<sup>42</sup> and the corresponding leading order CTEQ6L1 PDF set<sup>43</sup> in PYTHIA6. The resummation damping factor or  $b_{damp}$  which is one of the parameters used by PowHEG to control the ME and PS matching and the amount of high- $p_T$  ISR/FSR, is set to  $m_T$ .

ttbar cross-sections are calculated to NNLO accuracy in the strong coupling constant with the resummation of soft gluon emissions added to NNLL accuracy using the Top++v2.0 program.<sup>34</sup> Again an envelope of cross-sections is produced for different PDF sets including MSTW2008NNLO, CT10 NNLO and NNPDF2.3 NNLO. Variations in the renormalization and factorization scales, strong coupling constant, and top quark mass are also included in the envelope. The median of envelope is taken as the nominal ttbar cross-section and the 1 sigma variation in the envelope is taken as the ttbar cross-section uncertainty.

In addition to the total cross-section uncertainty, a number of ttbar samples are produced to study the variation in the shapes of ttbar kinematic distributions.

A radHi and radLo sample are produced to study the variation in the total amount of ISR/FST  $p_T$ . These samples are also produced with PowHEG+PYTHIA6 but have different renormalization and factorization scales ( $x_{0.5}$  to radHi and  $x_2$  to radLo). The radHi sample also has the  $b_{damp}$  parameter that help control the matching between PS and ME increased from the nominal  $m_{top}$  to  $x_2 m_{top}$ .

We study the variation of the parton shower simulation using a Powheg+Herwig++ ttbar sample. The hard scattering ME calculation has not changed from the nominal. The PDF used for the ME calculation is still NLO CT10 and the calculation is still performed with Powheg-Boxv.2 with the  $b_{damp} = m_T$ . However the PS, fragmentation and hadronization is now performed with Herwig++ with the CTEQ6L1 PDF set<sup>46</sup> with the UE-EE-5 parameter tune.

Variation in the hard scattering ME calculation are studied by comparing the nominal to a sample generated with SHERPA<sup>3</sup>. The same CT10 PDF set is used for sherpa and the nominal sample.

Non overlapping samples that are filtered according to  $E_T^{\text{miss}}$  are generated to increase statistics at high  $E_T^{\text{miss}}$  where our analysis resides. These samples are then merged to form a continuous distribution in  $E_T^{\text{miss}}$ .

### 6.2.2 STANDARD MODEL SINGLE TOP MONTE CARLO GENERATION

Like the nominal ttbar sample, the nominal single top samples are also simulated with Powheg-Boxv.2 and interfaced to PYTHIA6 for hadronization and parton showering, with CT10 PDF set and using the Perugia 2012 set<sup>47</sup> of tuned parameters.

Unlike the ttbar samples, single top samples are produced separately according to production channels. Three production channels exist including the s-channel, t-channel and the Wt channel. The largest contribution to our analysis comes from the Wt channel.

The NLO calculation of the  $p\bar{p} \rightarrow Wt$  includes contributions from  $p\bar{p} \rightarrow t\bar{t} \rightarrow t + b + W$ . However  $p\bar{p} \rightarrow t\bar{t} \rightarrow t + b + W$  is already included in our simulation of ttbar and including it here would be double counting. We can subtract out the ttbar contribution at either the level of amplitude (DR

scheme) or at the level of matrix elements (DS scheme). Subtracting at the matrix element level also remove any potential interference between the single top  $pp \rightarrow Wt$  and ttbar  $pp \rightarrow t\bar{t} \rightarrow t + b + W$  processes. Subtracting at the amplitude level does not remove those interferences. Both schemes violates formal gauge invariance and there isn't a consensus on the correct procedure. We generate two sets of Wt channel single top samples with the two schemes. The nominal single top sample is generated with the DR scheme and another sample is generated with the DS scheme. We to compare the difference between the two samples to quantify the uncertainty due to the single top and ttbar interference terms.

RadHi and radLo samples are also produced for all channels to study the variation in single top ISR and FSR emissions. These samples are also produced with PowHEG+PYTHIA6 but have different renormalization and factorization scales ( $x_0.5$  to radHi and  $x_2$  to radLo). The radHi sample also has the  $b_{damp}$  parameter that help control the matching between PS and ME increased from the nominal  $m_{top}$  to  $x_2 m_{top}$ .

We study the variation of the parton shower simulation using PowHEG+HERWIGG++ single top samples. The hard scattering ME calculation has not changed from the nominal. The PDF used for the ME calculation is still NLO CT10 and the calculation is still performed with PowHEG-Boxv.2 with the  $b_{damp} = m_T$ . However the PS, fragmentation and hadronization is now performed with HERWIGG++ with the CTEQ6L1 PDF set<sup>46</sup> with the UE-EE-5 parameter tune.

### 6.2.3 STANDARD MODEL $W + \text{jets}$ AND $Z + \text{jets}$ MONTE CARLO GENERATION

$W + \text{jets}$  and  $Z + \text{jets}$  are generated with the SHERPAv2.2.1 program. The matrix element are calculated for the vector boson (V) plus 0, 1, and/or 2 additional partons at NLO accuracy and 3, and/or 4 additional partons at LO accuracy.

The ME calculation is merged with SHERPA parton show according to the MEPS@NLO prescription. The proton substructure is modeled with the NNPDF3.0 NNLO PDF set and the PS tuning defined by SHERPA.

Systematic variations include a 7 point variation of the renormalization and factorization scales. The variations are used to quantify the theoretical uncertainty on our modeling of the  $W + \text{jets}$  and  $Z + \text{jets}$ .

The  $W + \text{jets}$  and  $Z + \text{jets}$  samples are generated in multiple non-overlapping slices of vector boson pt and b-jets and c-jets presence. The samples are then merged later to form a continuous distribution covering all phase space. This allows us to generate higher MC statistics in the region of phase space that is relevant to our analysis, the high- $p_T$  region with the presence of b and/or c-jets.

### 6.2.4 STANDARD MODEL $t\bar{t}+V$ MONTE CARLO GENERATION

$t\bar{t}+V$  where V is a  $W$  or  $Z$  boson samples are generated using MADGRAPH5\_AMC@NLO with the NNPDF3.0NLO PDF set. The matrix element calculation is performed to NLO accuracy. The parton shower, fragmentation, and hadronization is simulated using PYTHIA 8 with the underlying event tune A14. Variations in the hard scattering ME calculation are studied by generating another

sample using SHERPA and comparing its results to the nominal sample. Variation in renormalization and factorization scales are also produced.

### 6.2.5 STANDARD MODEL $t\bar{t} + \gamma$ MONTE CARLO GENERATION

$t\bar{t} + \gamma$  samples are generated using `MADGRAPH5_AMC@NLO` with the NNPDF3.0 NLO PDF set. The matrix element calculation is performed to NLO accuracy. The parton shower, fragmentation, and hadronization is simulated using PYTHIA 8 with the underlying event tune A14. The sample only simulates events with a filter for high photon  $p_T$ . This sample is then merged with the nominal ttbar sample to form the  $t\bar{t} + \gamma$  sample. The events with high  $p_T$  photons in the nominal ttbar samples are removed by a filter to avoid double counting.

### 6.2.6 STANDARD MODEL DIBOSON MONTE CARLO GENERATION

dibosons samples are generated with SHERPA v2.2 using CT10 PDF set.

## 6.3 DETECTOR SIMULATION

Two types of detector simulations were used. GEANT4 is used to perform the detector simulation for all background samples including ttbar,  $W + \text{jets}$ ,  $Z + \text{jets}$ , single top,  $t\bar{t} + V$ ,  $t\bar{t} + \gamma$ , and dibosons. For signal MC, a fast simulation framework is used in the interest of computing time. In fast simulation the majority of the detector are still simulated with GEANT4 with the exception of jets in the electromagnetic and hadronic calorimeter. Instead of simulating individual particle showers in the calorimeters, a predetermined parameterized description of the showers are used

instead. The fast simulation framework was validated against full GEANT4 simulation for several selected signal samples and found to agree in observed kinematics.

Groups within ATLAS that measure the detector and reconstruction performance may recommend reweighing of different MC depending on better or worse than expected performance of different reconstruction algorithms. Corrections are applied through reweighing to correct for known differences between data and simulation for the lepton trigger and reconstruction efficiencies, momentum scale, energy resolution, isolation, and for the efficiency of identifying jets originating from the fragmentation of  $b$ -quarks, together with the probability for mis-tagging light-flavor and charm quarks as recommended by ATLAS performance groups.

#### 6.4 PILE-UP SIMULATION

Because the LHC is operating at such high instantaneous luminosities, there are about on average 23 proton-proton interactions per bunch crossing. Most of these interactions have low amounts of momentum transfer between the protons and are called minimum-bias interactions. These interactions are also called pile-up interactions. In addition to the hard scattering interaction of interest, all MC samples are produced with a varying number of simulated minimum-bias interactions. The distribution of the number of additional overlaid minimum bias interactions is reweighed so that the distribution of the number of reconstructed vertexes matches between data and MC.

# 7

## General Analysis Strategy

### 7.1 GENERAL R-PARITY CONSERVING SUSY SEARCH STRATEGY

In R-parity conserving SUSY searches, the sought-after super-symmetric particles are produced in pairs. Each particle decays via a chain that ends in a stable, lightest super-symmetric particle (LSP). If the LSP is weakly interacting, it can not be directly detectable by the ATLAS detector and must be inferred from transverse momentum conservation as  $E_T^{\text{miss}}$ . The rest of the products from the decay

chain will be a series of SM particles.

All searches must distinguish between signal SUSY processes and background SM processes that mimic the signal detector signature. Traditional search methods often place a special emphasis on identifying the LSP as this is the one decay product that is unique to SUSY events. Practically this generally means searching for events with large amount of  $E_T^{\text{miss}}$ .

In regions with a large mass splitting between sparticle and LSP, the decay of the original sparticle generates large amounts of momentum for the LSP. Traditional searches therefore target the large amount of  $E_T^{\text{miss}}$  generated by the LSP as a method to separate signal from background.

Searches isolate signal by using this and other kinematic differences. Selections are made on sensitive variables forming a signal region (SR). The expected background rates in SR are predicted using a combination of MC and data driven techniques. One common technique involve making kinematically similar control regions (CR) and validation regions (VR). The CRs and VRs are designed to mimic the background kinematics in SR but are orthogonal to SR and are low expected signal rate. We directly measure the rate of background in kinematically similar CRs and use simulation to extrapolate between CR and SR. VRs form an independent cross check on these background predictions.

The data in SR is originally blinded to avoid any bias for or against discovery. We unblind the SR only after we decide the background prediction in SR is well understood based on observations in CRs and VRs.

## 7.2 GENERAL STRATEGIES IN COMPRESSED REGIONS

When the mass splitting between the original sparticle and its decay products becomes small, the sparticle has little energy to generate momenta in its decay products. The result is LSPs with low momenta. The traditional strategy of searching for events with large amount of  $E_T^{\text{miss}}$  therefore fails in this region of parameter space. This problem is ubiquitous to all regions with small mass splittings. We refer to all such regions as compressed regions.

In our analysis, the super-partner of the top, the stop is expected to decay into a neutralino and top. When the stop mass is close to that of the top mass plus the neutralino mass, both the top and neutralino gain very little momenta from the decay. The invisible neutralinos in turn generate very little missing transverse energy. This leaves only the visible tops which are mimicked by SM ttbar.

Traditional search methods depend on variables that are highly correlated with the total magnitude of  $E_T^{\text{miss}}$  such as  $m_{T2}$  and  $m_{\text{eff}}$ . Therefore traditional methods fail to separate stops from SM ttbar which has 50 to 300 times the production cross-section of stops in the region of interest. A High-Luminosity LHC study projects a  $2\sigma$  exclusion limit up to a stop mass of 500 GeV with 300  $\text{fb}^{-1}$  of data in this region.<sup>19</sup> The projected p-value as a function of stop mass for 300 and 3000  $\text{fb}^{-1}$  of data is given in figure 7.1

However, the soft decay products can gain additional momenta if the entire system is boosted by strong initial state radiation (ISR). The goal of the traditional searches have always been to identify the presence of the LSPs and use their presence to distinguish between signal and background. Instead of targeting events with large amount of  $E_T^{\text{miss}}$ , we use the correlations between the LSP

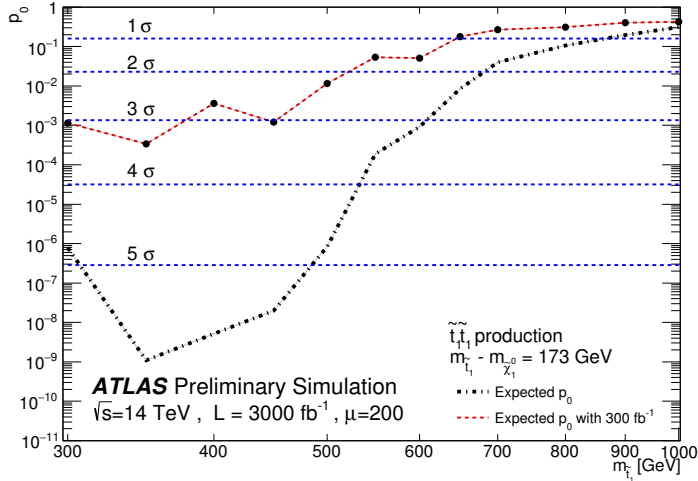


**Figure 7.1:** Projected HL-LHC sensitivity to the  $\Delta m = m_t$  region with 300 and  $3000 \text{ fb}^{-1}$  of data. Sensitivity is quantified in terms of the p-value  $p_0$ . 2 sigma exclusion is reached for stop masses below 500 GeV with  $300 \text{ fb}^{-1}$ . Figure taken from?

momenta and any ISR jets to identify LSPs in compressed regions.<sup>42,22</sup> Because LSPs gain little momentum from stop decays, the correlation between ISR and LSPs in compressed regions tend to be extremely strong. By targeting the correlations between ISR and  $E_T^{\text{miss}}$  instead of the total magnitude of  $E_T^{\text{miss}}$ , we effectively turn a weakness of the compressed region into a strength.

The relationship between the decay products and ISR also has an additional benefit of being model independent. This correlation is dictated solely by relativistic kinematics rather than the underlying QFT of any particular model. The direction and magnitude of the momenta of the decay products are determined mostly by two things, how heavy the decay products are and how hard they are kicked by the ISR. For the  $p\bar{p} \rightarrow \tilde{t}\tilde{t} \rightarrow t\tilde{\chi}_1^0 \bar{t}\tilde{\chi}_1^0$  process, the relationship is given by equation 7.2. This ratio between the invisible decay products and the total ISR  $p_T$  is called  $R_{\text{ISR}}$ .

$$E_T^{\text{miss}} \equiv p_{\tilde{t}\tilde{t}}^{\text{lab}} \beta_{\tilde{t}\tilde{t}}^{\text{lab}} E_{\tilde{t}\tilde{t}}^{\text{miss}} \sim \frac{p_T^{\text{ISR}}}{m_{\tilde{t}\tilde{t}}} 2\gamma_{\tilde{t}\tilde{t}}^{\tilde{t}\tilde{t}} m_{\tilde{t}\tilde{t}} \sim p_T^{\text{ISR}} \frac{2\gamma_{\tilde{t}\tilde{t}}^{\tilde{t}\tilde{t}} m_{\tilde{t}\tilde{t}}}{2\gamma_{\tilde{t}\tilde{t}}^{\tilde{t}\tilde{t}} m_{\tilde{t}\tilde{t}}} \sim p_T^{\text{ISR}} \frac{m_{\tilde{t}\tilde{t}}}{m_{\tilde{t}\tilde{t}}} \implies (7.1)$$

$$R_{\text{ISR}} \equiv \frac{E_T^{\text{miss}}}{p_T^{\text{ISR}}} \sim \frac{m_{\tilde{t}\tilde{t}}}{m_{\tilde{t}\tilde{t}}}, \quad (7.2)$$

The ratio between  $E_T^{\text{miss}}$  and ISR  $p_T$  is proportional to the ratio between the mass of a single LSP and original sparticle. Its interesting to note that the back to back boost between the two original stops does not affect the correlation between the observable  $E_T^{\text{miss}}$  and ISR  $p_T$ . Although the LSP's can individually gain momenta from the back to back boost of the sparticles against one another, the back to back momenta will exactly cancel resulting in zero measurable  $E_T^{\text{miss}}$ .

The di-LSP system only gains  $p_T$  by inheriting it from the boost by the ISR system on the two sparticles. The fraction of the momenta that is inherited by the di-LSP system is exactly  $\frac{m_{LSP}}{m_{\text{sparticle}}}$  if the sparticle decay gives no additional momentum to the LSP.

Figure ?? shows the correlation between the  $R_{\text{ISR}}$  ratio in  $pp \rightarrow \tilde{t}\bar{t} \rightarrow t\tilde{\chi}_1^0 \bar{t}\tilde{\chi}_1^0$  simulation for two different stop masses (350 and 550 GeV) as predicted by equation 7.2. The  $\Delta m$  between stop and neutralino is 173 GeV or 550 MeV from the top mass in both cases. Both stop samples sharply peak at exactly  $m_{\tilde{t}\tilde{t}}/m_{\tilde{t}\tilde{t}}$  with a gaussian width of approximately 4 percent. No detector resolution effects were included in the simulation and only the all hadronic decay channel was considered.

The separation power of ISR and  $E_T^{\text{miss}}$  correlations are made even stronger considering the correlation is in 2 dimensions, in magnitude and direction. ISR and  $E_T^{\text{miss}}$  are necessarily back to back in signal. In comparison, the neutrino gains significant momentum directly from the top decay in

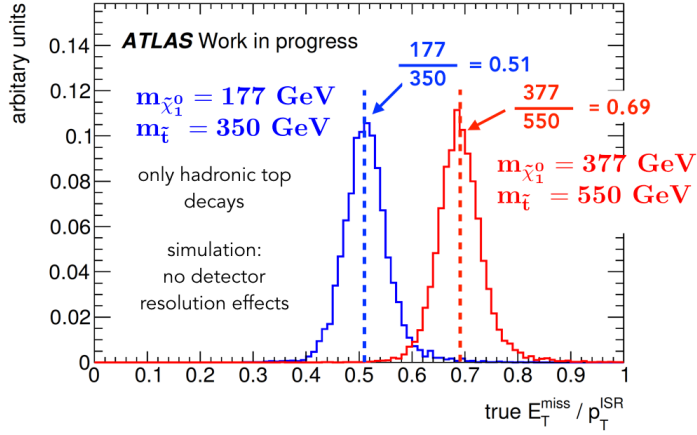


**Figure 7.2:** Correlation between the  $R_{\text{ISR}}$  ratio in simulation for two different stop masses. Both stop samples peak sharply at  $m_{\tilde{\chi}_1^0}/m_{\tilde{t}}$  with only a gaussian width of 4 percent. Deviation from the preferred ratio is limited by the top width, as the top must be pulled off-shell to generate phase space. No detector resolution effects were included and only the all hadronic decay channel was considered.

ttbar background and their correlation with ISR is not as absolute.

By constructing variables that capitalize on this correlation we are able to separate signal from SM backgrounds. At the same time, the increase in center-of-mass energy from 8 to 13 TeV can mean up to an order of magnitude increase in the production cross-section of signal plus strong ISR. The 13 TeV dataset presents a golden opportunity to search for many experimentally difficult physics processes that need a boost from strong ISR in order to be detected.

# 8

## Recursive Jigsaw Reconstruction

### 8.1 INTRODUCTION TO RECURSIVE JIGSAW ALGORITHM ON EVENTS WITH $E_T^{\text{miss}}$

Every search involving missing energy has to contend with the fact that information about the invisible system is lost. The question of how to best fill the missing degree of freedom is a problem ubiquitous to all analysis that have  $E_T^{\text{miss}}$  especially when there exists multiple invisible particles in the event. The recursive jigsaw method aims to compartmentalize the lost information and gain the

most from what information that is available.

Traditional edge variables such as  $\mathcal{M}_{T_2}$ , shown in equation 8.1, extremize over all possible kinematic configurations of the two invisible particles  $p_1$  and  $p_2$ . These variables can form an edge corresponding to some kinematic limit.  $\mathcal{M}_{T_2}$  effectively extremizes over all possible configurations allowed by the missing degrees of freedom. However, optimizing over too large a phase space can unintentionally destroy useful information.

$$\mathcal{M}_{T_2}^2 \equiv \min_{\not{p}_1 + \not{p}_2 = \not{E}_T^{miss}} \left[ \max \{ m_T^2(p_{Tl-}, \not{p}_1), m_T^2(p_{Tl+}, \not{p}_2) \} \right] \quad (8.1)$$

The recursive jigsaw reconstruction (RJR) method also uses maximizations and minimizations to pin down the missing degrees of freedom.<sup>39,40</sup> However, these extremizations are restricted to be in a specific location of the decay tree.

For example, consider a simple particle decay chain where  $a \rightarrow b c$  and then  $c \rightarrow 1 2$ . Recursive jigsaw would treat the situation differently if particle  $1$  was invisible compared to if particle  $b$  was invisible. To zeroth order, losing information about particle  $1$  affects only half the information on particle  $c$  which contains only half the information of particle  $a$ , but losing information on particle  $b$  directly affects half the information on particle  $a$ . Unlike traditional methods which extremizes over all possible configurations of the invisible particle. RJR compartmentalizes the lost information and extracts the maximum amount of information from events with missing energy.

RJR separates the event according to a predefined "decay tree." The decay tree can be as detailed as needed be, either attempting to resolve every branch in the decay tree down to the level of the fi-

nal state objects or forming aggregate states that have useful kinematics. Each node in the decay tree represents a particular intermediate state or final state. RJR will classify all accepted objects into the different nodes by extremizing certain metrics such as the state's mass and the state's energy. Specifics on the metrics used for each node are detailed in section 8.2. The extremizations set the unknown degree of freedoms in their respective center of mass frames. The result is then propagated back up the tree to the lab frame, creating a complete picture of the event with all ambiguities resolved.

For the compressed region, the most basic tree involves separating the event into sparticle and ISR systems and then further separating the sparticle system into visible and invisible parts. The decay tree is represented in figure. 8.1. Further detail can be added to the sparticle system such as resolving the stop decays. For this analysis, we found that attempting to reconstruct individual tops did not result in higher analysis sensitivity. The high multiplicity of hadronic jets makes reconstructing low pt tops very difficult in signal and gives little separation power because the dominant background is SM ttbar which also has real tops. Therefore, we avoid further resolving the sparticle node to the level of individual tops.

## 8.2 RECURSIVE JIGSAW METHOD OF IDENTIFYING INITIAL STATE RADIATION

In order to separate the event into an initial state radiation (ISR) system and a sparticle system, we first boost to the transverse center of mass frame of all accepted objects. The transverse center of mass frame has the useful property that when the entire event is divided into two systems, these two systems must have equal and opposite transverse momenta. Its also important to note that the lab

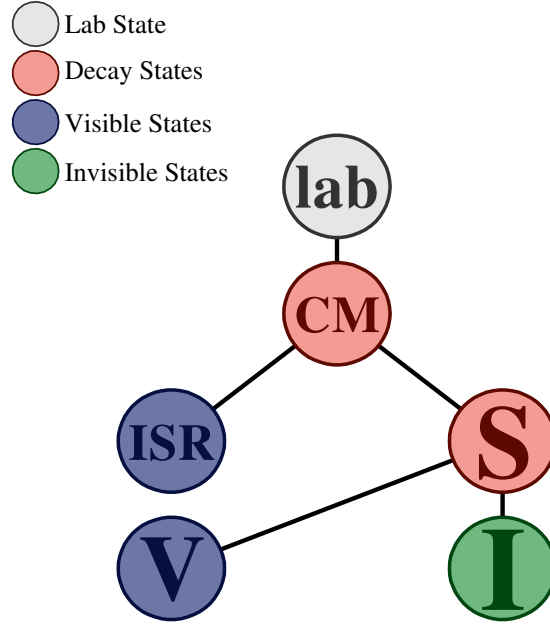


**Figure 8.1:** Decay Tree corresponding to ISR-assisted  $E_T^{\text{miss}}$  signal analysis strategy.

frame and the transverse center of mass frame only significantly differ in cases when an energetic object is not accepted. In other words, the two frames differ significantly only when the  $E_T^{\text{miss}}$  has a high probability of being miss reconstructed.

Once in the transverse center of mass frame, we find the thrust axis  $\vec{n}$  as defined in 8.2.

$$\vec{n} \equiv \max_{\text{jets, } E_T^{\text{miss}}} \vec{n} \sum_i |p_T^i \cdot \vec{n}| \quad (8.2)$$

The thrust axis  $\vec{n}$  represents the axis that maximizes the amount of back to back transverse momenta along it. If strong ISR is present, then the back to back recoil between ISR and stops should represent the single largest back to back kick in the event. Therefore, the thrust axis should approximate the direction of the back to back recoil between the stops and ISR in events with strong ISR.

We then divide the event into two hemispheres according to the thrust axis. The hemisphere containing the  $E_T^{\text{miss}}$  is identified as the sparticle hemisphere containing the decay products of the two stops. This is because we expect the sparticle hemisphere to contain the two neutralinos. The hemisphere opposite the direction of the  $E_T^{\text{miss}}$  is identified as the ISR hemisphere. All jets in the ISR hemisphere are considered to have originated from initial state radiation and all jets in the sparticle hemisphere are considered to have originated from one of the two stops.

The ISR identification algorithm can also be interpreted as an exclusive two jet clustering algorithm that seeks to simultaneously minimize the masses of both jets. This interpretation is a mathematically equivalent to the thrust axis interpretation. Since we are in the transverse center of mass frame, finding the thrust axis is the same as simultaneous maximizing the  $p_T$  of the sparticle and ISR systems. The total  $E_T$  of the event, shown in equation 8.3, is constant. Maximizing the  $p_T$  of the sparticle and ISR systems is identical to minimizing the masses of the sparticle and ISR systems. At the same time, the jet axes are guaranteed to be arranged in a back to back fashion because we in the transverse center of mass frame. The jet axis is therefore identical to the thrust axis.

$$E_T = \sqrt{(m^{\text{ISR}})^2 + (p_T^{\text{ISR}})^2} + \sqrt{(m^{\text{sparticle}})^2 + (p_T^{\text{sparticle}})^2} \quad (8.3)$$

### 8.3 PERFORMANCE OF INITIAL STATE RADIATION IDENTIFICATION ALGORITHM

We can check the performance of the thrust based initial state radiation (ISR) identification algorithm by plotting the ratio of reconstructed over true ISR  $p_T$  in signal simulation. Figure 8.2 shows

the distribution of the ratio of reconstructed vs true ISR  $p_T$  for 350 GeV stop mass and 172 GeV neutralino mass signal sample. Only events with fully hadronic stop decays and at least 400 GeV of true ISR  $p_T$  are accepted for this plot. Detector resolution effects on jets and  $E_T^{\text{miss}}$  are included when calculating the reconstructed ISR  $p_T$ .

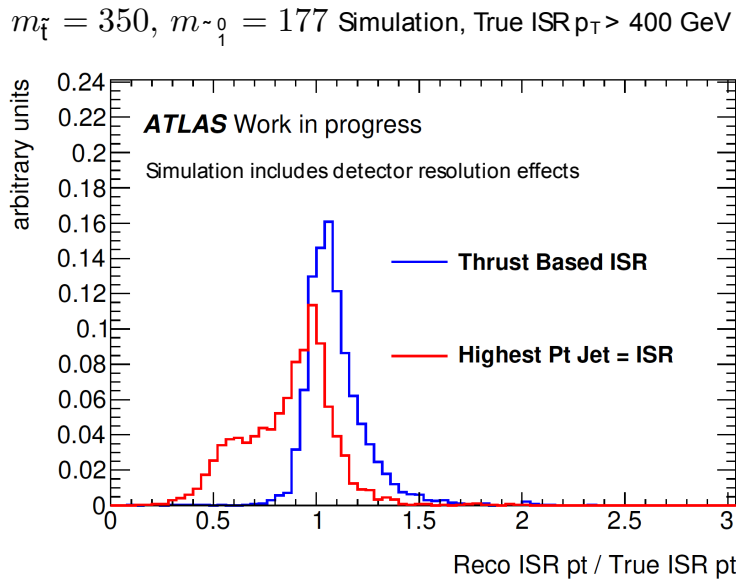


**Figure 8.2:** The distribution of the ratio of reconstructed vs true ISR  $p_T$  for the 350 GeV stop mass and 172 GeV neutralino mass signal sample. Only simulations with fully hadronic stop decays and at least 400 GeV of true ISR  $p_T$  are accepted. The red distribution is formed when the whole ISR system is equated to just the highest  $p_T$  jet. The blue distribution uses the thrust based ISR identification system.

A simple and currently popular form of ISR identification is simply the equating the highest  $p_T$  jet with the ISR system. The highest  $p_T$  jet algorithm is represented by the red distribution in figure 8.2. The single jet algorithm loses 20 to 50 percent of the ISR energy in about 40 percent of events. This is because the ISR system's energy is often split between multiple jets.

In comparison, the thrust based ISR identification system is able to capture the whole ISR system

consisting of multiple jets. The fitted gaussian width of the blue peak is 9 percent and this uncertainty includes detector resolution effects. The gaussian mean is centered about 1.05. The reason for this is because a jet originating from a stop will occasionally go in the opposite direction as the  $E_T^{\text{miss}}$  and be misidentified as an ISR jet. The  $p_T$  of the misidentified sparticle jet tend to be small when compared to the total  $p_T$  of the ISR system. Hence, this misidentification shows up as a 5 percent bias in the reconstructed ISR  $p_T$ . Optimization of the ISR identification algorithm shows that this small bias does not impact the sensitivity of the search.

The non-gaussian tail in the blue distribution that extends to a reconstructed over true ISR  $p_T$  ratio of 1.5 is due to energetic ISR jets that go in the same direction as the  $E_T^{\text{miss}}$ . In these cases, the ISR jets that are in the same direction as the  $E_T^{\text{miss}}$  are miss-reconstructed as having originated from a stop. Only the ISR jets going in an opposite direction to the  $E_T^{\text{miss}}$  are reconstructed as ISR jets. Therefore the reconstructed ISR system fail to partially cancel the  $p_T$  of the oppositely facing jets and the reconstructed ISR system has a larger  $p_T$  than the true ISR  $p_T$ . However, these cases are rare and the non-gaussian tail accounts for less than 15 percent of the events in blue distribution.

#### 8.4 KINEMATIC VARIABLES OF INITIAL STATE RADIATION AND SPARTICLE SYSTEMS

Once we separated the event into two hemispheres according the thrust axis as described in section 8.2 we can construct a number of kinematic variables that captures different features of the two hemispheres. These variables are listed below.

$N_{\text{btag}}^s$ : number of b-tagged jets associated with the sparticle hemisphere.

$N_{\text{jet}}^S$ : number of jets associated with the sparticle hemisphere.

$p_{T,b}^{\circ,S}$ :  $p_T$  of the leading b-tagged jet in the sparticle hemisphere.

$p_T^{\text{jet } 4, S}$ :  $p_T$  of the fourth highest  $p_T$  jet in the sparticle hemisphere.

$M_T^S$ : transverse mass of the whole sparticle system and  $E_T^{\text{miss}}$ .

$p_T^{\text{ISR}}$ :  $p_T$  of the ISR system

$\Delta\phi_{\text{ISR}, I}$ : angular separation in  $\phi$  of the ISR and the  $E_T^{\text{miss}}$  (evaluated in the transverse CM frame)

$R_{\text{ISR}}$ : Ratio between  $E_T^{\text{miss}}$  and  $p_T^{\text{ISR}}$  (evaluated in transverse CM frame)

$N_{\text{jet}}^S$  and  $N_{\text{btag}}^S$  quantify the jet multiplicity in the sparticle system.  $p_{T,b}^{\circ,S}$ ,  $p_T^{\text{jet } 4, S}$ ,  $M_T^S$  and  $p_T^{\text{ISR}}$

quantify the amount of energy in the sparticle and ISR hemispheres. Finally,  $\Delta\phi_{\text{ISR}, I}$  and  $R_{\text{ISR}}$  describe the correlation between the ISR system and the  $E_T^{\text{miss}}$  in direction and magnitude. All of these variables will be used to separate signal from background in the signal region described in detail in section ??.

# 9

## Collision Data Samples

### 9.1 DATA PERIODS AND GOOD RUN LIST

This analysis uses the LHC proton-proton collision data at a centre-of-mass energy of  $\sqrt{s}=13$  TeV that is collected by ATLAS in 2015 and 2016.

We select for data where all relevant subdetector parts are running without defects and the quality of data is good. This is done by requiring the data pass a good run list (GRL). The good run list is

compiled after manual and automated checks were performed on both detector hardware and the kinematics of reconstructed physics objects.

The GRLs used for the 2015 dataset is `data15_13TeV.periodAllYear_DetStatus-v79-repro20-02_DQDefects-00-02-02_PHYS_StandardGRL_All_Good_25ns.xml`.

The GRL for the 2016 data is `data16_13TeV.periodAllYear_DetStatus-v83-pro20-15_DQDefects-00-02-04_PHYS_StandardGRL_All_Good_25ns.xml`.

The dataset after GRL selection has a total integrated luminosity of  $36.47 \pm 1.2 \text{ fb}^{-1}$ . The total integrated luminosity as a function of time for 2015 and 2016 before the requirement of an GRL is shown in figure 9.1.

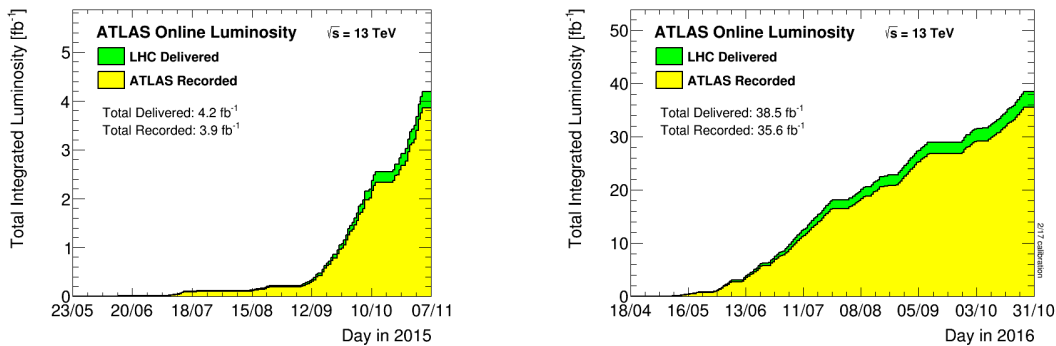


**Figure 9.1:** Distribution of the amount of data delivered by the LHC and recorded ATLAS vs time in 2015 and 2016

Peak luminosity reached  $1.38 \times 10^{34} \text{ cm}^{-2} \text{ sec}^{-1}$  in 2016. Taking data at this high rate means we expect multiple proton proton interactions in every bunch crossing. The average number of interactions per bunch crossing,  $\langle \mu \rangle$ , is 13.7 in 2015 and 23.2 in 2016. The distribution of the mean number of interactions per bunch crossing is given in figure 9.2.

In order to keep data flow to a manageable size, ATLAS only record events if a trigger is fired.

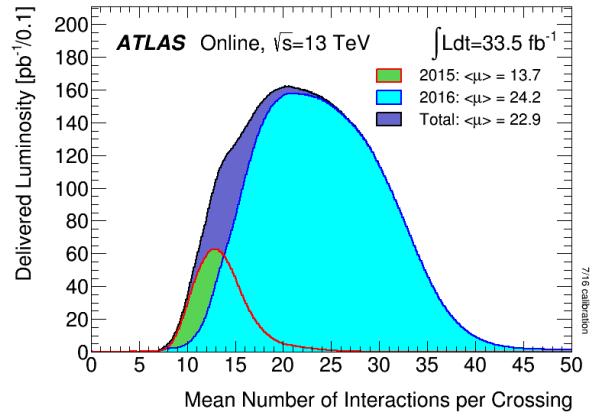


**Figure 9.2:** Distribution of the mean number of interactions per bunch crossing weighted by integrated luminosity for 2015 and 2016 ATLAS data taking.

The ATLAS trigger system is summarized in chapter 4. This analysis uses the lowest unprescaled  $E_T^{\text{miss}}$  trigger for each data taking period. This trigger is `HLT_xe70_tc_lcw` for all of 2015 data taking, `HLT_xe90_mht_L1XE50` for 2016 period A-D3, `HLT_xe100_mht_L1XE50` for 2016 period D4-F1, and `HLT_xe110_mht_L1XE50` for 2016 period F2 and onward.

# 10

## Event Preselection

We first require that the event pass a few basic selection to ensure that the events do not have large amounts of calorimeter noise or non-collision backgrounds. These requirements are called `event cleaning`, and `jet cleaning` and are designed to reject events with poorly reconstructed jets or  $E_T^{\text{miss}}$ . These basic selections are applied to all control regions (CR), validation regions (VR), and signal regions (SR).

A brief description of the selections is given below:

Cut 1 Data events must be in accepted according to the Good Runs List (GRL) described in chapter 9.1. This ensures all relevant subdetector of ATLAS are operating normally during data taking.

Cut 2 Remove events with noise bursts and possible incomplete events due to the TTC reset procedure from the data. Data events must have larError == 0, tileError == 0, SCT error == 0, and coreFlags &ox4000 == 0.

Cut 4 Require that at least one reconstructed primary vertex must exist.

Cut 5 Events must not contain any **BadLoose** jets with  $p_T > 20$  GeV (at any  $\eta$  range). Bad quality jets indicate the presence of calorimeter noise or non-collision backgrounds. Both can lead to poor  $E_T^{\text{miss}}$  reconstruction and hence, the whole event is rejected. **BadLoose** jets are defined in jet quality selection in section 3.3.4.

Cut 6 The event must not contain any cosmic muons. Cosmic muons are identified as muons with large impact parameters ( $|z_o| > 1$  mm and  $|d_o| > 0.2$  mm). Only baseline muons after overlap removal are considered in cosmic muon identification.

Cut 7 The event must not contain any **bad** muons. This include any muons reconstructed from high energy jets punching through the calorimeter and depositing energy into the muon system, or from poorly reconstructed inner detector tracks that are incorrectly matched to

muon spectrometer segments. These *fake* muons may result in misreconstructed  $E_T^{\text{miss}}$  so the whole event is rejected.

Details on all object definitions can be found in chapter 5.

On top of these basic requirements, additional **pre-selections** are applied to each control, validation, and signal region depending on the number of leptons required in the respective region.

### 10.1 ZERO LEPTON PRE-SELECTION

Any zero lepton region require the selections given in table ??.

GRL, Event Cleaning and Jet Cleaning	
	$E_T^{\text{miss}}$ Trigger
$E_T^{\text{miss}}$	$> 250 \text{ GeV}$
$N_{\text{baselineleptons}}$	0
anti- $k_t R = 0.4$ signal jets	$\geq 4, p_T > 80, 80, 40, 40 \text{ GeV}$
<i>b</i> -tagged signal jets	$\geq 1$
$ \Delta\phi(\text{jet}^{0,1}, E_T^{\text{miss}}) $	$> 0.4$
$E_T^{\text{miss,track}}$	$> 30 \text{ GeV}$
$ \Delta\phi(E_T^{\text{miss}}, E_T^{\text{miss,track}}) $	$< \pi/3$

**Table 10.1:** zero lepton pre-selection criteria common to all zero lepton signal and validation regions.

All zero lepton regions trigger on  $E_T^{\text{miss}}$  using the lowest unprescaled  $E_T^{\text{miss}}$  trigger for that data period. An offline selection of  $E_T^{\text{miss}} > 250 \text{ GeV}$  is required to ensure that all accepted events are on the trigger efficiency plateau. The trigger efficiency curve as a function of offline  $E_T^{\text{miss}}$  for select  $E_T^{\text{miss}}$  triggers can be seen in figure 4.2.

We require that the event contains exactly zero baseline leptons. We also require at least four signal jets with a minimum pt of (80, 80, 40, 40) GeV in the event. At least one signal jet must be b-tagged at the 77 percent working point. These jet energy and multiplicity requirements are loose and will be superseded by more stringent selections in the SR, VRs and CRs.

For our analysis the primary reason that QCD multijet background is able to pass the SR selections is due to misreconstructed jets. QCD multijet produces little intrinsic  $E_T^{\text{miss}}$ . In order to pass the 250 GeV  $E_T^{\text{miss}}$  requirement, multijet background need additional fake  $E_T^{\text{miss}}$  from mismeasured jets. For example, an extremely energetic jet may punch through the calorimeter and be reconstructed with a small  $E_T$ . This lost  $E_T$  maybe reconstructed as  $E_T^{\text{miss}}$ .

The  $|\Delta\phi(\text{jet}^{o,i}, E_T^{\text{miss}})| > 0.4$  requirement ensures that the  $E_T^{\text{miss}}$  is not collinear with the most energetic jets in the event. This provides strong rejection against fake  $E_T^{\text{miss}}$  resulting from a single misreconstructed energetic jet. Requirements on a loose agreement between  $E_T^{\text{miss}}$  and  $E_T^{\text{miss,track}}$  also discriminate against  $E_T^{\text{miss}}$  resulting from misreconstructed jets and therefore QCD multijet.

## 10.2 ONE LEPTON PRE-SELECTION

The one lepton preselection is similar to the zero lepton preselection except for several important requirements. The one lepton preselection is summarized in table ??.

First, the one lepton selections use signal leptons instead of baseline leptons in zero lepton regions. The one lepton regions use lepton momentum information and therefore require higher quality leptons.

GRL, Event Cleaning and Jet Cleaning	
$E_T^{\text{miss}}$ Trigger	
$E_T^{\text{miss}}$	$> 250 \text{ GeV}$
$N_{\text{signallep}}$	I
$N_{\text{jets}}$	$\geq 4$
$b$ -tagged signal jets	$\geq 1$
$ \Delta\varphi(\text{jet}^{\text{o},\text{i}}, E_T^{\text{miss}}) $	$> 0.4$

**Table 10.2:** one lepton pre-selection criteria common to all one lepton signal and validation regions.

Next both signal leptons and signal  $R = 0.4 \text{ anti-} k_t$  jets are counted as jets in one lepton regions. This is because one lepton regions serve as control and validation regions and are designed to model the background in the signal region. The biggest background contributions in the signal region come from backgrounds that decay through the hadronic tau channel. As such, we use the electron or muon in the one lepton CR and VR to model the hadronic tau in the zero lepton SR.

The  $E_T^{\text{miss,track}} > 30 \text{ GeV}$  and  $|\Delta\varphi(E_T^{\text{miss}}, E_T^{\text{miss,track}})| < \pi/3$  requirements are removed because the QCD multijet contribution to one lepton regions is negligible. The  $|\Delta\varphi(\text{jet}^{\text{o},\text{i}}, E_T^{\text{miss}})| > 0.4$  selection is kept because the cut provides a closer modeling of the phase space in SR.

# 11

## Signal Region Definition

The kinematic selections in the signal region are designed to reject SM ttbar events which comprise 70-90 percent of all background in SR. The same selections are also effective at rejecting subdominant including  $W$ +jets, single top,  $Z$ +jets and QCD multijet backgrounds. This chapter first builds physical intuition on the kinematics of each SM background in section 11.1 with special emphasis on the dominate SM ttbar. A brief recap of the ISR reconstruction algorithm is given in section ??.

The SR definition is given in section II.2. The section goes into detail on the performance of the SR selections. Lastly the SR yields and background composition are covered in section ?? and II.4.

## II.1 PHYSICAL INTUITION ON HOW SIGNAL REGION SELECTIONS REJECT SM BACKGROUND

The zero lepton SR is designed specifically to reject the dominant ttbar background. The SR's design choice and signal and ttbar kinematics are summarized in this section. The SR's effect on subdominate backgrounds are also described near the end of the section. More detail on each SM background, including background estimation techniques, can be found in chapter 12.

95 percent of all ttbar which survive SR selection decay via the single hadronic tau and single lepton decay channels. SM ttbar that decays via the fully hadronic decay channel generates no little intrinsic  $E_T^{\text{miss}}$  and is negligible in SR. Therefore, understanding ttbar specifically require us to understand the single lepton decay channel where the leptonic top can decay via an electron, muon or tau.

Its important to note that a neutrino from a top decay cannot have a  $p_T$  anywhere near 250 GeV if the top decays at rest. Therefore, the  $E_T^{\text{miss}} > 250$  GeV requirement essentially forces the leptonic top to be boosted.

The leptonic top can gain boost only through one of two ways. Either the leptonic top recoils against the hadronic top in a back to back fashion or both tops recoil against strong ISR. This breakdown of SM ttbar into two kinematically distinct population is covered in more detailed in section 12.2.

The thrust axis contains important information in both populations. In the top/anti-top population, the thrust axis aligns along the top/anti-top back to back boost. In the ttbar+strong ISR population, the thrust axis aligns along the ISR/ttbar back to back boost.

Figure 11.1 illustrates example events from the two distinct ttbar populations and stop signal. We line up all three events according to their thrust axis and the hemisphere containing the  $E_T^{\text{miss}}$  displayed in the upper half.

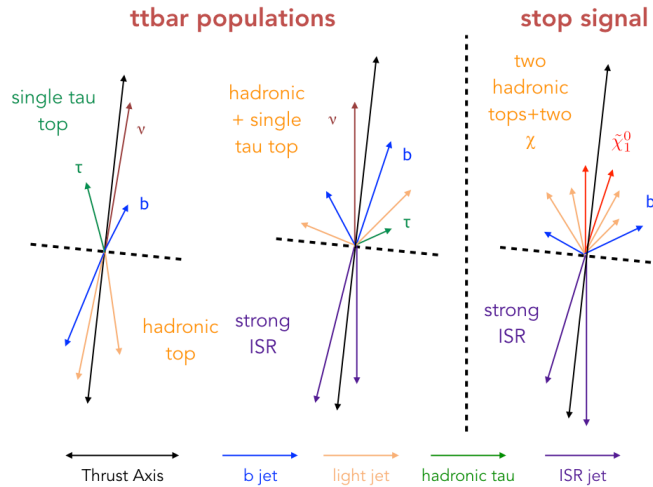


**Figure 11.1:** Basic depiction of the kinematics of the two ttbar populations and stop plus strong ISR events after 0 lepton pre-selection

We can immediately see that the signal has a significantly higher jet multiplicity and total energy in the hemisphere with the  $E_T^{\text{miss}}$  than the top/anti-top back to back population in ttbar. After all, the signal has 6 jets originating from the two hadronic tops in the hemisphere with  $E_T^{\text{miss}}$  compared with only a single leptonic top in the top/anti-top back to back ttbar population. The ttbar plus strong ISR population looks more signal like as it has higher jet multiplicity and energy in the

$E_T^{\text{miss}}$  hemisphere however, it still has less total energy than that of signal.

By cutting on the jet multiplicity and total energy in the hemisphere with  $E_T^{\text{miss}}$  we are able to reject 98 to 99 percent of ttbar events which already passed preselection but have less than 400 GeV of true ISR  $p_T$ . Acceptance of ttbar events increase with true ISR  $p_T$  but only asymptotically. Even at 1200 GeV of true ISR  $p_T$ , a ttbar event which already passed zero lepton preselection only has a 35 percent chance of passing the additional signal region selection.

After pre-selection, 90 percent of all ttbar events belong to the top/anti-top back to back population. The top/anti-top ttbar population dominates initially because it requires less total center of mass energy to boost a single top against the other instead of boosting both tops with additional strong ISR.

After SR selection, only approximately 10 percent of all ttbar events have true ISR  $p_T$  less than 400 GeV. A back of the envelope calculation shows that ttbar events need around 600 GeV of ISR  $p_T$  in order to boost the neutrino enough to pass the 250 GeV  $E_T^{\text{miss}}$  selection if both tops started at rest. The neutrino is not very effective at absorbing ISR  $p_T$  and must share the ISR  $p_T$  with the 5 other particles in the ttbar decay. This completely agrees with the true ISR  $p_T$  distribution in SR which peaks around 550 GeV for ttbar background in SR. The distribution of true ISR  $p_T$  of ttbar in SR can be seen in figure 11.2.

The analysis works by isolating ttbar with at least 550 GeV of ISR  $p_T$ . In comparison, a 400 GeV stop only require 440 GeV of ISR  $p_T$  to pass the 250 GeV  $E_T^{\text{miss}}$  requirement. We effectively gain an order of magnitude in signal to background ratio due to the larger differential cross-section on the lower required ISR  $p_T$ .

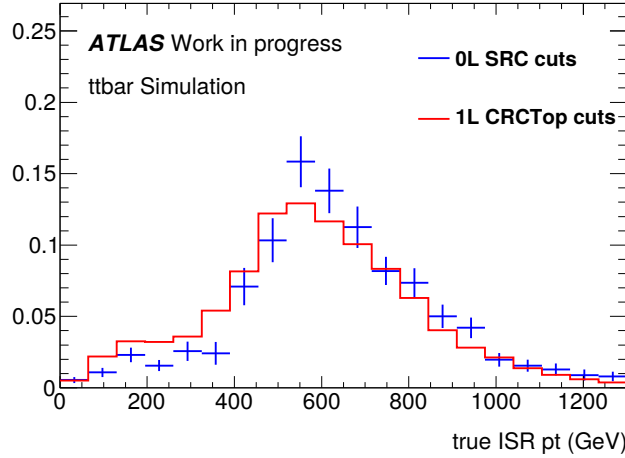


**Figure 11.2:** Distribution of true ISR pt for ttbar that survive the signal selections

At the same time, we gain another factor of 5 improvement simply by working in the zero lepton channel. The stop signal in SR decay mainly via the all hadronic decay channel with a 44 percent branching fraction. In comparison, 80 percent of ttbar background in SR decay via the hadronic tau channel with a branching fraction of approximately only 10 percent.

The  $E_T^{\text{miss}}$  and ISR correlations in direction and magnitude further improve the signal to background ratio by another factor of 5 to 10. When combined, we are able to over come the original 300 times difference in product cross-section between 400 GeV stop and ttbar.

As the stop mass increases, the required ISR  $p_T$  in signal decreases according to  $m_{\tilde{t}}/m \sim \frac{1}{\sqrt{s}}$ , further increasing the accepted signal differential cross-section even if the signal production cross-section is dropping. At the same time, the signal will peak at higher  $R_{\text{ISR}}$  ratios where background is rarer. In this way, the analysis is able to maintain sensitivity across a wide range of stop masses despite rapidly dropping signal production cross-section at high stop masses.

After zero lepton preselection, the signal to background ratio is 1 to 40 for a stop mass of 400 GeV.

After signal region selection we get an around 2 to 1 signal to background ratio for the same mass point. A quantitative breakdown of SR selection and yields is given in section 11.2 and 11.3.

At the same time, the same kinematic selections on jet multiplicity and total energy is also difficult for sub-dominant backgrounds such as  $W$ +jets,  $Z$ +jets, single top and QCD multijet to satisfy. It is in general difficult for these other processes to produce such high jet multiplicity and total energy in the same half of the event as the  $E_T^{\text{miss}}$ . Processes such as  $W$ +jets and  $Z$ +jets normally have the  $E_T^{\text{miss}}$  recoiling against other energetic jets. Therefore, energetic jets in these processes tend to lie in the hemisphere opposite the  $E_T^{\text{miss}}$ . Total subdominate background contributions to SR is around 10-30 percent depending on  $R_{\text{ISR}}$  region.

The kinematic variables used are reconstructed using the recursive jigsaw method. A detailed description of this method and variable defined can be found in section 8.2. In short, the recursive jigsaw method separates the event into two hemispheres according to the thrust axis. The thrust axis is the axis that maximizes the amount of back to back  $p_T$  along it and should approximate the direction of ISR and sparticle back to back recoil in events with strong ISR. The hemisphere containing the  $E_T^{\text{miss}}$  is considered the sparticle hemisphere and the hemisphere opposite the  $E_T^{\text{miss}}$  is considered the ISR hemisphere. All jets in the sparticle hemisphere is considered to have originated from one of the stop decays. All jets in the ISR hemisphere is considered to be an ISR jet. The performance of this ISR identification algorithm can be found in section 8.3.

We also construct variables that measure kinematic properties of both the ISR and sparticle hemispheres. These include  $N_{\text{btag}}^S$  and  $N_{\text{jet}}^S$  which describe the jet multiplicity of the sparticle system.

$M_T^S$ ,  $p_T^{jet\ 4,S}$ , and  $p_{T,b}^{o,S}$  are all related to the total energy in the sparticle system.  $p_T^{ISR}$  corresponds to the total  $p_T$  of the ISR system. Finally  $R_{ISR}$  and  $\Delta\phi_{ISR, I}$  quantify the correlation between the ISR system and  $E_T^{\text{miss}}$  in both direction and magnitude.

## II.2 SIGNAL REGION KINEMATIC SELECTION

Kinematic Selections for Signal Region is defined in table II.1.

**Table 11.1:** Signal region definitions, in addition to the preselection requirements presented in Table ??.

Variable	SRC-1	SRC-2	SRC-3	SRC-4	SRC-5
$N_{b-jet}^S$			$\geq 1$		
$N_{jet}^S$			$\geq 5$		
$p_T^{ISR}$			$> 400 \text{ GeV}$		
$p_{T,b}^{o,S}$			$> 40 \text{ GeV}$		
$p_T^{4,S}$			$> 50 \text{ GeV}$		
$m_S$			$> 300 \text{ GeV}$		
$\Delta\phi_{ISR, E_T^{\text{miss}}}$			$> 3.00$		
$R_{ISR}$	0.30-0.40	0.40-0.50	0.50-0.60	0.60-0.70	0.70-0.80

The selections on  $N_{jet}^S$  and  $N_{b-jet}^S$  ensures that the hemisphere with  $E_T^{\text{miss}}$  has high amounts of jet multiplicity. These requirements are naturally satisfied in signal events because the two neutralinos naturally go in the same direction as the six jets from the two stop decays. However this requirement is more difficult to satisfy for the top/anti-top back to back ttbar population since only a single leptonic or hadronic tau top is in the same hemisphere as the  $E_T^{\text{miss}}$  in the top/anti-top back to back

population.

The ttbar plus strong ISR population is able to pass this selection as both the leptonic and hadronic tops are in sparticle hemisphere. The result is the main background is ttbar plus strong ISR pt events pass after a requirement on the sparticle jet multiplicity and the  $p_T^{\text{ISR}} > 400 \text{ GeV}$  requirement. For stop masses Signal to background ratio is around 1 to 5 after these selections.

Next we make a requirement on the total energy of the sparticle system. The total transverse mass of the sparticle system  $m_S$  must be greater than 300 GeV and the  $p_T$  of the jet with 4th highest  $p_T$  in the sparticle system must be greater than 50 GeV.  $p_{T,b}^{o,S}$  must also be greater than 40 GeV.

In general, the signal with two fully hadronic tops has more energy in the sparticle hemisphere then ttbar. The top/anti-top back to back recoil population is nearly eliminated by these selections. Of the ttbar events that passed zero lepton preselection, less than 2 percent of ttbar events with true ISR pt less than 400 GeV pass these additional requirements. Selection efficiency remain at approximately 35 percent even for ttbar events with greater than 600 GeV of true ISR pt. Signal to background ratio improves to around 1 to 2 after these selections.

Lastly we make the a selections on correlations between the  $E_T^{\text{miss}}$  and ISR systems.  $\Delta\phi_{\text{ISR},E_T^{\text{miss}}} > 3.0$  ensures the  $E_T^{\text{miss}}$  and ISR systems are back to back. The ISR system and  $E_T^{\text{miss}}$  must be nearly back to back in signal because the neutralino gains momenta mainly from ISR. On the other hand, the neutrino in SM ttbar gains significant momenta from the top decay and its correlation with ISR is not as strong. This is true for subdominant backgrounds including  $W+\text{jet}$  and single top.

The distribution of  $\Delta\phi_{\text{ISR},E_T^{\text{miss}}}$  with all previous selections on sparticle jet multiplicity and sparticle system energy applied is shown in figure 11.3.

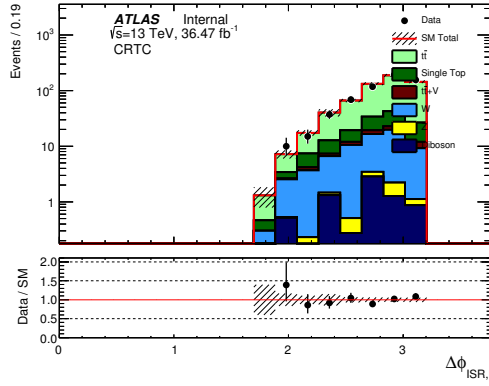


**Figure 11.3:**  $\Delta\phi_{\text{ISR}, E_T^{\text{miss}}}$  distributions for the zero lepton preselection plus sparticle jet multiplicity,  $p_T^{\text{ISR}}$ , and sparticle total energy requirement with  $36.47 \text{ fb}^{-1}$  of data. The ratio between data and MC is shown in the bottom panel. The hashed area in both the top and lower panel represent the uncertainty due to MC statistics and detector plus theoretical systematic uncertainties

After all signal selections, we get the final  $R_{\text{ISR}}$  distribution shown in figure 11.4. This  $R_{\text{ISR}}$  distribution is then separated into 5 bins from 0.3 to 0.8. The 5 SR bins are fitted simultaneously to extract the signal strength. We expect to receive very little signal events in  $R_{\text{ISR}}$  below 0.3 and the region is dominated by QCD background. As such the  $R_{\text{ISR}}$  region below 0.3 is not included in the final SR fit.

Stop samples with different stop and neutralino masses will peak in different locations in  $R_{\text{ISR}}$  with a signal to background ratio of approximately 2 to 1 under the peak. The simultaneous fit to all five bins captures this peaking feature in  $R_{\text{ISR}}$  for any stop mass.

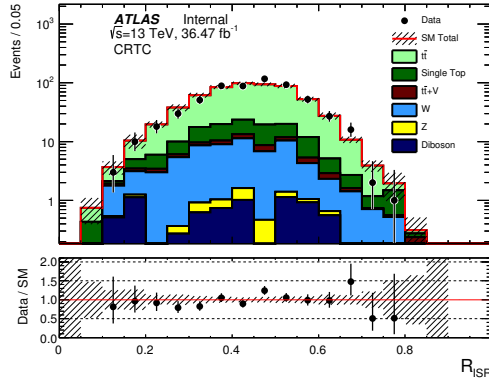


**Figure 11.4:**  $R_{ISR}$  distribution after signal region selection with  $36.47 \text{ fb}^{-1}$  of data. The ratio between data and MC is shown in the bottom panel. The hashed area in both the top and lower panel represent the uncertainty due to MC statistics and detector plus theoretical systematic uncertainties

### II.3 SIGNAL REGION EXPECTED YIELDS AND KINEMATIC DISTRIBUTIONS

The expected yields in SR is given in table II.2. All backgrounds have been normalized to control regions defined in chapter 12. Signal yields for three example signal samples with stop, neutralino masses of  $(300, 127 \text{ GeV})$ ,  $(400, 227 \text{ GeV})$ , and  $(500, 327 \text{ GeV})$  are also shown for comparison. We achieved a 1 to 1 to 2 to 1 signal to background ratio under the signal  $R_{ISR}$  peak in SR.

Plots of signal region distribution for select kinematic variables are shown in figure II.5

### II.4 SIGNAL REGION BACKGROUND COMPOSITION

The dominate background in all signal region bins is standard model pair produced tops ( $t\bar{t}$ ). The breakdown of background composition is given in table ??

$t\bar{t}$  accounts for 85 percent of all backgrounds in the signal region. The next most prevalent

SRC <sub>1</sub>		SRC <sub>2</sub>		SRC <sub>3</sub>	
Z	$0.11 \pm 0.03$	Z	$0.43 \pm 0.09$	Z	$0.86 \pm 0.12$
dibosons	$0.04 \pm 0.04$	dibosons	$0.41 \pm 0.28$	dibosons	$0.24 \pm 0.21$
ttbar	$1.99 \pm 0.46$	ttbar	$16.01 \pm 1.58$	ttbar	$28.65 \pm 1.99$
singleTop	$0.09 \pm 0.06$	singleTop	$1.26 \pm 0.44$	singleTop	$0.96 \pm 0.17$
ttV	$0.03 \pm 0.04$	ttV	$0.23 \pm 0.09$	ttV	$0.39 \pm 0.18$
W	$0.46 \pm 0.23$	W	$0.59 \pm 0.13$	W	$1.38 \pm 0.27$
Total MC	$2.72 \pm 0.52$	Total MC	$18.94 \pm 1.67$	Total MC	$32.47 \pm 2.04$

SRC <sub>4</sub>		SRC <sub>5</sub>	
Z	$0.71 \pm 0.14$	Z	$0.44 \pm 0.10$
dibosons	$0.49 \pm 0.41$	dibosons	$0.15 \pm 0.10$
ttbar	$21.07 \pm 1.54$	ttbar	$6.33 \pm 0.72$
singleTop	$1.00 \pm 0.39$	singleTop	$0.53 \pm 0.14$
ttV	$0.39 \pm 0.09$	ttV	$0.08 \pm 0.08$
W	$1.43 \pm 0.34$	W	$1.38 \pm 0.37$
Total MC	$25.09 \pm 1.69$	Total MC	$8.91 \pm 0.84$

**Table 11.2:** Signal Region expected discovery significance for select samples with 20% background systematic uncertainty.

**Table 11.3:** Standard Model Background Composition in the Signal Region ??.

$R_{ISR}$ Range	0.20-0.30	0.30-0.40	0.40-0.50	0.50-0.60	0.60-0.70	0.70-0.80
t $\bar{t}$						
W+jets						
Z+jets						
Others (dibosons+Single Top+QCD)						

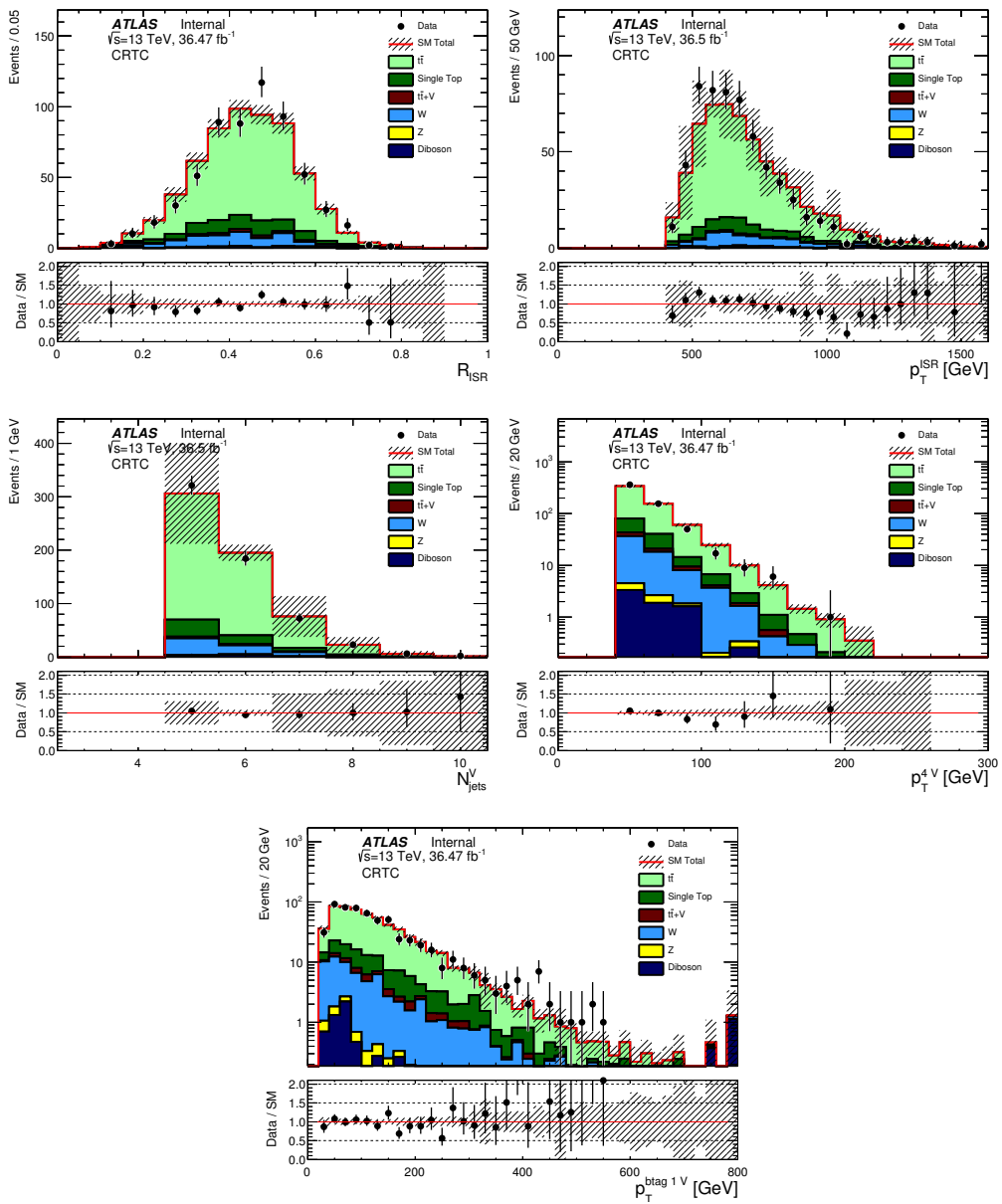


**Figure 11.5:** Distributions for signal region selection. The ratio between data and MC is shown in the bottom panel. The hashed area in both the top and lower panel represent the uncertainty due to MC statistics and detector plus theoretical systematic uncertainties

background is W+jets which can reach up to 15 percent in high  $R_{\text{ISR}}$  bins.

# 12

## Standard Model Backgrounds

### 12.1 COMMON BACKGROUND ESTIMATION AND VALIDATION TECHNIQUES

We use both data and MC based background estimation technique for estimating background in the signal region. A common partially data driven technique directly measures the amount of background in kinematically similar control regions (CR) in data. Once we know the amount of background in the CR, we can then extrapolate to the signal region using MC predictions.

We determined the background rate through a simultaneous fit to all SR and CRs when setting limits or calculating discovery significances. The background rate will be mainly constrained by the CRs because the CRs have significantly higher statistics than SR.

We also perform a background only fit to estimate the background rates. The background only fit extracts a normalization factor for each background by simultaneously fit all control regions. The normalization factors are then applied to the expected background rates in SR. The background only fit results may differ from the combined fit. However the two estimate should be similar as long as the CRs are well designed. A more detailed explanation of CR, SR and fitting procedures are covered in the statistical analysis chapter 14.

We use control regions to estimate the dominant ttbar background and subdominant W+jet, single top, and ttV backgrounds. Z+jets and diboson backgrounds are estimated using MC alone. Z+jets and dibosons contribute less than 5 percent of all backgrounds in the SR and we allow for an additional 100 percent theory uncertainty for these two samples. Finally QCD multijet background is estimated using the jet smearing method described in section 12.3.6. Details on the ttbar background is found in section 12.2. Details on the treatment of each sub dominate background can be found in section 12.3.

The scale factors for each background derived from the simultaneous fit to the CR are given in table 12.1. ttbar background is scaled down by 0.707 because the MC over estimates the amount of ttbar that is produced with strong ISR.

MC sample	Fitted scale factor
ttbar (SRA_TT)	$1.147 \pm 0.146$
ttbar (SRA_TW)	$1.150 \pm 0.114$
ttbar (SRA_To)	$0.856 \pm 0.123$
ttbar (SRB_TT)	$1.219 \pm 0.160$
ttbar (SRB_TW)	$1.009 \pm 0.0697$
ttbar (SRB_To)	$0.904 \pm 0.0524$
ttbar (SRC)	$0.674 \pm 0.0479$
ttbar (SRD)	$1.032 \pm 0.110$
ttbar (SRE)	$1.041 \pm 0.1083$
W+jets	$1.122 \pm 0.155$
Z+jets (SRA,B TT and TW)	$1.213 \pm 0.232$
Z+jets (SRA,B To)	$1.115 \pm 0.143$
Z+jets (SRD)	$1.081 \pm 0.145$
Z+jets (SRE)	$1.233 \pm 0.149$
Single top	$1.211 \pm 0.389$
ttbar $\gamma$	$1.275 \pm 0.184$

**Table 12.1:** MC scale factors for SM backgrounds. Scale factors are derived by simultaneously fitting to all background CR using  $36.47 \text{ fb}^{-1}$  of data.

## 12.2 DOMINANT BACKGROUND: STANDARD MODEL $t\bar{t}$

The dominant background in this analysis is SM ttbar. After signal selection ttbar still accounts for 70-90 percent of the background depending on the  $R_{\text{ISR}}$  range. This section covers in detail the properties and treatment of SM ttbar in this analysis. The section 12.2.1 demonstrates that there exists two kinematically distinct populations of SM ttbar, each with unique characteristics and observables. Section 12.2.2 describes how we are able to directly measure the amount of ttbar in SR using a one lepton CR.

### 12.2.1 TWO KINEMATICALLY DISTINCT POPULATIONS OF $t\bar{t}$

After the zero lepton preselection, 80 percent of ttbar events decay via the single hadronic tau channel. 15 percent of ttbar events decay via the single lepton channel where the lepton is an electron or a muon. The lepton is later lost because either it has too low  $p_T$  to be reconstructed, removed because they were too close to another jet or is mis-reconstructed as a jet. The rest of the five percent are due to di-leptonic decays. Fully hadronic ttbar is negligible after SR selections because they produce little intrinsic  $E_T^{\text{miss}}$ .

The  $E_T^{\text{miss}} > 250$  GeV requirement in preselection selects ttbar with boosted leptonic tops. A top at rest simply do not have enough energy to produce a neutrino with 250 GeV of  $p_T$ . The leptonic top can gain boost mainly through one of two ways. Either the leptonic top recoils in a back to back fashion against the hadronic top or both tops can recoil against strong ISR.

In both situations the axis of maximum back to back  $p_T$ , the thrust axis, contains important in-

formation. In the case where the leptonic is recoiling against the hadronic top, the thrust axis lines up along the top/anti-top's axis of back to back recoil. In the case where both tops are boosted by strong ISR, the thrust axis approximates the ttbar vs ISR recoil direction. An artistic representation of the role of the thrust axis in each ttbar population can be seen in figure 12.1.

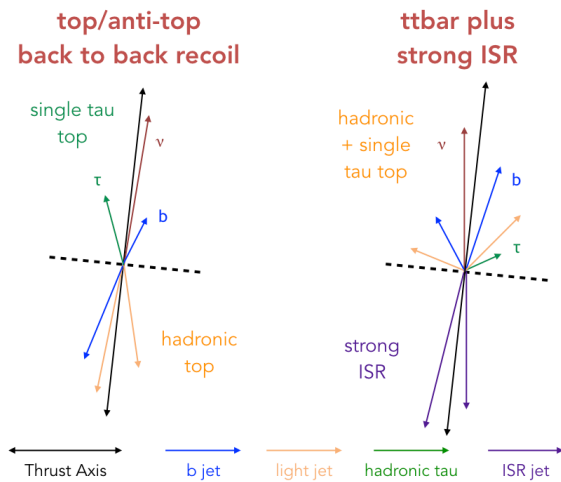


**Figure 12.1:** Depiction of the kinematics of the back to back ttbar population and the ttbar plus strong ISR population that exists after the zero lepton pre-selection. The two example event's thrust axis are aligned. The hemisphere containing  $E_T^{\text{miss}}$  has significantly higher jet multiplicities and total energy in ttbar plus strong ISR events.

The ttbar plus strong ISR population has on average much higher jet multiplicities and total energy in the hemisphere containing  $E_T^{\text{miss}}$ . Hence, we can use observable such as  $N_{\text{jet}}^S$  and  $M_T^S$  to distinguish ttbar plus strong ISR events from top/anti-top back to back recoil events.

### 12.2.2 PREDICTING THE AMOUNT OF $t\bar{t}$ IN SIGNAL REGION USING A ONE LEPTON CONTROL REGION

Stop signal is expected to have a higher jet multiplicities and energy in the hemisphere containing  $E_T^{\text{miss}}$  than both ttbar populations. The stringent SR requirements on the jet multiplicities and total energy of the sparticle hemisphere effectively eliminate the top/anti-top back to back ttbar population and also rejects approximately  $2/3$  of ttbar plus strong ISR population. A detailed explanation of SR design and performance can be found in chapter 11.

The ttbar events that survives the SR selections are composed of almost exclusively ttbar that are also produced with strong ISR. Approximately 90 percent of the ttbar events in SR have an ISR  $p_T$  of at least 400 GeV. A back of the envelope calculation shows that we need around 550-600 GeV of ISR  $p_T$  to boost the ttbar neutrino to above 250 GeV of  $p_T$ . The neutrino must share the ISR  $p_T$  with 5 other ttbar decay products and is not particularly efficient at absorbing ISR  $p_T$ . Figure 11.2 shows that the true ISR  $p_T$  distribution for ttbar in SR peaks at approximately 550 GeV. This demonstrates that the SR does indeed capture only ttbar with strong ISR  $p_T$ .

A direct consequence of selecting for only strong ISR ttbar is that the predicted ttbar background rates in SR is directly related to the amount of ISR/FSR in the MC. The next-to-leading order (NLO) POWHEG+PYTHIA6 ttbar MC gives upwards of 30 percent uncertainty due to ISR/FSR systematic. The ISR/FSR theoretical uncertainty would completely dominate if we relied on MC to predict SR ttbar rates.

In order to decrease the ISR/FSR uncertainty, we directly measure the ttbar plus strong ISR rate

in data using an one lepton ttbar CR (CRCTop). One lepton here refers only to electron and muons because they can be reconstructed with much greater purity then taus. The selections used to define the CRCTop is defined in table 12.2. All variables used are defined in section 8.4.

**Table 12.2:** One-lepton  $t\bar{t}$ +ISR control region (CRCTop) definitions. The same  $E_T^{\text{miss}}$  triggers as mentioned in Table ?? are used.

Variable	$1L 1b t\bar{t}CR$
1 Lepton Pre-Selection	
$N_{\text{lep}}$	= 1
$m_T(\ell, E_T^{\text{miss}})$	$< 80 \text{ GeV}$
$\Delta R(b_{o,1}, \ell)_{\text{min}}$	$< 2.0$
$N_{\text{jet}}^S$	$\geq 5$
$N_{\text{btag}}^S$	$\geq 1$
$p_T^{4,S}$	$> 40 \text{ GeV}$
$p_T^{\text{ISR}}$	$\geq 400$

CRCTop captures the same kinematic features as SR by targeting ttbar also produced with strong ISR  $p_T$ . The CR uses similar selections on the same kinematic variables as SR. The correlations on ISR and  $E_T^{\text{miss}}$  are removed to increase statistics and lower signal contamination. For example,  $\Delta\phi_{\text{ISR}, I}$  specifies the direction of neutrino relative to the direction of the ISR. A requirement of  $\Delta\phi_{\text{ISR}, I} > 3.0$  essentially selects specific ttbar decay axis. Removing this cut opens up more phase space to ttbar decays but does not change the requirement on strong ISR  $p_T$ .

Figure 12.2 shows the true ISR  $p_T$  distribution for ttbar in SR and CR. Both distributions peak at roughly 550 GeV and have similar shapes. The one lepton CR essentially measures the amount of

ttbar plus strong ISR directly in data. By normalizing ttbar background rates to the CR, we are able to limit the ISR/FSR uncertainty to below 10 percent for all  $R_{\text{ISR}}$  regions.

The close kinematic selection between CRCTop and SR also allow leads to cancelation of other systematics. For example, the 6 percent uncertainty on jet energy scale and jet energy resolution can be partial attributed to the CR and SR requiring jets of similar  $p_T$ . A more detailed discussion of systematics can be found in chapter 13

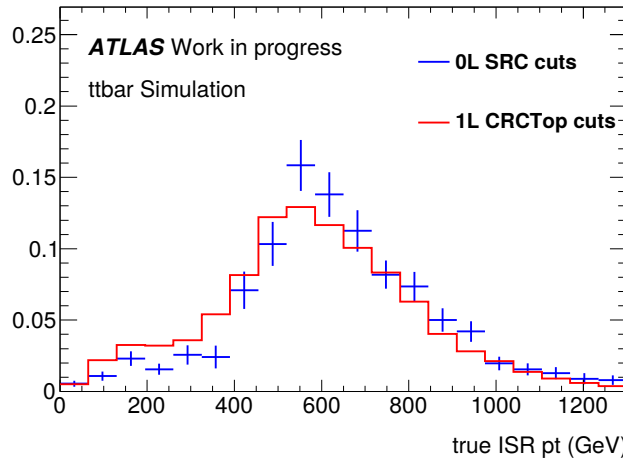


**Figure 12.2:** Distribution of true ISR  $p_T$  for ttbar that survive the CR and SR selections. Both peak at roughly 550 GeV demonstrating that the one lepton CR and zero lepton SR captures the same population of ttbar plus strong ISR. Therefore, the one lepton CR essentially measures the amount of ttbar in SR directly from data with little extrapolation over ISR  $p_T$ .

In the one lepton CRCTop, the lepton is included as a “jet” in the Jigsaw ISR algorithm and will be counted as a sparticle jet or an ISR jet depending on which hemisphere it falls. The lepton is meant to play the role of a hadronic tau jet in the zero lepton SR. This approximation is justified since roughly 80 percent of all ttbar events in SR decay via the hadronic tau channel.

Stop signal, especially those with  $\Delta m \neq m_t$ , tend to produce more  $E_T^{\text{miss}}$  because of the pres-

ence of neutralinos. A cut of  $m_T(\ell, E_T^{\text{miss}}) < 80 \text{ GeV}$  is added to remove signal contamination. A  $\Delta R(b_{\text{o},i}, \ell)_{\text{min}} < 2.0$  cut is added to increase ttbar purity and ensure orthogonality to the W+jets control region.

The  $p_T^{\text{jet } 4, S} > 50 \text{ GeV}$  cut is relaxed to  $p_T^{\text{jet } 4, S} > 40 \text{ GeV}$  in order to increase statistics in the CR. The  $p_T^{\text{jet } 4, S}$  cut specifies the  $p_T$  of the 4th jet in the sparticle system. The  $p_T^{\text{jet } 4, S}$  cut can be correlated with ISR/FSR because there is a chance that the 4th most energetic jet in the sparticle system is from radiation and not from a top decay. However for this analysis it is more important to accurately gauge the amount of hard ISR of order hundred or more GeV that the ttbar system recoils against then amount of additional radiation in the same hemisphere as  $t\bar{t}$ . We found that loosening  $p_T^{\text{jet } 4, S}$  cut to 40 GeV does not result in a large difference in the true ISR pt distribution in the CRCTop and SR.

## CRCTOP SIGNAL CONTAMINATION

Signal contamination in CRCTop ranges from 1 percent at high stop masses to 12 percent at low stop masses for all mass points not already excluded by previous stop experiments. The largest signal contamination occurs at a stop mass of 225 to 250 GeV. Here, the signal contamination approaches 12 percent due to the large stop production cross-section. Lower stop masses result in higher signal contamination but our search does not have sensitivity to regions below 225 GeV.

The fact that CRCTop can attain such low signal contamination while selecting for ttbar background with such similar kinematic features as SR is impressive. The SR has a signal to background ratio of approximately 2 to 1 for stop masses between 250 GeV and 400 GeV. In comparison, CRC-

Top is able to achieve SR contamination of around 5 to 12 percent for the same signal points.

CRCTop is able to make up for this factor of 20-40 difference in S/B rate mainly due to two reasons. First CRCTop is a one lepton control region. Working in the one lepton region means both signal and ttbar background draw from the single muon and single electron decay channels. Signal and background therefore has similar decay fractions in CRCTop. The SR, on the other hand, mainly selects for signal with two tops that decay fully hadronically with roughly a 44 percent branching fraction. In comparison, the ttbar background in SR main decay via the single hadronic tau decay channel with only a 10 percent decay fraction. The CR therefore has a factor of 5 decrease in S/B ratio compared to the SR based on branching fraction alone.

The SR also gains S/B by enforcing the correlations between the ISR system and  $E_T^{\text{miss}}$ . Removing the  $\Delta\phi_{\text{ISR}, I} > 3.0$  requirements decreases S/B by another factor of 3. Including all regions of  $R_{\text{ISR}}$  in CRCTop and specifically targeting the  $R_{\text{ISR}}$  window under the signal peak decreases the S/B of 2 to 5 to the S/B depending on the stop mass and location of signal  $R_{\text{ISR}}$  peak. Removing the requirement on these correlations do no change the requirement on strong ttbar ISR  $p_T$  but opens up more phase space for ttbar to decay.

The two factors combine to make up the roughly factor of 30 decrease in S/B between SR and CRCTop; all the while preserving the agreement in true ttbar ISR  $p_T$  distribution shown in figure

12.2.

## CRCTop DISTRIBUTIONS

Distribution of important variables after normalization to  $36.47 \text{ fb}^{-1}$  of data are shown for CRCTop in figure 12.3. There seem to be no significant slope in the data over MC comparison in the CRCTop  $p_T^{\text{jet } 4, S}$  distribution. This is further evidence that the extrapolation from 40 to 50 GeV across  $p_T^{\text{jet } 4, S}$  is allowed.

There is a noticeable trend in the data over MC comparison in the CRCTop  $p_T^{\text{ISR}}$  distribution. The disagreement is not surprising given that a priori we have an 30 percent uncertainty due to the ISR/FSR uncertainty. This further demonstrate the need for a CR that directly measures the amount of ttbar with strong ISR pt in data.

The normalization scale factor for ttbar is 0.707 according to a background only fit on  $36.47 \text{ fb}^{-1}$  of data. This scale factor is quiet different from 1.0 which indicates that the ttbar MC alone does not well model the high ISR  $p_T$  phase space. Again, this difference is not unexpected given the 30 percent ISR/FSR uncertainty on ttbar MC.

### 12.2.3 VALIDATING $t\bar{t}$ PREDICTIONS IN SIGNAL REGION USING A ZERO LEPTON VALIDATION REGION

We also define a zero lepton ttbar VR to validate the predicted background rates in SR. The ttbar VR (VRCTop) is kinematically similar to SR but has the  $\Delta\phi_{\text{ISR}, I} < 3.0$  selection is inverted to ensure orthogonality and limit signal contamination. In ttbar events,  $\Delta\phi_{\text{ISR}, I}$  specifies the direction of neutrino relative to the direction of the ISR. Inverting the  $\Delta\phi_{\text{ISR}, I}$  selection only selects for ttbar

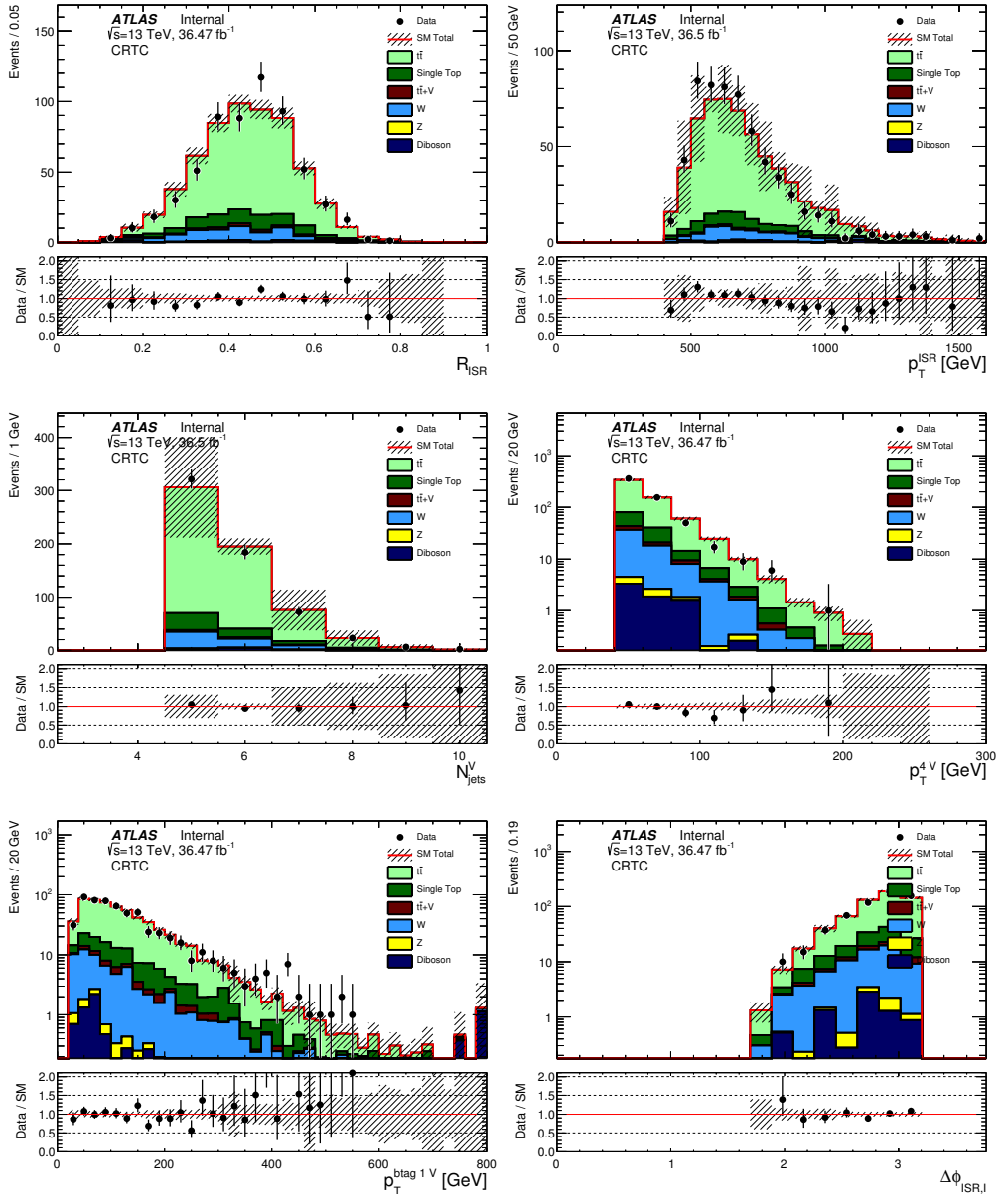


**Figure 12.3:** One lepton ttbar CR (CRCTop) distributions for  $36.47 \text{ fb}^{-1}$  of data. All backgrounds have already been normalized to CRs by performing a background only fit. The ratio between data and MC is shown in the bottom panel. The hashed area in both the top and lower panel represent the uncertainty due to MC statistics and detector systematic uncertainties.

**Table 12.3:** Zero-lepton  $t\bar{t}$ +ISR validation region definitions, in addition to the SRC requirements listed in Table ??.

Variable	
$N_{\text{jet}}^{\text{s}}$	$\geq 4$
$N_{\text{btag}}^{\text{s}}$	$\geq 1$
$p_T^{\text{btag } 1, \text{ s}}$	$\geq 40$
$p_T^{\text{ISR}}$	$\geq 400$
$M_T^{\text{s}}$	$> 100 \text{ GeV}$
$M_T^{\text{s},\text{vis}}/M_T^{\text{s}}$	$< 0.6$
$\Delta\phi_{\text{ISR}, I}$	$< 3.00$

with a different decay axis but does not change the requirements on strong ISR  $p_T$ . The  $\Delta\phi_{\text{ISR}, I} < 3.0$  selection does effectively reject stop events because the neutralinos gain all their momenta from the ISR system in signal.

The requirement on  $M_T^{\text{s}}$  is reduced to 100 GeV (vs. 300 GeV in the SR) and an  $N_{\text{jet}}^{\text{s}} \geq 4$  selection is applied (vs.  $N_{\text{jet}}^{\text{s}} \geq 5$  in the SR) to enhance the yields of semi-leptonic  $t\bar{t}$  events. A requirement of  $M_T^{\text{s},\text{vis}}/M_T^{\text{s}} < 0.6$  is added to reduce signal contamination and reject QCD multijet background.

Similar to CRCTop, the  $p_T^{\text{jet } 4, \text{ s}} > 50 \text{ GeV}$  selection is relaxed to  $p_T^{\text{jet } 4, \text{ s}} > 40 \text{ GeV}$  to increase VR statistics.

The distributions of the selection variables in VRCTop are shown in Fig. 12.4. The background rates have been normalized to CRs through the use of a background only fit to  $36.47 \text{ fb}^{-1}$  of data. The predicted background rate in the VRCTop agrees with data to within  $1\sigma$ . This demonstrates

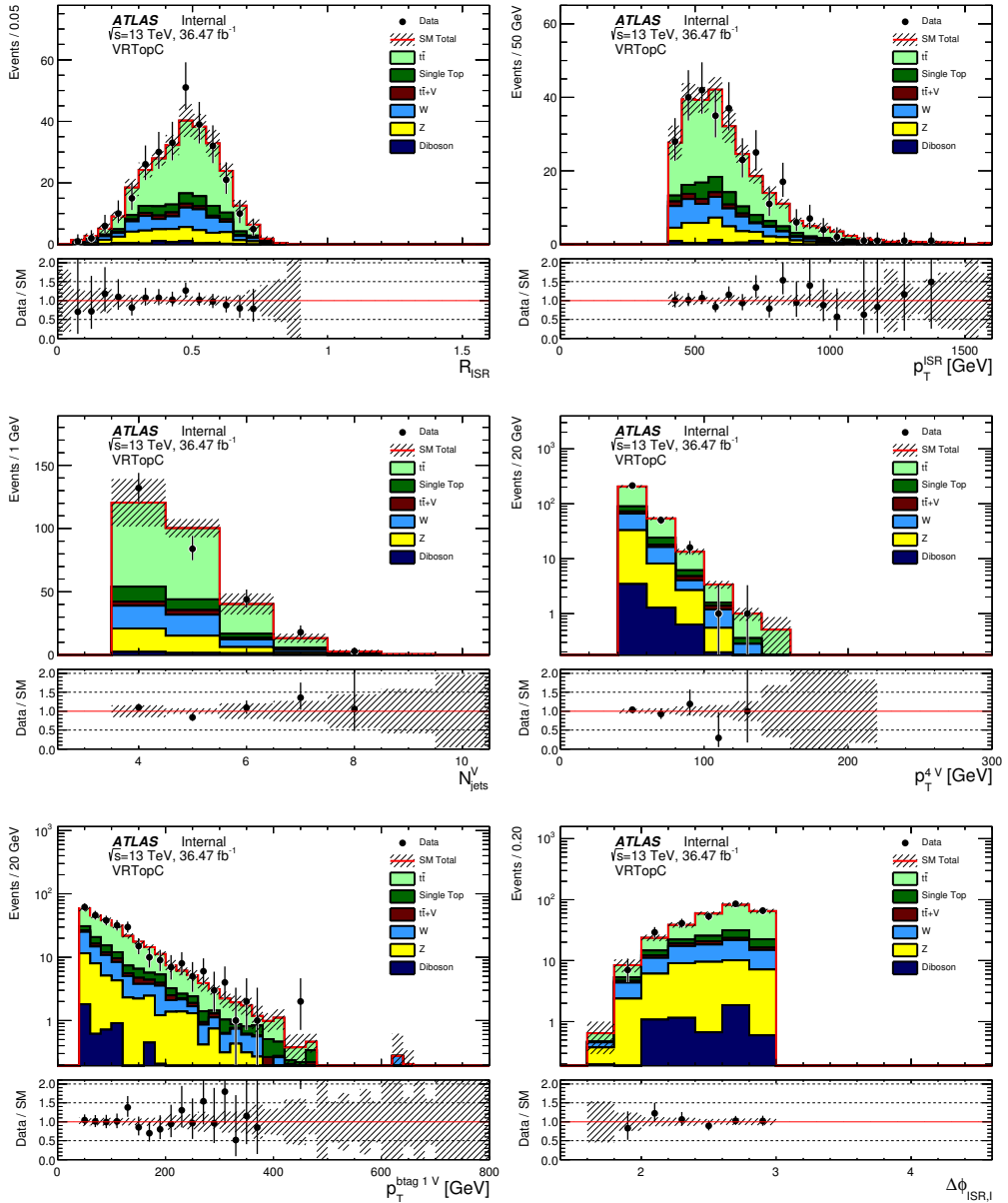


**Figure 12.4:** Distribution of select variables in the zero lepton  $t\bar{t}$  validation region. The ratio between data and MC predictions are shown in the bottom panel. The background rates have been normalized to CRs through the use of a background only fit to  $36.47 \text{ fb}^{-1}$  of data. Experimental systematic uncertainties on background predictions are depicted as the hashed bands.

that CRCTop is an effective predictor of ttbar background rates in VR and SR. The  $R_{\text{ISR}}$  shape is well modeled as we see no distinct trends in the data vs MC ratio in  $R_{\text{ISR}}$ .

Similar to CRCTop, there is a noticeable trend in the data over MC comparison in the VRCTop  $p_T^{\text{ISR}}$  distribution. Again this is expected because the MC is a poor predictor of ISR  $p_T$  rates. The fact that data in VRCTop agrees with the predicted background rate proves that CRCTop can effectively measure the amount of ttbar with at least 400 GeV of ISR  $p_T$ .

### 12.3 SUBDOMINANT BACKGROUNDS

#### 12.3.1 STANDARD MODEL W+JETS

$W$  boson produced in conjunction with QCD jets ( $W$ +jets) consists our largest sub-dominant background.  $W$ +jets consists of 5 percent of the total background in the SR. However the distribution of  $W$ +jets is not uniform across  $R_{\text{ISR}}$ .  $W$ +jets can reach around 15 percent of all background in the SR bins with the largest  $R_{\text{ISR}}$ . This means the  $W$ +jets contribution mostly affects the signal with high stop masses because those signal samples peak at high  $R_{\text{ISR}}$ .

We estimate  $W$ +Jets using a 1 lepton control region defined in section 12.3.1. The 1 lepton  $W$ +jet CR is orthogonal to the 1 lepton ttbar CR and 1 lepton single top CR defined in table 12.2 and ??.

#### $W + \text{jets}$ CONTROL REGION

The 1 lepton  $W$ +jet CR is designed to reject top events and ensure high  $W$ +jet purity. The definition of the  $W$ +jets CR is given in table 12.4.

**Table 12.4:** Summary of the selection for the 1-lepton,  $W$ +jets control regions.

	CRW
Number of leptons	1
Number of jets (incl. lepton)	$\geq 4$
$p_T$ of jets (incl. lepton)	(80, 80, 40, 40) GeV
$\min  \Delta\varphi(\text{jet}^{o-1}, E_T^{\text{miss}}) $	$> 0.4$
$E_T^{\text{miss}}$	$> 250$ GeV
$m_T(\ell, E_T^{\text{miss}})$	( $> 30, < 100$ GeV)
Number of $b$ -jets	= 1
$m_{\text{jet}, R=1.2}^o$	$< 60$ GeV
$\Delta R(b_{o,1}, \ell)_{\text{min}}$	$> 2.0$

The signal lepton is treated as a jet for the jet multiplicity and the jet  $p_T$  requirement as well as for the top reconstruction. The mass requirement on the large R jet  $m_{\text{jet}, R=1.2}^o < 60$  GeV rejects events with reconstructed boosted tops. The  $m_T(\ell, E_T^{\text{miss}})$  selection ensures that the transverse mass is consistent with those originating from a  $W$  boson.

Orthogonality between  $W$ +jet CR and the single top CR is ensured by the requirement on the number of  $b$ -jets. Orthogonality between ttbar CR and  $W$ +jet CR is ensured by the selection on  $\Delta R(b_{o,1}, \ell)_{\text{min}}$ , defined as the minimum  $\Delta R$  between the two jets with the highest b-tag value and the selected lepton. The signal contamination is less than 10% for all signal points.

Data vs MC comparisons in the  $W +$  jets control region are shown in histograms in figure 12.5. The expected MC background has been normalized to the amount of data in the  $W +$  jets control region by performing a simultaneous fit to all background CR. The hashed bands on the total SM background correspond to the amount of total experimental systematical uncertainty plus the MC

statistical uncertainty. The yield in the  $W +$  jets CR is given in table 12.5.

Data and MC are compatible to within statistical uncertainty. No strong trends are observed in the data to MC ratios in any of the distribution.

CRW (60% purity)	
Z	$1.99 \pm 0.45$
dibosons	$9.85 \pm 1.76$
ttbar	$128.42 \pm 3.82$
singleTop	$51.14 \pm 3.37$
ttV	$1.07 \pm 0.16$
W	$288.12 \pm 8.86$
Total MC	$480.58 \pm 10.38$
Data	$531.00 \pm 23.04$
SF	$1.17 \pm 0.10$

**Table 12.5:** Yields in the  $W +$  jets CR with  $36.47 \text{ fb}^{-1}$  of data.

### 12.3.2 STANDARD MODEL SINGLE TOP

Standard Model single top consists of 3 to 7 percent of the background in any one  $R_{\text{ISR}}$  bin. In total, single top consist of 4 percent of the total background in SRC. A 1 lepton single top control region is defined in section 12.3.2. The single top CR is orthogonal to both the 1 lepton  $W +$  jets control region and ttbar control region.

#### SINGLE TOP CONTROL REGION

The definition of the single top control region is given in table ??.

The signal lepton is treated as a jet for the jet multiplicity and the jet  $p_T$  requirement as well as for the top reconstruction. The  $m_T(\ell, E_T^{\text{miss}})$  selection ensures that the transverse mass is consistent

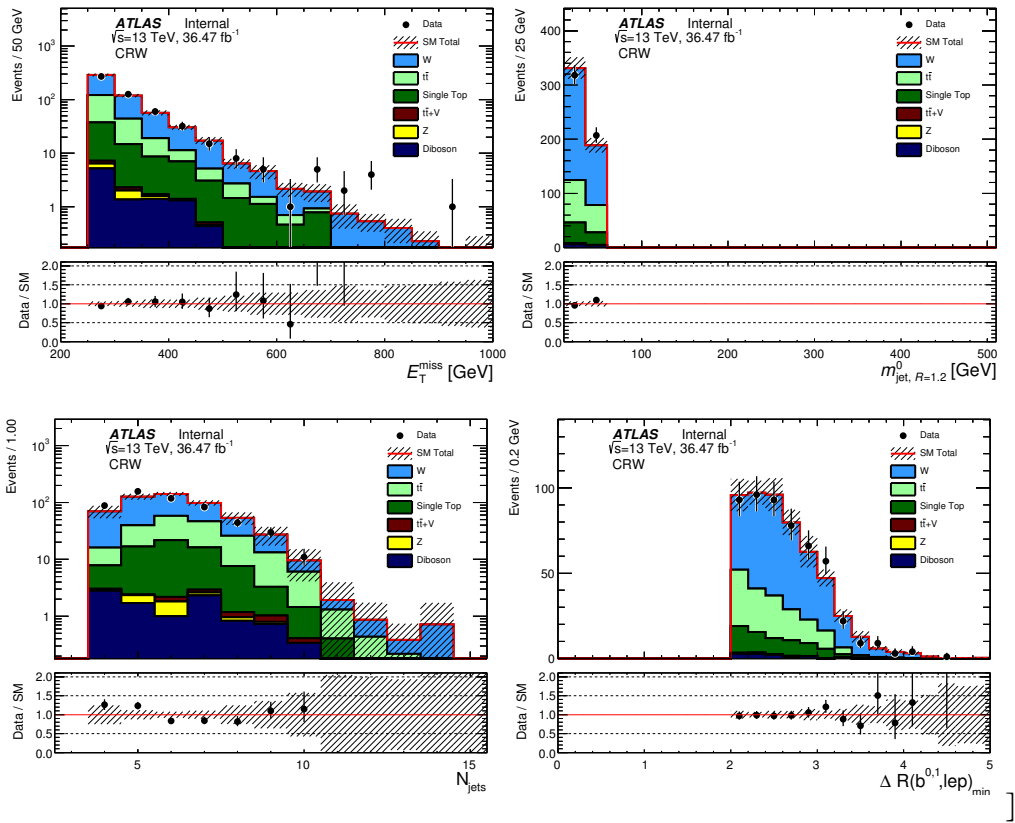


**Figure 12.5:** Postfit data/MC comparisons in the  $W + \text{jets}$  CR. From left to right and top to bottom, the variables shown are  $E_T^{\text{miss}}$ ,  $m_T(\ell, E_T^{\text{miss}})$ ,  $m_{\text{jet},R=1.2}^0$  and  $\Delta R(b_{o,I}, \ell)_{\text{min}}$ . The expected SM background has been normalized to data in the CR by performing a simultaneous fit to all background CR. The hatched band on the total SM background correspond to the total experimental systematic uncertainty plus the MC statistical uncertainty.

with a  $W$  decay. The  $\Delta R(b, b) > 1.5$ , the  $\Delta R$  between the two b-jets with the highest b-tagging

values, isolates single top events and reject ttbar background. This gives the single top CR a single

top purity of  $\sim 50\%$

The mass requirement on the large R jet  $m_{\text{jet},R=1.2}^0 > 120$  GeV searches for events with reconstructed boosted tops and ensures orthogonality with the  $W + \text{jets}$  CR. The  $\Delta R(b_{o,I}, \ell)_{\text{min}}$  selection ensures orthogonality with the ttbar CR.

**Table 12.6:** Selection for the 1-lepton, single top control region.

	CRST
Number of leptons	1
Number of jets (incl. lepton)	$\geq 4$
$p_T$ of jets (incl. lepton)	(80,80,40,40) GeV
$\min  \Delta\phi(\text{jet}^{o-1}, E_T^{\text{miss}}) $	$> 0.4$
$E_T^{\text{miss}}$	$> 250$ GeV
$m_T(\ell, E_T^{\text{miss}})$	$> 30, < 100$ GeV
Number of $b$ -jets	$\geq 2$
$m_{\text{jet}, R=1.2}^o$	$v > 120$ GeV
$m_T^{b,\text{min}}$	$> 200$ GeV
$\Delta R(b_{o,1}, \ell)_{\text{min}}$	$> 2.0$
$\Delta R(b, b)$	$> 1.5$

Data vs MC comparisons in the single control region are shown in histograms in figure 12.6. The expected MC background has been normalized to the amount of data in the single top control region by performing a simultaneous fit to all background CR. The hashed bands on the total SM background correspond to the amount of total experimental systematical uncertainty plus the MC statistical uncertainty. The yield in the single top CR is given in table 12.7.

Data and MC are compatible to within statistical uncertainty. No strong trends are observed in the data to MC ratios in any of the distribution.

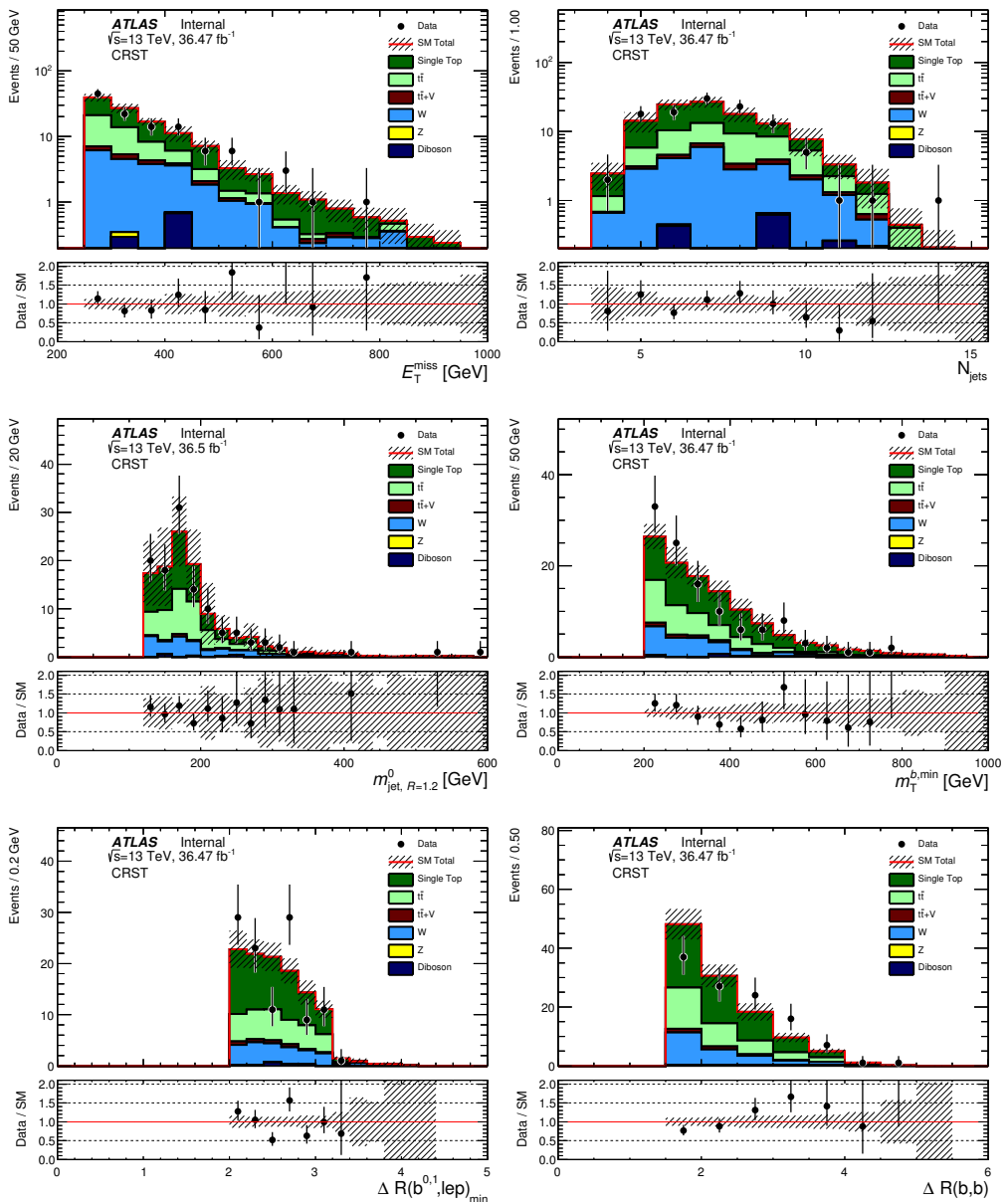


**Figure 12.6:** Single top control region distributions for  $36.47 \text{ fb}^{-1}$  of data after a simultaneous fit to all background CR. The ratio between data and MC is shown in the bottom panel. The hashed area on the expected SM background represent the uncertainty due to experimental systematics and MC statistics.

CRST (44% purity)	
Z	$0.11 \pm 0.05$
dibosons	$1.52 \pm 0.54$
ttbar	$34.17 \pm 2.10$
singleTop	$45.62 \pm 1.41$
ttV	$2.42 \pm 0.19$
W	$19.72 \pm 1.69$
Total MC	$103.57 \pm 3.10$
Data	$113.00 \pm 10.63$
SF	$1.21 \pm 0.29$

**Table 12.7:** Yields in the CRST in  $36.47 \text{ fb}^{-1}$  of data.

### 12.3.3 STANDARD MODEL $t\bar{t}+Z$

$t\bar{t}$  produced in conjunction with a  $Z$  boson consist of about 1 percent of the background in the SR.

Although the background is essentially negligible we do estimate the amount of  $t\bar{t} + Z$  using a  $t\bar{t} + \gamma$  CR.

Using the charged leptonic  $Z$  boson decays to design a CR to estimate the  $t\bar{t} + Z$  background would produce a CR with small systematic uncertainty. However, such CR tend to have low statistics because of the small branching fraction to electrons/muons compared to the branching fraction of neutrinos. A dilepton CR also contain a large contamination of  $t\bar{t}$  and  $Z + \text{jets}$  processes.

We take another data driven approach by building a one-lepton CR for  $t\bar{t} + \gamma$ .  $t\bar{t}\gamma$  mimics  $t\bar{t} + Z$  as the photon is in many ways like a lighter  $Z$ . The CR is designed to minimize theoretical uncertainties due to the extrapolation from the  $\gamma$  in CR to the  $Z$  in SR.

We require exactly one signal photon and one signal lepton. The lepton is not treated as a jet for the purpose of jet multiplicity and jet requirements unlike the  $t\bar{t}$ ,  $W + \text{jets}$  and single top CRs. We trigger on leptons instead of  $E_T^{\text{miss}}$  in this region with the triggers defined in table 12.8.

**Table 12.8:** Single Lepton triggers

Channel	Trigger
	Data 2015
Electron Muon	HLT_e24_lhmedium_L1EM20VH OR HLT_e60_lhmedium OR HLT_e120_lhloose HLT_mu20_iloose_L1MU15 OR HLT_mu50
	Data 2016
Electron Muon	HLT_e26_lhtight_nod0_ivarloose OR HLT_e60_lhmedium_nod0 OR HLT_e140_lhloose HLT_mu26_ivarmedium OR HLT_mu50

The highest  $p_T$  photon is required to have a  $p_T$  of at least  $> 150$  GeV. The high  $p_T$  gamma ensures that we are in a region of phase space where the  $\gamma p_T$  shape will mimic the heavier  $Z \rightarrow \nu\bar{\nu}$  decay. The true  $\gamma p_T$  and the  $Z p_T$  distributions without detector resolution effects is shown in figure 12.7 after a selection of reconstructed boson  $p_T > 150$  GeV has been applied for both samples.

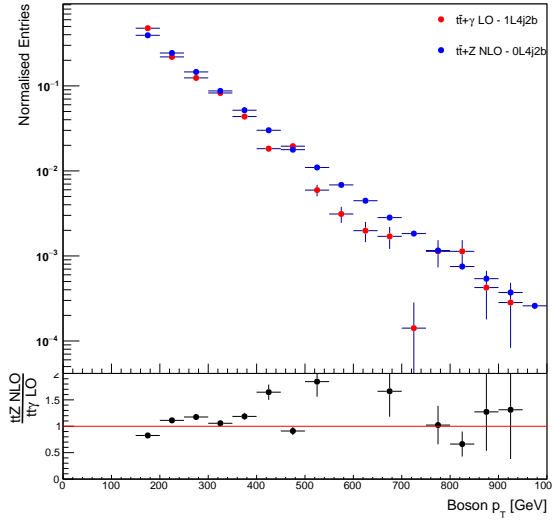


**Figure 12.7:** Truth  $p_T$  ratio.

The  $t\bar{t} + \gamma$  control region is given in table 12.9. The expected background and data yields in the  $t\bar{t} + \gamma$  CR is given in table 12.10.

Data vs MC comparisons in the  $t\bar{t} + \gamma$  control region are shown in histograms in figure 12.8. The expected MC background has been normalized to the amount of data in the  $t\bar{t} + \gamma$  control region by performing a simultaneous fit to all background CR. The hashed bands on the total SM background correspond to the amount of total experimental systematical uncertainty plus the MC statistical uncertainty.

**Table 12.9:** Selection for the  $t\bar{t} + \gamma$  1 lepton CR. The same triggers as described in Table 12.8 are used and the same signal lepton requirements are mad as in Tables ?? and ??

Selection	Requirement
Event selection	Event cleaning
Trigger	1L Triggers
Leptons	= 1
Lepton $p_T$	$\geq 28$ GeV
Photons	exactly 1
jet multiplicity	$\geq 4$
Jet $p_T$	(80,80,40,40) GeV
b-jet multiplicity	$\geq 2$
$\gamma p_T$	$> 150$ GeV

**Table 12.10:** Background composition of  $t\bar{t}\gamma$  CR.

CRTTGamma (87% purity)	
ttGamma	$112.20 \pm 1.49$
VGamma	$6.41 \pm 0.70$
Z	$0.73 \pm 0.21$
dibosons	$0.00 \pm 0.00$
ttbar	$4.57 \pm 1.23$
singleTop	$2.01 \pm 0.81$
ttV	$2.42 \pm 0.28$
W	$0.04 \pm 0.02$
Total MC	$128.38 \pm 2.23$
Data	$160.00 \pm 12.65$
SF	$1.28 \pm 0.12$

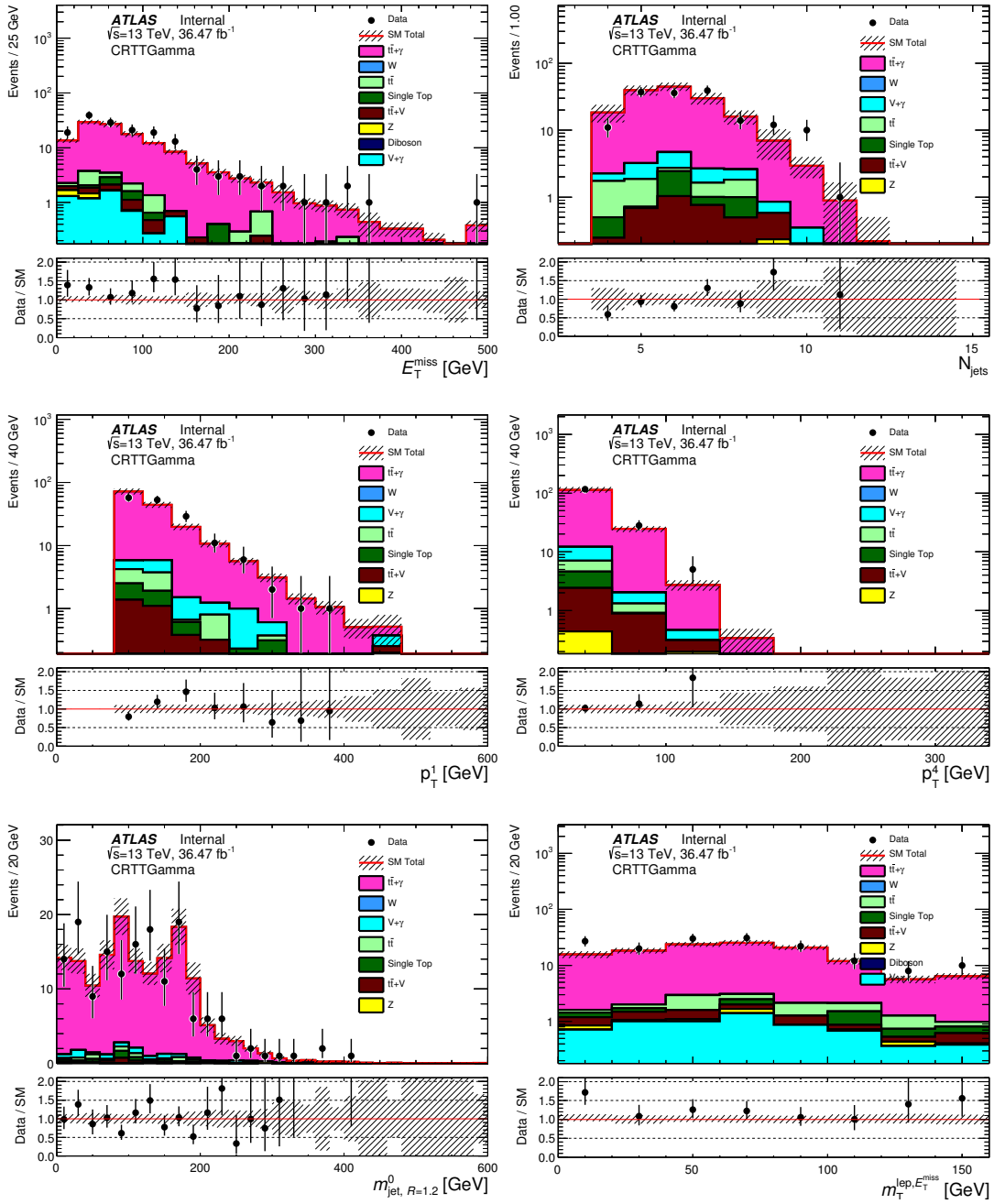


**Figure 12.8:** Prefit distributions of the  $E_T^{\text{miss}}$  and  $m_T(\ell, E_T^{\text{miss}})$  for fake lepton checks. Agreement at low  $m_T(\ell, E_T^{\text{miss}})$  is reasonable indicating no significant contributions from fake leptons. The ratio between data and MC is given in the bottom panel. The hashed area in both the top and lower panel represents the uncertainty due to MC statistics.

#### 12.3.4 STANDARD MODEL Z+JETS

Z+jets consist of 3 percent of all backgrounds in the SR. The percentage of Z+jets is higher in high  $R_{\text{ISR}}$  bins. The percentage Z+jets rises to 7 percent in  $R_{\text{ISR}}$  between 0.6 and 0.8. We use just the MC prediction for Z+jets because the rate of Z+jet is so low. We assign an 100 percent theory uncertainty to the Z+jets rate in the SR.

The ttbar validation region described in section 12.2.3 has a larger fraction of Z+jets event than those in the SR. The ttbar VR is kinematically similar to those of the SR with some loser cuts on jet multiplicity and ISR,  $E_T^{\text{miss}}$  correlations. The good agreement between data and MC in the ttbar VR is evidence that the Z+jets MC cannot be wrong by more than 100 percent.

#### 12.3.5 STANDARD MODEL DIBOSON

Standard Model dibosons consist of 1 percent of the background in the signal region. The diboson background consist of less then 2 percent of any single  $R_{\text{ISR}}$  bin in the SR. The background is negligible and we only use MC predictions for background estimation.

#### 12.3.6 STANDARD MODEL QCD MULTIJET AND ALL HADRONIC $t\bar{t}$

Both QCD multijet and all hadronic  $t\bar{t}$  creates little intrinsic  $E_T^{\text{miss}}$ . Instead misreconstructed jets can cause an imbalance in the total event  $E_t$  and generate fake  $E_T^{\text{miss}}$ . QCD contributions are only significant in the SR bins with low  $R_{\text{ISR}} < 0.4$  and are estimated using a data driven method called the jet smearing method.

## THE JET SMEARING METHOD

QCD multijet and all hadronic  $t\bar{t}$  background are estimated using the jet smearing method. The jet smearing method uses several steps to model the  $E_T^{\text{miss}}$  expected to result from mis-reconstructing jets.

First seed events with well reconstructed jets and little  $E_T^{\text{miss}}$  are first selected from data. Then, the seed event's jet momenta are repeatedly smeared with predetermined jet energy response. The resulting *pesudo-data* events with smeared jets can have potentially large  $E_T^{\text{miss}}$  due to misreconstructed jets. A schematic of the jet smearing method is shown in figure 12.9.

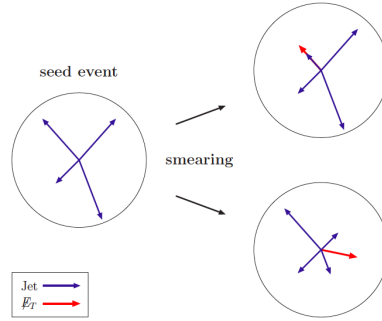


**Figure 12.9:** Schematic of the jet smearing method. A seed event with good jet energy measurements are repeatedly smeared with predetermined jet energy resolutions. The new  $E_T^{\text{miss}}$  is calculated as the difference between the seed event's and smeared event's jet momenta plus the original seed event's  $E_T^{\text{miss}}$ . (Figure taken from <sup>44</sup>)

Seed events are selected using the criteria in table ??.

Where the quantity  $E_T^{\text{miss}} \text{sig.} = \frac{E_T^{\text{miss}} - 8 \text{ GeV}}{\sum E_T}$  measures the general significant of the amount of  $E_T^{\text{miss}}$  relative to total hadronic activity in an event. In general events with low  $E_T^{\text{miss}} \text{sig.}$  have better reconstructed jets. However, the requirement on  $E_T^{\text{miss}} \text{sig.}$  depends on the number of b-jets due to

**Table 12.11:** Seed event preselection

Cut
$n_{\text{prim.vertices}} > 0$
Jet trigger
Bad jet veto
Cosmic muon veto
Bad muon veto
Baseline lepton veto
$\geq 4$ jets
$\geq 1$ $b$ -jets
$E_T^{\text{miss}} \text{sig.} < 0.3 + 0.1 \cdot n_{\text{n-bjets}}$

the possibility of  $b$ -quarks emitting a significant fraction of their energy in the form of neutrinos.

The jet response function include contributions from the following effects:

- Limited calorimeter granularity
- Hadronic energy falling outside of the jet radius or failed to be clustered correctly by jet reconstruction.
- Additional energy clustered into the jet that result from other sources.
- Energetic jet punching through the calorimeter.
- Dead material in the calorimeter.
- $b$ -quark generating real  $E_T^{\text{miss}}$  through decay to neutrinos.  $B$ -tagged jets have a different jet response function than light quark jets to account for this difference.

The jet smearing methods have a number of inherent assumptions about the generation of  $E_T^{\text{miss}}$  in QCD multijet and all hadronic  $t\bar{t}$  background. These assumptions include:

- The jet response captures all sources of jet pt measurement fluctuations
- The  $E_T^{\text{miss}}$  of multijet events are dominated by mis-measured jets

- Jet response are independent on the presence of other jet and jet smearing can be applied on a jet-by-jet basis

Other sources of  $E_T^{\text{miss}}$  not taken into account by the jet smearing method such as  $E_T^{\text{miss}}$  from pileup jets, mis-reconstructed soft term of the  $E_T^{\text{miss}}$  and object overlap removal are assumed to be negligible in the signal region.

### QCD MULTIJET CONTROL REGION AND VALIDATION REGION

The pseudo-data resulting from the jet smearing processes is then normalized to data using the QCD control region defined in table 12.12. The QCD CR is designed to be close to the SR except the min  $|\Delta\phi(\text{jet}^{o-1}, E_T^{\text{miss}})|$  is required to be low, between 0.05 to 0.1 instead of high  $> 0.04$ . This region is dominated by QCD backgrounds with high  $E_T^{\text{miss}}$  due to a single mis-reconstructed energetic jet but with the same jet multiplicity and jet kinematics required in the SR.

Data vs QCD pseudo-data prediction for the  $p_T^{\text{ISR}}$ ,  $\Delta\phi_{\text{ISR}, I}$  and  $M_T^S$  variables for the QCD CR can be seen in figure 12.10. These variables are shown because they are extrapolated over from CR to SR.

The results of QCD multijet prediction using jet smearing after normalizing to the CR can be checked in the QCD VR defined in table 12.13. The QCD VR has the exact same kinematic selection as the SR except with a lower min  $|\Delta\phi(\text{jet}^{o-1}, E_T^{\text{miss}})|$  between 0.1 and 0.2.  $R_{\text{ISR}}$  is also required to be below 0.4 but we don't expect a large QCD contribution at higher  $R_{\text{ISR}}$ .

Data vs QCD pseudo-data prediction for the  $R_{\text{ISR}}$  and  $\Delta\phi_{\text{ISR}, I}$  variables for the QCD VR can be seen in figure 12.10. A good agreement is found between data and pseudo-data predictions.

**Table 12.12:** QCD CR definitions, in addition to the 0 lepton preselection in Table ??.

Variable	CR
$\min  \Delta\phi(\text{jet}^{\text{o}-1}, E_{\text{T}}^{\text{miss}}) $	[0.05, 0.1]
$N_{\text{b-jet}}^{\text{s}}$	$\geq 1$
$N_{\text{jet}}^{\text{s}}$	$\geq 5$
$\hat{p}_{\text{T},b}^{\text{o,s}}$	$> 40 \text{ GeV}$
$\Delta\phi_{\text{ISR}, E_{\text{T}}^{\text{miss}}}$	$> 2.00$
$p_{\text{T}}^{\text{ISR}}$	$> 150 \text{ GeV}$
$R_{\text{ISR}}$	$< 0.4$
$\hat{p}_{\text{T}}^{4,\text{s}}$	$> 50 \text{ GeV}$
b-tagged jets	$\geq 1$

**Table 12.13:** QCD VR definitions, in addition to the 0 lepton preselection in Table ??.

Variable	VR
$\min  \Delta\phi(\text{jet}^{\text{o}-1}, E_{\text{T}}^{\text{miss}}) $	[0.1, 0.2]
$N_{\text{b-jet}}^{\text{s}}$	$\geq 1$
$N_{\text{jet}}^{\text{s}}$	$\geq 5$
$\hat{p}_{\text{T},b}^{\text{o,s}}$	$> 40 \text{ GeV}$
$m_{\text{s}}$	$> 300 \text{ GeV}$
$\Delta\phi_{\text{ISR}, E_{\text{T}}^{\text{miss}}}$	$> 3.00$
$p_{\text{T}}^{\text{ISR}}$	$> 400 \text{ GeV}$
$R_{\text{ISR}}$	$< 0.4$
$\hat{p}_{\text{T}}^{4,\text{s}}$	$> 50 \text{ GeV}$
b-tagged jets	$\geq 1$

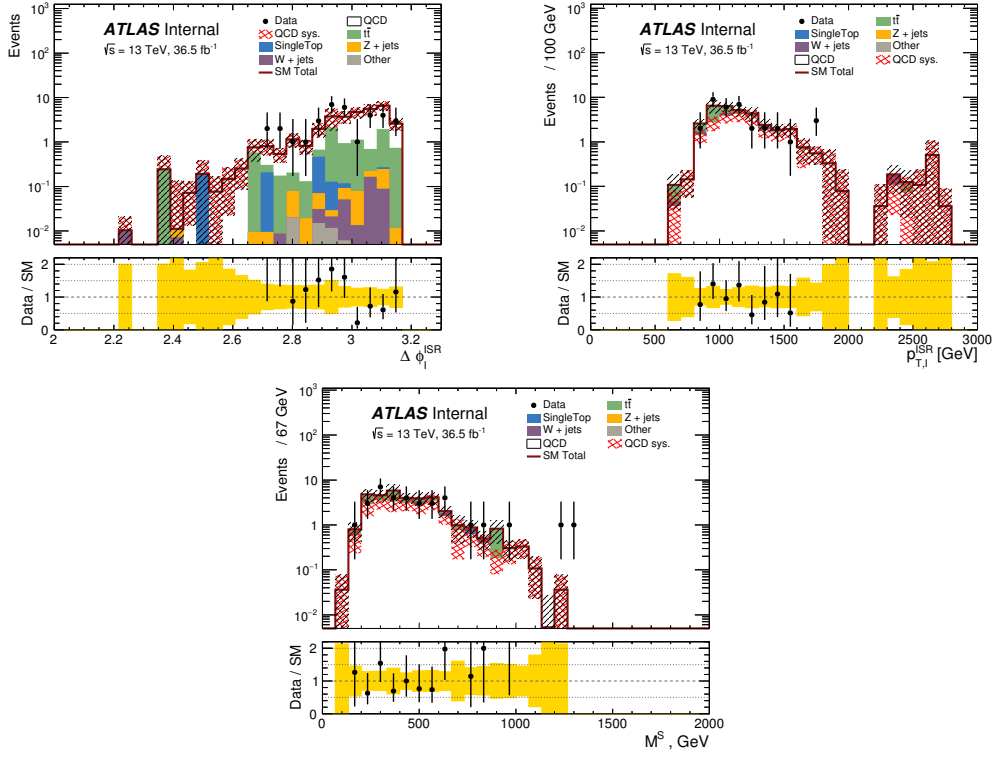


**Figure 12.10:**  $p_T^{\text{ISR}}, \Delta\phi_{\text{ISR},I}$  and  $M^S$  distributions in the QCD control regions.

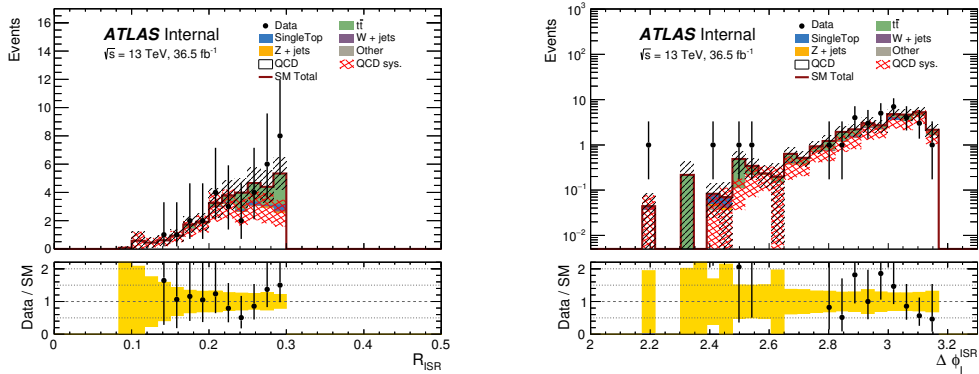


**Figure 12.11:**  $R_{\text{ISR}}$  and  $\Delta\phi_{\text{ISR},I}$  distributions in the QCD validation regions.

## QCD PREDICTION IN THE SIGNAL REGION

The predicted amount of QCD in the signal region is given by the amount of QCD pseudo-data that survive the signal region selection after normalization to the QCD CR. The systematic uncertainty on the SR QCD prediction is given by repeating the process with a tighter and looser set of seed event selections. An upward error correspond to seed events requiring  $E_T^{\text{miss}} \text{sig.} < 0.6 + 0.2 \cdot n_{\text{n-bjets}}$  and a lower error corresponds to seed events requiring  $E_T^{\text{miss}} \text{sig.} < 0.2 + 0.05 \cdot n_{\text{n-bjets}}$ .

The expected QCD yield and uncertainty in the SR is given in table ??

**Table 12.14:** Expected yields of the QCD multijet backgrounds in SR.

$R_{\text{ISR}}$ Region	0.3-0.4	0.4-0.5	0.5-0.6	0.6-0.7	0.7-0.8
QCD expected yield	$4.56 \pm 2.38$	$1.58 \pm 0.77$	$0.32 \pm 0.17$	$0.04 \pm 0.02$	$0.00 \pm 0.00$

# 13

## Systematic Uncertainties

Systematic uncertainties can be categorized into two separate categories, experimental uncertainties and theoretical uncertainties. Experimental systematics result from uncertainties in physics object reconstruction, calibration and understanding the detectors. Theoretical systematics result from uncertainties in theoretical calculations. The same experimental uncertainty is assumed to be 100% correlated across different background sources. Theoretical uncertainties are assumed to be uncorre-

lated from one another.

In general systematic uncertainty are parameterized as independent nuisance parameters with gaussian constraints. The systematic on backgrounds are evaluated through a simultaneous fit to CR and SR. An estimate of the amount of systematic uncertainties on backgrounds in SR can be done by fitting the CR alone and extrapolating the result to the SR. If the background prediction fluctuate in the same way in the CR and SR the total systematic in SR would be partially canceled out in the transfer factor. This is why designing a CR that is kinematically similar to the SR is crucial to mitigating systematic uncertainties. More detail on CR design and systematics can be found in chapter 12.1 on background estimation and chapter 14 on statistics analysis.

Total background systematics is around 20% in the SR. The dominate background systematic uncertainty in the region between  $0.3 < R_{\text{ISR}} < 0.7$  is uncertainty on the jet energy scale, uncertainty on the ttbar ISR/FSR, and uncertainty on the ttbar matrix element and parton shower calculation with each attributing roughly 10% to the total systematic uncertainty. The theoretical uncertainty on the amount of interference between SM ttbar and single top at NLO is also significant. The large systematic uncertainty in the  $R_{\text{ISR}}$  bin between 0.7 – 0.8 is completely due to MC statistics caused by the low expected yield. However the 0.7 – 0.8  $R_{\text{ISR}}$  region is completely statistically dominated for the same reason, expecting only 0.7 background events.

The background uncertainty in each SR  $R_{\text{ISR}}$  region ordered by size of the systematic is given in table 13.1 and 13.2.

The fit may compensate for a change in one systematic by varying several other systematics in order to get the best fit in CR. This can lead to correlations between systematics that are initially

Uncertainty of channel	SRC <sub>1</sub>	SRC <sub>2</sub>	SRC <sub>3</sub>
Total background expectation	20.56	27.54	18.86
Total statistical ( $\sqrt{N_{\text{exp}}}$ )	$\pm 4.53$	$\pm 5.25$	$\pm 4.34$
Total background systematic	$\pm 6.62 [32.18\%]$	$\pm 4.89 [17.75\%]$	$\pm 3.53 [18.72\%]$
alpha_ttbarGenPS	$\pm 4.86 [23.6\%]$	$\pm 1.91 [6.9\%]$	$\pm 2.39 [12.7\%]$
alpha_RadLoHi	$\pm 2.64 [12.8\%]$	$\pm 2.19 [8.0\%]$	$\pm 1.06 [5.6\%]$
alpha_JetSmearing	$\pm 2.38 [11.6\%]$	$\pm 0.77 [2.8\%]$	$\pm 0.17 [0.91\%]$
alpha_theoSysSingleTop	$\pm 1.66 [8.1\%]$	$\pm 1.18 [4.3\%]$	$\pm 1.21 [6.4\%]$
gamma_stat_SRC <sub>1</sub> _cuts_bin_o	$\pm 1.29 [6.3\%]$	$\pm 0.00 [0.00\%]$	$\pm 0.00 [0.00\%]$
mu_ttbarC	$\pm 0.91 [4.4\%]$	$\pm 1.55 [5.6\%]$	$\pm 1.03 [5.4\%]$
alpha_JER	$\pm 0.81 [3.9\%]$	$\pm 2.70 [9.8\%]$	$\pm 1.14 [6.0\%]$
alpha_JET_GroupedNP_3	$\pm 0.72 [3.5\%]$	$\pm 0.03 [0.10\%]$	$\pm 0.17 [0.89\%]$
mu_SingleTop	$\pm 0.56 [2.7\%]$	$\pm 0.40 [1.4\%]$	$\pm 0.41 [2.2\%]$
alpha_MET_SoftTrk_ResoPerp	$\pm 0.46 [2.3\%]$	$\pm 0.56 [2.0\%]$	$\pm 0.22 [1.2\%]$
alpha_cEff	$\pm 0.43 [2.1\%]$	$\pm 0.40 [1.5\%]$	$\pm 0.11 [0.60\%]$
alpha_JET_GroupedNP_2	$\pm 0.30 [1.5\%]$	$\pm 0.78 [2.8\%]$	$\pm 0.36 [1.9\%]$
alpha_JET_GroupedNP_1	$\pm 0.27 [1.3\%]$	$\pm 0.06 [0.23\%]$	$\pm 0.04 [0.19\%]$
alpha_MET_SoftTrk_Scale	$\pm 0.23 [1.1\%]$	$\pm 0.29 [1.0\%]$	$\pm 0.08 [0.45\%]$
alpha_theoSysDiboson	$\pm 0.19 [0.94\%]$	$\pm 0.10 [0.37\%]$	$\pm 0.14 [0.76\%]$
alpha_CExtrap	$\pm 0.16 [0.80\%]$	$\pm 0.31 [1.1\%]$	$\pm 0.19 [1.0\%]$
alpha_LightEff	$\pm 0.15 [0.74\%]$	$\pm 0.22 [0.80\%]$	$\pm 0.04 [0.23\%]$
alpha_bEff	$\pm 0.14 [0.70\%]$	$\pm 0.00 [0.01\%]$	$\pm 0.07 [0.36\%]$
alpha_JET_EtaNonClosure	$\pm 0.11 [0.54\%]$	$\pm 1.13 [4.1\%]$	$\pm 0.01 [0.03\%]$
mu_Wjets	$\pm 0.09 [0.45\%]$	$\pm 0.22 [0.81\%]$	$\pm 0.22 [1.2\%]$
alpha_theoSysW	$\pm 0.09 [0.45\%]$	$\pm 0.24 [0.88\%]$	$\pm 0.23 [1.2\%]$
alpha_MET_SoftTrk_ResoPara	$\pm 0.07 [0.35\%]$	$\pm 0.19 [0.68\%]$	$\pm 0.03 [0.15\%]$
mu_TtbarV	$\pm 0.05 [0.22\%]$	$\pm 0.09 [0.34\%]$	$\pm 0.09 [0.47\%]$
alpha_PILEUP	$\pm 0.02 [0.11\%]$	$\pm 0.32 [1.2\%]$	$\pm 0.12 [0.64\%]$
alpha_FTEtrap	$\pm 0.02 [0.11\%]$	$\pm 0.04 [0.13\%]$	$\pm 0.03 [0.17\%]$
alpha_theoSysTTbarV	$\pm 0.01 [0.07\%]$	$\pm 0.03 [0.11\%]$	$\pm 0.03 [0.15\%]$
alpha_JVT	$\pm 0.01 [0.06\%]$	$\pm 0.04 [0.13\%]$	$\pm 0.04 [0.22\%]$
gamma_stat_SRC <sub>2</sub> _cuts_bin_o	$\pm 0.00 [0.00\%]$	$\pm 1.42 [5.1\%]$	$\pm 0.00 [0.00\%]$
gamma_stat_SRC <sub>3</sub> _cuts_bin_o	$\pm 0.00 [0.00\%]$	$\pm 0.00 [0.00\%]$	$\pm 0.96 [5.1\%]$

**Table 13.1:** Breakdown of the dominant systematic uncertainties on background estimates. Note that the individual uncertainties can be correlated, and do not necessarily add up quadratically to the total background uncertainty. The percentages show the size of the uncertainty relative to the total expected background.

Uncertainty of channel	SRC4	SRC5
Total background expectation	7.69	0.90
Total statistical ( $\sqrt{N_{\text{exp}}}$ )	$\pm 2.77$	$\pm 0.95$
Total background systematic	$\pm 1.37$ [17.77%]	$\pm 0.71$ [78.68%]
alpha_theoSysSingleTop	$\pm 0.71$ [9.3%]	$\pm 0.00$ [0.00%]
alpha_ttbarGenPS	$\pm 0.68$ [8.8%]	$\pm 0.63$ [69.1%]
gamma_stat_SRC4_cuts_bin_o	$\pm 0.54$ [7.0%]	$\pm 0.00$ [0.00%]
alpha_RadLoHi	$\pm 0.46$ [6.0%]	$\pm 0.13$ [14.8%]
alpha_JER	$\pm 0.35$ [4.6%]	$\pm 0.09$ [9.7%]
mu_ttbarC	$\pm 0.35$ [4.5%]	$\pm 0.04$ [4.9%]
mu_SingleTop	$\pm 0.24$ [3.1%]	$\pm 0.00$ [0.00%]
mu_Wjets	$\pm 0.22$ [2.9%]	$\pm 0.02$ [2.7%]
alpha_theoSysW	$\pm 0.21$ [2.7%]	$\pm 0.02$ [2.3%]
alpha_JET_GroupedNP_1	$\pm 0.18$ [2.3%]	$\pm 0.04$ [4.2%]
alpha_PILEUP	$\pm 0.15$ [2.0%]	$\pm 0.13$ [13.9%]
alpha_MET_SoftTrk_ResoPerp	$\pm 0.14$ [1.9%]	$\pm 0.01$ [1.6%]
alpha_MET_SoftTrk_ResoPara	$\pm 0.13$ [1.7%]	$\pm 0.00$ [0.12%]
alpha_LightEff	$\pm 0.12$ [1.6%]	$\pm 0.02$ [1.9%]
alpha_bEff	$\pm 0.08$ [1.0%]	$\pm 0.01$ [1.4%]
alpha_cEff	$\pm 0.07$ [0.93%]	$\pm 0.03$ [3.2%]
alpha_JET_EtaNonClosure	$\pm 0.07$ [0.87%]	$\pm 0.11$ [12.4%]
alpha_JET_GroupedNP_3	$\pm 0.06$ [0.72%]	$\pm 0.02$ [2.5%]
alpha_JVT	$\pm 0.02$ [0.29%]	$\pm 0.00$ [0.35%]
alpha_JetSmearing	$\pm 0.02$ [0.26%]	$\pm 0.00$ [0.15%]
alpha_CExtrap	$\pm 0.02$ [0.23%]	$\pm 0.00$ [0.22%]
mu_TtbarV	$\pm 0.01$ [0.17%]	$\pm 0.01$ [1.1%]
alpha_JET_GroupedNP_2	$\pm 0.01$ [0.15%]	$\pm 0.09$ [10.3%]
alpha_FTEtrap	$\pm 0.01$ [0.10%]	$\pm 0.00$ [0.17%]
alpha_MET_SoftTrk_Scale	$\pm 0.01$ [0.07%]	$\pm 0.00$ [0.11%]
gamma_stat_SRC5_cuts_bin_o	$\pm 0.00$ [0.00%]	$\pm 0.21$ [23.0%]

**Table 13.2:** Breakdown of the dominant systematic uncertainties on background estimates. Note that the individual uncertainties can be correlated, and do not necessarily add up quadratically to the total background uncertainty. The percentages show the size of the uncertainty relative to the total expected background.

parameterized as independent nuisance parameters before the fit to CR. The correlation matrix between a reduced set of systematic variations and background scale factor after the simultaneous fit to all CRs are given in figure 13.1. The scale factor  $\mu$  is the amount that the expected background MC must be scaled up/down by so that data and MC yields agree in the CR.

The post-fit pull is given in figure 13.2. No profiling of any systematics is observed.

A summary of the experimental and theoretical uncertainties relevant to this analysis is given in the sections below.

### 13.0.1 EXPERIMENTAL UNCERTAINTIES

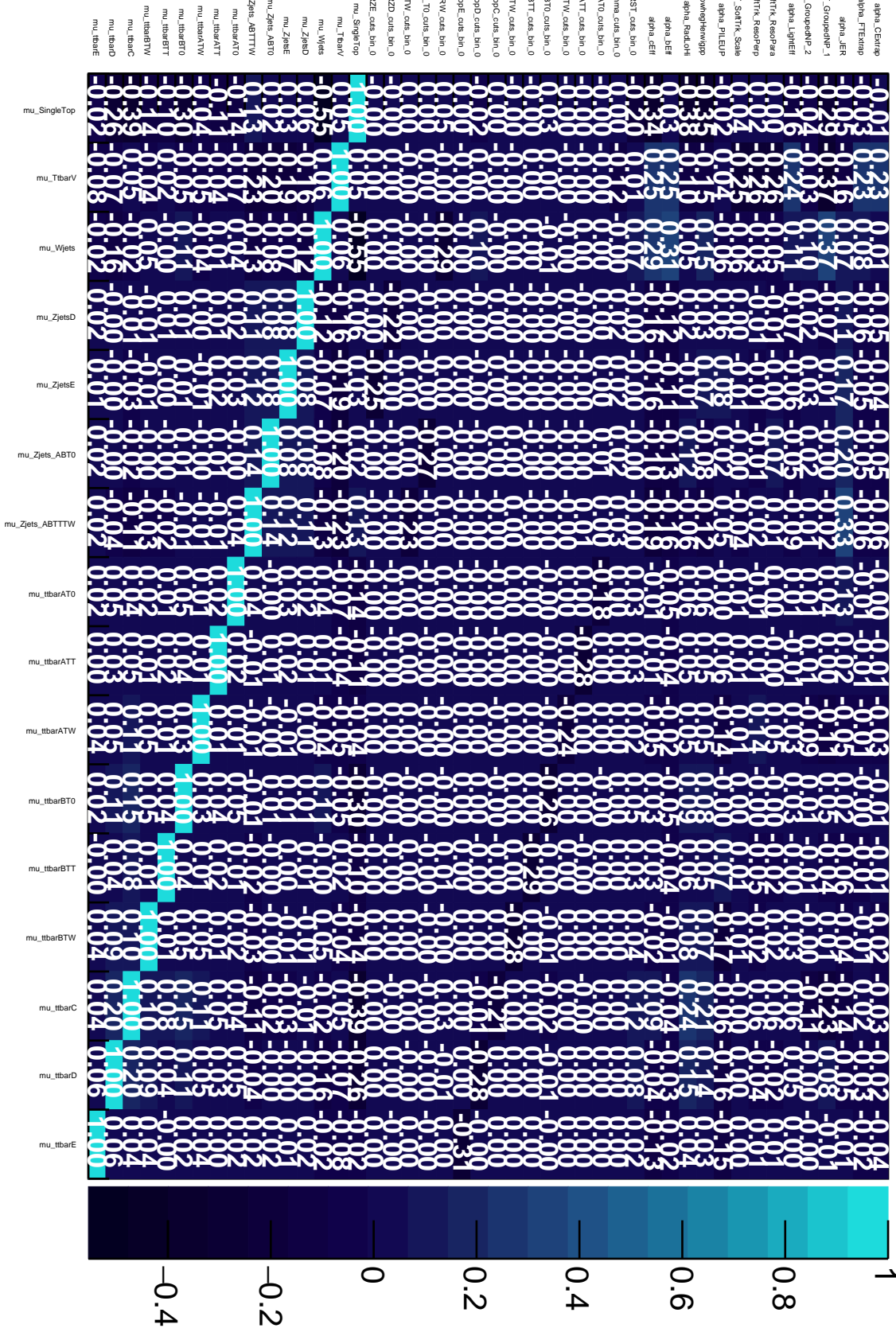
Experimental systematics are estimated using a simultaneous fit of CR and the results extrapolated to the SR in a background only fit. Variations on background yield and kinematics are determined for each systematic by different object performance groups using a number of simulation based and in-situ techniques. These are variations correspond to the  $+1$  or  $-1$  sigma fluctuation on the gaussian constraint for the systematic. A simultaneous fit to the CR gives both the background scale factor  $\mu$ , the best fit value of the systematic parameter  $\alpha$ , and the systematic uncertainty associated with the background prediction in the SR.

### UNCERTAINTIES ON THE JET ENERGY SCALE (JES) AND JET ENERGY RESOLUTION (JER)

The two main uncertainties affecting jet measurements are the uncertainties in JES and JER calibrations. The jet reconstruction and calibration process is described in section 3.3. Uncertainty in the calibration process leads to uncertainty in the calorimeter response to the true jet energy.

Figure 13.1: Correlation matrix between select nuisance parameters.

## Reduced correlation matrix



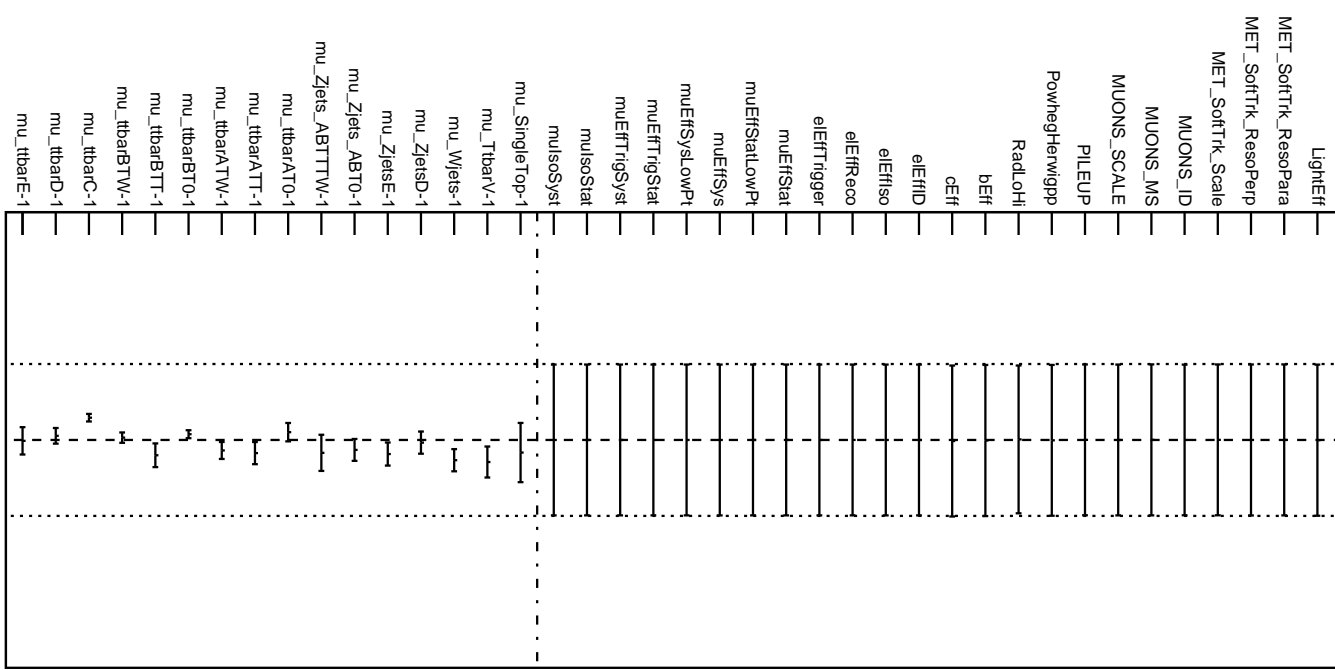
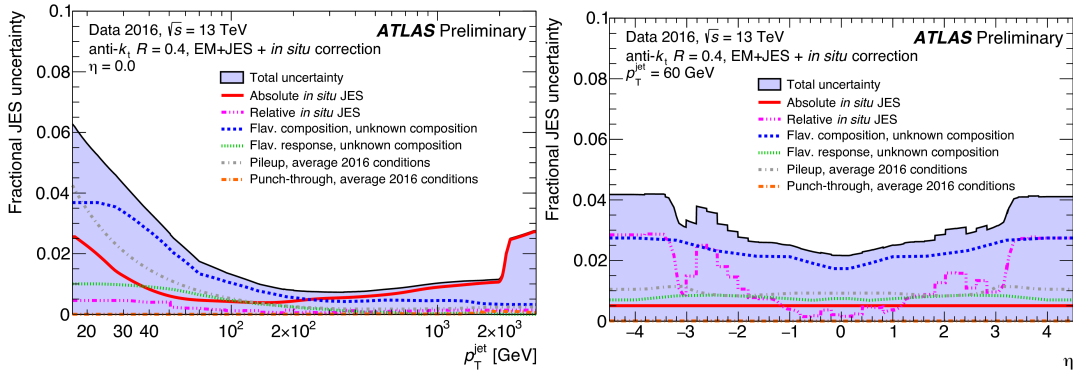


Figure 13.2: Post-fit pull plot for the background-only fit.

Since the dominant background, SM ttbar, uses a ttbar control region that requires very similar jet kinematics to the SR, Much of the JES and JER uncertainty is canceled out in the transfer factor between the two. The JES uncertainty still accounts for one of the major systematic background in the SR at around 10% in every bin. Some of this results from extrapolation between the iL CR and oL SR where a lepton is effectively replaced with a hadronic tau jet using simulation.

Uncertainties on the JES are derived from different in-situ techniques by the ATLAS Jet/ $E_T^{\text{miss}}$  group. These techniques exploit the transverse momentum balance between a jet and a reference object such as a photon or a Z boson or between multiple jets in multijet events.<sup>7,6</sup>. The uncertainty on JES depends on  $\eta$  and  $p_T$  of the jet. Uncertainties related to jet flavor composition and pile-up are also included.

The fractional JES uncertainty vs  $\eta$  and  $p_T$  for 2016 data can be seen in figure 13.4.



**Figure 13.3:** Fractional uncertainty on the jet energy scale (JES) vs jet  $\eta$  and jet  $p_T$ .

Uncertainties on the JER are derived from dijet balance techniques.<sup>6</sup> The fractional uncertainty on JER vs  $\eta$  and  $p_T$  can be seen in figure ??

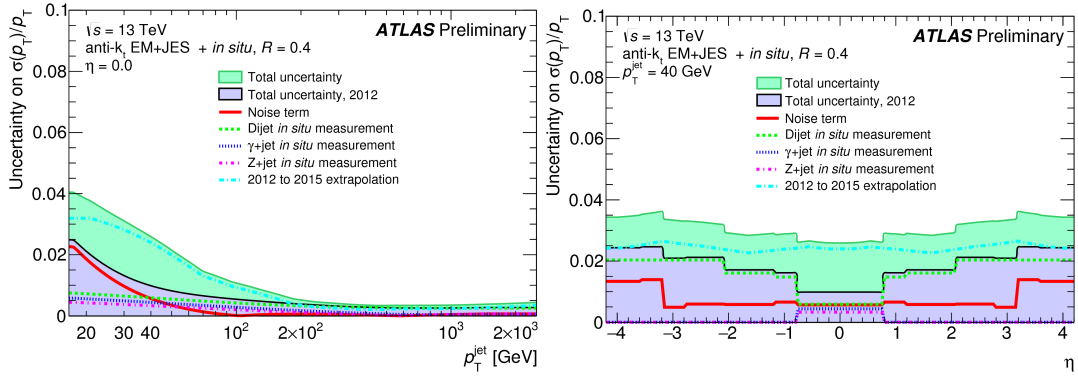


**Figure 13.4:** Fractional uncertainty on the jet energy resolution (JER) vs jet  $\eta$  and jet  $p_T$ .

## UNCERTAINTY ON $b$ -TAGGING

Uncertainties on  $b$ -tagging are no a large contribution to our systematics due to the fact that we require only a single b-tagged jet and high b-jet  $p_T$  requirement of 40 GeV. The dominant background ttbar and sub-dominate backgrounds  $W+jets$  and QCD multijets all use CRs that also require i  $b$ -tagged jet.  $b$ -tagging uncertainty contribute only 1-3% uncertainty to the total background yield in the SR because of both of these factors.

The  $b$ -tagging uncertainty is derived by the ATLAS flavor-tagging working group. A separate set of weights are applied for each set of  $b$ -tagging variations. These include scale factors on  $b$ -tagging efficiencies and the rate of mis-tagging of  $c$ -jets and light-flavored jets.

## UNCERTAINTY ON THE $E_T^{\text{miss}}$ SOFT TERM

Because the  $E_T^{\text{miss}}$  is built out of fully calibrated and reconstructed physics objects, the majority of the uncertainty on  $E_T^{\text{miss}}$  has already been accounted for by jet and lepton momenta and energy un-

certainties. However, the soft term of the  $E_T^{\text{miss}}$  is the one part of  $E_T^{\text{miss}}$  reconstruction that does not come from any hard physics object. The uncertainty on the  $E_T^{\text{miss}}$  soft term must be estimated independently.

The uncertainty on the resolution and scale of the  $E_T^{\text{miss}}$  soft term is derived by the ATLAS Jet/ $E_T^{\text{miss}}$  group using two in-situ methods using  $Z \rightarrow \mu\mu$  events. The uncertainty on the  $E_T^{\text{miss}}$  track soft term (TST) vs the number of reconstructed primary vertexes in  $t\bar{t}$  simulation is shown in figure 13.5.

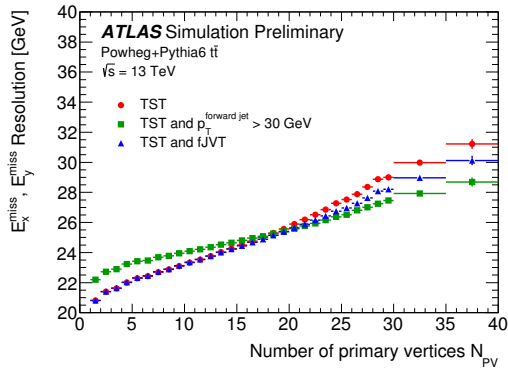


Figure 13.5: Uncertainty on the  $E_T^{\text{miss}}$  track soft term (TST) vs the number of reconstructed vertexes.

The  $E_T^{\text{miss}}$  soft term resolution and scale uncertainty contribute a 1 – 2% uncertainty on the total background yield. The small uncertainty result from the high required  $E_T^{\text{miss}}$  of at least 250 GeV and little to no extrapolation across  $E_T^{\text{miss}}$  between CR and SR for all major backgrounds.

## UNCERTAINTY ON LEPTON RECONSTRUCTION EFFICIENCIES AND ENERGY SCALE

Uncertainty on lepton reconstruction and identification propagate to uncertainty on CR and SR yields. These uncertainties include uncertainties on e/ $\gamma$  resolution, energy scale, and reconstruction

efficiency and muon momenta and reconstruction efficiency. Lepton trigger scale factors are taken into account for the  $t\bar{t} + \gamma$  control region.

These uncertainties are derived by the ATLAS E/ $\gamma$  and muon combined performance groups and result in sub 1% uncertainty on signal region yields.

## PILEUP

The uncertainty on the amount of pileup in 2015 and 2016 ATLAS data is estimated using a two sided variation in event weights. Pile-up uncertainty contributes a 1-2% uncertainty on the total background yield in the SR.

### 13.0.2 THEORETICAL UNCERTAINTIES

Theoretical uncertainties quantify the uncertainty associated with MC event generation including calculations on the matrix element, parton shower, and different input parameters such as  $\alpha_s$ , and others. As the background is ultimately normalized to the CR, only difference is the transfer factor (defined in equation ??) will result in a different SR background yield. We vary MC generation with respect to the default setting and determine the corresponding variation in the transfer factor as according to equation 13.1.

$$\Delta_X = \frac{T_f^{\text{up}} - T_f^{\text{down}}}{T_f^{\text{up}} + T_f^{\text{down}}} \quad (13.1)$$

All theoretical uncertainties for different backgrounds are assumed to be independent of one another.

## $t\bar{t}$ THEORETICAL UNCERTAINTY

Theoretical uncertainties on ttbar production include uncertainties on the hard scattering matrix element (ME) calculation, uncertainties on the parton shower (PS), and uncertainty on the amount of ISR/FSR produced in association with ttbar.

The ttbar ISR/FSR uncertainty is estimated by performing the analysis on fully reconstructed simulation with variations on the PS tuning and ME+PS matching scales that induces more/less ISR and FSR to be emitted in the simulation. The uncertainty on the ME calculation and on the PS calculation is estimated by performing the analysis on truth level-simulation using different MC generator programs without detector resolution effects. In other words, the ISR/FSR uncertainty determines how much the ttbar yields in SR differ if different *PowHeg* and *PYTHIA* settings were used. The ttbar hard scattering and PS variations determines how much the ttbar yields in SR differ if a different generator other than *PowHegPYTHIA* is used.

Uncertainties on the ME and PS are estimated by comparing the nominal *PowHegPYTHIA* ttbar sample with *PowHegHERWIG++* ttbar and *SHERPA 2.2.1* ttbar samples. The *PowHegHERWIG++* sample do not vary the ME calculation with respect to the nominal sample but does perform a different set of PS calculation with a distinct PS tune. The *SHERPA 2.2.1* ttbar sample perform a different ME and PS calculation with a different PDF set and PS tune. More details on the different ttbar MC generation can be found in section 6.2.

We take an envelope of the *SHERPA* and *PowHegHERWIG++* variations as the combined ttbar hard scattering and PS uncertainty. This is because the *PowHegHERWIG++* and *SHERPA* samples both vary the PS and avoids double counting of the PS uncertainty. The total hard scattering plus PS uncertainty is defined as the maximum of equation 13.2 and ??.

$$\Delta_{\text{hard scatter}} = \frac{T_f^{\text{PowHeg}} - T_f^{\text{SHERPA}}}{T_f^{\text{SHERPA}}} \quad (13.2)$$

$$\Delta_{\text{PS}} = \frac{T_f^{\text{PYTHIA}} - T_f^{\text{HERWIG++}}}{T_f^{\text{PYTHIA}}} \quad (13.3)$$

The ttbar ISR uncertainty is estimated by using the radHi and radLo *PowHegPYTHIA* samples. These samples are produced with different renormalization and factorization scales compared to the nominal sample (x0.5 to radHi and x2 to radLo). The radHi sample also increase the  $b_{damp}$  parameter that help control the matching between PS and ME from the nominal  $m_{top}$  to x2  $m_{top}$ . In general, the radHi (radLo) sample generates a higher (lower) differential cross-section for ttbar that is produced in conjunction with strong ISR than the nominal.

The raw pre-fit  $t\bar{t}$  yields in CR, VR and SR for the different ttbar samples and the ttbar theory uncertainty derived from transfer factor is given in table 13.3

	$t\bar{t}$ CR	SRC <sub>1</sub>	SRC <sub>2</sub>	SRC <sub>3</sub>	SRC <sub>4</sub>	SRC <sub>5</sub>	$t\bar{t}$ VR
ttbar	$668 \pm 9$	$16.7 \pm 1.6$	$31.7 \pm 2.1$	$21.7 \pm 1.6$	$6.3 \pm 0.8$	$0.60 \pm 0.23$	$232 \pm 5$
ttbar (rad up)	$872 \pm 11$	$25.2 \pm 2.3$	$39.5 \pm 2.3$	$28.7 \pm 2.1$	$8.6 \pm 1.0$	$1.05 \pm 0.33$	$293 \pm 7$
ttbar (rad down)	$521 \pm 9$	$10.1 \pm 1.0$	$19.2 \pm 1.6$	$15.8 \pm 1.5$	$6.3 \pm 1.2$	$0.7 \pm 0.4$	$187 \pm 5$
ttbar (Powheg+H++)	$621 \pm 10$	$16.3 \pm 1.8$	$27.8 \pm 1.8$	$18.0 \pm 1.5$	$6.5 \pm 0.9$	$0.46 \pm 0.18$	$206 \pm 5$
ttbar (Sherpa)	$840 \pm 40$	$30 \pm 8$	$42 \pm 9$	$22 \pm 5$	$7.4 \pm 3.2$	$< 0.01$	$297 \pm 30$
Transfer factors (in %)							
ISR/FSR		20	10	4	10	5	3.3
PS		5	6	11	11	20	4
Generator (Sherpa)		40	5	19	10	100	2

**Table 13.3:** Expected yields for different ttbar samples and theory uncertainties based on transfer factor for the  $t\bar{t}$  background for the SR, ttbar CR and VR.

### $W + \text{jets}$ THEORETICAL UNCERTAINTY

The *SHERPA* generator is used to estimate  $W + \text{jets}$  theory uncertainties. Different scale variations and seven LHE<sub>3</sub> variations are included to model the variations in *SHERPA* parton shower and ME calculations.

The theory uncertainty on  $W + \text{jets}$  production obtained from transfer factors is given in table 13.4. Values are given as percent uncertainty on  $W + \text{jets}$  yields in the SR.

### SINGLE TOP THEORETICAL UNCERTAINTY

Single top theoretical uncertainty include uncertainty on the PS, ISR/FSR, and the interference between ttbar and single top in the  $Wt$  channel. Single top uncertainties is evaluated on the  $Wt$  subprocess because the  $Wt$  subprocess dominates the single top background in signal region.

The single top parton shower uncertainty is modeled by comparing the nominal *PowHeqPYTHIA* sample with a *PowHeqHERWIG* + + single top sample in a similar fashion to the  $t\bar{t}$  PS uncertainty.

SR	uncertainty (%)
SRA-TT	9.5
SRA-TW	8.0
SRA-To	6.1
SRB-TT	9.1
SRB-TW	7.9
SRB-To	3.3
SRC <sub>1</sub>	11.4
SRC <sub>2</sub>	12.5
SRC <sub>3</sub>	11.8
SRC <sub>4</sub>	10.7
SRC <sub>5</sub>	9.5
SRC <sub>6</sub>	11.3
SRD-low	8.8
SRD-high	8.2
SRE	9.5
VRW	1.9

**Table 13.4:** Summary of the theory uncertainties (in percent) on  $W$  production obtained using variations on transfer factors.

The single top ISR/FSR uncertainty is also modeled by comparing the radHi and radLo *PowHegPYTHIA* single top samples to the nominal *PowHegPYTHIA* samples analogous to the  $t\bar{t}$  ISR/FSR uncertainty.

The single top interference uncertainty refer to the fact that at NLO the calculation of the  $pp \rightarrow Wt$  process will include contributions from  $pp \rightarrow t\bar{t} \rightarrow t + b + W$  which is already modeled in the SM ttbar MC. We can subtract out the ttbar contribution at either the level of amplitude (DR scheme) or at the level of matrix elements (DS scheme). Subtracting at the matrix element level also remove any potential interference between the single top  $pp \rightarrow Wt$  and ttbar  $pp \rightarrow t\bar{t} \rightarrow t + b + W$  processes. Subtracting at the amplitude level does not remove those interferences.

There is an uncertainty on the correct procedure to treat ttbar and single top interference as both

DR and DS schemes violates formal gauge invariance. We estimate this uncertainty by comparing the DR and DS schemes.

At the moment we take an 100% interference uncertainty because of the low MC statistics in DS scheme.

The raw pre-fit single top yields in SR, single top CR and VR for the different single top samples and the single top theory uncertainty derived from transfer factor is given in table 13.5.

	CRST	SRC <sub>1</sub>	SRC <sub>2</sub>	SRC <sub>3</sub>	SRC <sub>4</sub>	SRC <sub>5</sub>	VRT
st Wt (MET <sub>200</sub> )	41.7 ± 1.1	0.66 ± 0.14	1.14 ± 0.18	0.99 ± 0.17	0.39 ± 0.11	0.12 ± 0.06	19.9 ± 1.1
st Wt (radHi, MET <sub>200</sub> )	50.4 ± 1.3	0.60 ± 0.14	1.26 ± 0.20	1.33 ± 0.21	0.57 ± 0.14	0.25 ± 0.09	21.9 ± 1.3
st Wt (radLo, MET <sub>200</sub> )	34.9 ± 1.0	0.57 ± 0.13	0.77 ± 0.15	0.77 ± 0.15	0.37 ± 0.10	0.09 ± 0.05	16.9 ± 1.0
st Wt (Powheg+H++,MET <sub>200</sub> )	39.2 ± 1.0	0.62 ± 0.13	0.84 ± 0.16	0.79 ± 0.15	0.38 ± 0.10	0.08 ± 0.05	18.7 ± 1.0
st Wt (DS,MET <sub>200</sub> )	6.8 ± 0.4	0.12 ± 0.05	0.30 ± 0.09	0.23 ± 0.08	0.16 ± 0.06	0.020 ± 0.020	4.39 ± 0.4
Transfer factors (in %)							
ISR/FSR		16 ± 17	6 ± 13	9 ± 13	3 ± 18	32 ± 32	5.4 ± 1.1
PS		0 ± 30	22 ± 22	15 ± 24	0 ± 40	30 ± 70	0 ± 20
Interference (DR vs DS)		10 ± 50	60 ± 50	40 ± 50	150 ± 110	0 ± 110	35 ± 30

**Table 13.5:** Summary of the single-top theory uncertainties obtained in each of the signal regions. The uncertainties are symmetrized, and all numbers are given in percentages.

## $\bar{t} + W/Z$ THEORETICAL UNCERTAINTY

$\bar{t} + W/Z$  theoretical uncertainty include scale variations and **NNPDF3.0** PDF variations. Plus an uncertainty on the difference between  $\bar{t}\gamma$  and  $\bar{t}Z$  vector boson  $p_T$  differential cross section is added for  $\bar{t} + W/Z$  due to the procedure of using to estimate  $\bar{t} + W/Z$ . The *SHERPA*+OpenLoops is used to calculate  $\bar{t}\gamma$  and  $\bar{t}Z$  vector boson differential cross-section to NLO accuracy. The relative difference between *SHERPA*+OpenLoops and the nominal *MADGRAPH5\_AMC@NLO* cross-

sections is combined in quadrature with the scale and **NNPDF3.0** PDF variations to give the total  $t\bar{t} + W/Z$  theoretical uncertainty.

$t\bar{t} + W/Z$  theoretical uncertainty is given in table ???. The systematic uncertainty maybe large for  $t\bar{t} + W/Z$  production in the SR but  $t\bar{t} + W/Z$  comprise about 1% of our expected background. Therefore,  $t\bar{t} + W/Z$  do not contribute significantly to the total background uncertainty in the analysis.

SR	uncertainty (%)
SRA-TT	5.2
SRA-TW	4.0
SRA-To	0.8
SRB-TT	3.3
SRB-TW	5.0
SRB-To	1.2
SRC <sub>1</sub>	35.3
SRC <sub>2</sub>	5.5
SRC <sub>3</sub>	6.6
SRC <sub>4</sub>	19.7
SRC <sub>5</sub>	23.7
SRD-low	3.4
SRD-high	6.5
SRE	2.7

**Table 13.6:** Summary of the theory uncertainties (in percent) on  $t\bar{t} + W/Z$  production obtained on the transfer factor. The uncertainties are symmetries.

## DIBOSONS THEORETICAL UNCERTAINTY

A 50% uncertainty is used for the dibosons estimate because the diboson yield is predicted using MC alone.

## $Z + \text{JETS}$ THEORETICAL UNCERTAINTY

A 50% uncertainty is used for the  $Z + \text{jets}$  estimate because the  $Z + \text{jets}$  yield is predicted using MC alone.

## SIGNAL THEORETICAL UNCERTAINTY

Coming soon

# 14

## Statistical Analysis

### 14.1 INTRODUCTION TO LOG LIKELIHOOD FITTING

We check the consistency of data to predicted SM background and extract information on any potential signal using log likelihood fitting. The basic premise behind log likelihood fitting is that the parameters most likely to describe the data is the one that maximizes the total likelihood defined in equation 14.1.

$$\mathcal{L}(\vec{z}) = \prod_{i=1}^n P(x_i|\vec{z}) \quad (14.1)$$

Where  $x_i$  are data points and  $\vec{z}$  are a list of parameters, and  $P(x|\vec{z})$  is the fitted probability density function (PDF). The PDF  $P(x|\vec{z})$  have the probability of producing the a dataset  $x_i$  when the likelihood is maximized.

Maximizing the likelihood is equivalent to minimizing the negative log likelihood or NLL since logarithms are a monotonically increasing functions. Therefore, we tend to minimize the NLL  $M$  defined in equation 14.2

$$M(\vec{z}) = -\ln((\mathcal{L}(\vec{z}))) = -\sum_{i=1}^n \ln(P(x_i|\vec{z})) \quad (14.2)$$

In collider physics we do not know the total number of  $n$  events a priori. Instead, we have an expected value of events proportional to the cross-section times luminosity. This means the actual number of measured events should vary according to a poisson distribution. We include this uncertainty in the number of final observed events by multiplying a poisson distribution with expected rate  $\lambda$  to the likelihood in equation 14.1 resulting in equation 14.3.

$$\mathcal{L}(\vec{z}) = \left\{ \frac{\exp^{-\lambda}}{n!} \right\} \prod_{i=1}^n P(x_i|\vec{z}) \quad (14.3)$$

Finally, for this particular analysis we perform a binned fit to the  $R_{\text{ISR}}$  distribution in the signal region instead of an event by event shape fit. Therefore our fitted PDF ( $x_i|\vec{z}$ ) is not a full continuous

function but a series of expected values in discrete bins. Therefore  $P(x|\vec{z})$  can be written as equation 14.4.

$$P_{b_i} = P(x_i|\vec{z}) = \int_{b_{i-1}}^{b_i} f(x|\vec{z}) \, dx \quad (14.4)$$

Where  $f(x|\vec{z})$  is the continuous PDF,  $b_i$  and  $b_{i-1}$  are the bin edges for the  $i$ th bin. Assuming a poisson distribution of events in each bin, the extended likelihood and NLL becomes equation 14.5 and 14.6.

$$\mathcal{L}(N_{b_i}^{data}|\vec{z}) = \prod_{k=1}^{n_{bins}} \frac{(\lambda P_{b_i})^{N_{b_i}^{data}} e^{-\lambda P_{b_i}}}{N_{b_i}^{data}!} \quad (14.5)$$

$$\mathcal{M}(\vec{z}) = -\ln((\mathcal{L}(\vec{z})) = -\sum_{i=1}^{n_{bins}} (N_{b_i}^{data} \ln(\lambda P_{b_i}) - \lambda P_{b_i} - \ln N_{b_i}^{data}!) \quad (14.6)$$

Where  $N_{b_i}^{data}$  is the number of data in the  $i$ th bin,  $\lambda$  is the expected rate in the region,  $P_{b_i}$  is the probability of an event being in the  $i$ th bin if it is in the signal region and  $\vec{z}$  is the fitted parameters such as signal cross-section etc. Both  $\lambda$  and  $P_{b_i}$  can depend on the fitted parameters  $\vec{z}$  because the total amount and shape of background and signal can change with the fitted parameters.

A mathematically equivalent interpretation is that  $\lambda P_{b_i}$  is simply the expected number of events in a particular bin. In this case, equation 14.5 and 14.6 become 14.7 and 14.8 where  $N_{b_i}^{MC}$  is the expected number of events from simulation.

$$\mathcal{L}(N_{b_i}^{data} | \vec{z}) = \prod_{k=1}^{nbins} \frac{(N_{b_i}^{MC})^{N_{b_i}^{data}} e^{-N_{b_i}^{MC}}}{N_{b_i}^{data}!} \quad (14.7)$$

$$M(\vec{z}) = -\ln((\mathcal{L}(\vec{z})) = -\sum_{i=1}^{nbins} (N_{b_i}^{data} \ln(N_{b_i}^{MC}) - N_{b_i}^{MC} - \ln N_{b_i}^{data}!) \quad (14.8)$$

Simultaneous fits to multiple regions is performed by simultaneously maximizing the total negative log likelihood of all fitted regions. The total negative log likelihood is simply a sum of the individual likelihood of each region.

## 14.2 OVERVIEW OF FITTING TO CONTROL REGIONS AND SIGNAL REGIONS

We hope to both predict the number of expected background events and extract the amount of signal present by performing log likelihood fits to the control regions and signal region in our analysis.

We normalize backgrounds to data in control regions dominated by background but are kinematically similar to the signal region. The background normalization is allowed to float and the fit will extract the total amount of background that best describe the data in all the different control regions. All backgrounds that form a statistically significant contribution to the total background in SR has a corresponding CR. The background estimation techniques and definitions of these CRs are given in chapter 12.

The amount of MC background in both the CR and SR will fluctuate with experimental and theoretical systematics for the fit. However after the fit the total amount of background will be nor-

malized to the CR. If the raw MC yield for background fluctuate down with a given systematic then the normalization scale factor in the CR will increase. If the raw MC background yield in SR also decreases by the same amount, then the increased normalization scale factor will compensate for this and bring fitted background yield in SR remains unchanged. In this way, the control region help cancel systematic variations by directly measuring the amount of background in from data instead of relying on MC predictions.

The more kinematically similar the definition of the CR to the SR, the better the cancelation. Any extrapolation between CR and SR must only be across well modeled variables. Otherwise large systematic uncertainties will arise due to extrapolation cross poorly modeled parts of the simulation or worse the background prediction maybe wrong.

We can also check the result of our background predictions without unblinding the signal region in validation regions. Validation regions receive the normalization scale factors to background from the fit to the control region but do not participate in the fit. The VRs are designed to be kinematically similar to the SRs while keeping signal contaminations low. In this way, the VRs serves as a mid-point to check the extrapolation between CR and SR.

The relationship between CR, SR and VR is graphically depicted in figure 14.1.

In an excess were to exist in the SR, a simultaneous fit to all CR and SR is performed for to calculate the statistical significance of any potential excess in the case of discovery. If no excess were found, then a simultaneous fit to all CR and SR is also performed quantify the maximum amount of signal cross-section that can be excluded.

The background normalization and systematic uncertainty is also extracted through these simul-

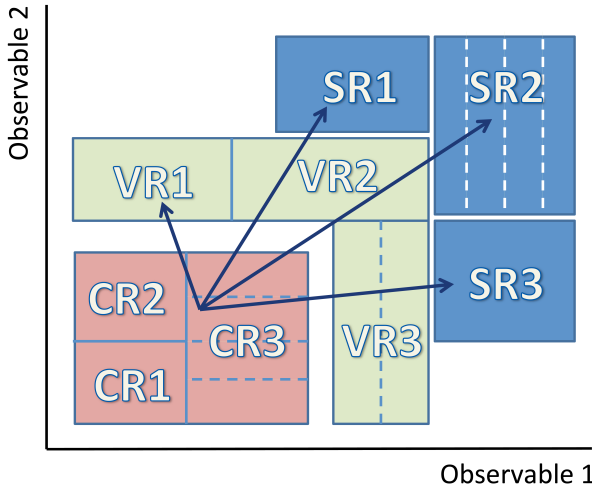


**Figure 14.1:** Basic diagram of data driven background estimation techniques. We define control regions (CR) that is dominated by background and have little signal. We can estimate the amount of background we expect in the signal region (SR) by measuring the amount of background in the CR and extrapolating to the SR using MC predictions.

taneous fit to control and signal regions.

However, the CRs have much higher statistics than the SR. Therefore, the background rate is mainly constrained by the CR and the SR mainly constrain the amount of signal. Therefore we can quantify the amount of background and the systematic uncertainty that we would expect in the signal region by performing a background only fit where only CRs are fitted. In this case, the SR behaves like another VR and is not fitted.

These three types of fits, the background only fit, the discovery fit and the exclusion fit are covered in more detail in sections 14.4 to 14.5. The parameterization of systematics as constrained nuisance parameters is covered in section 14.3.

We use the software package `HistFitter` (version `HistFitter-00-00-53`) to perform the statistical analysis.<sup>24</sup> `HistFitter` provides many tools to easily manage and integrate multiple

CR, SR backgrounds, and systematics. `HistFitter` is built upon other statistical analysis software including `RooFit`.<sup>48</sup> At its core `HistFitter` is still performing log likelihood fitting based on the principle introduced in section 14.1 but the software makes bookkeeping of the different CR, SRs and fits much more streamlined.

### 14.3 PARAMETERIZATION OF SYSTEMATICS AS GAUSSIAN CONSTRAINTS

Systematics uncertainties are parameterized as fitted parameters called nuisance parameters. The nuisance parameter, defined as  $\alpha$ , is constrained to a particular value by a constraint function  $C(\alpha)$ . The fitted PDF  $P(x|\vec{z}, \alpha)$  can depend on a number of unconstrained fitted parameter  $\vec{z}$  and the constrained  $\alpha$ . The constraint function  $C(\alpha)$  is multiplied to the likelihood as shown in equation 14.9 and contributes to the total likelihood.

$$\mathcal{L}(\vec{z}, \alpha) = \prod_{i=1}^n P(x_i|\vec{z}, \alpha) C(\alpha) \quad (14.9)$$

Now the value of  $\alpha$  corresponding to the maximum likelihood  $\mathcal{L}(\vec{z}, \alpha)$  may not be the same as value where  $C(\alpha)$  is maximized. Depending on the data points  $x_i$ , the component of the likelihood from  $\prod_{i=1}^n P(x_i|\vec{z}, \alpha)$  maybe bigger even if  $C(\alpha)$  is not at its maximum.

We pay a penalty on the total likelihood if the nuisance parameter  $\alpha$  deviates from the value with maximum  $C(\alpha)$ . The fit finds the optimal point between changing the  $\alpha$  so that the PDF best describes the data and the cost from the constraint function on  $\alpha$ .

We use Gaussians as the constraint function for all systematics. The nominal value corresponds

to  $\alpha = 0$  and the plus and minus 1 sigma deviation corresponds to  $\alpha = \pm 1$ .

Two types of systematics exist normalization and shape for our analysis. Normalizations systematics are only applied to the total normalization of the background and signal in the SR. For normalization background we determine how much the backgrounds and signal will fluctuate with the  $\pm 1$  sigma variation in systematic in each of our CRs and SR.

Shape systematics on the other allow different bins in  $R_{\text{ISR}}$  in the SR to fluctuate at different rates differently. For example a shape systematic with the  $\alpha$  value of 0.1 and have a 10 percent increase in background in bin 1 but a 15 percent increase in background in bin 2. The fluctuation in each bin is determined independently.

#### 14.4 BACKGROUND ONLY FIT AND BACKGROUND ESTIMATION

For the background only fit, the CRs are simultaneously fitted but the SR is not fitted. The backgrounds in the SR are normalized to the background normalization scale factors derived from the fit to the CRs. No signal sample is included in the fit and potential signal contamination in the CR is ignored. The background only fit is performed to estimate the background systematic uncertainties and the amount of expected background in the signal region in the absence of a signal.

The background only fit has the advantage of being able to quantify the expected amount of background and systematic uncertainties on background while the SR is blinded.

The background normalizations predicted in the background only fit may differ from the discovery and exclusion fits because the SR is simultaneously fitted in those fits. This difference should be

small as long as the CRs are well designed and have much higher constraining power on the amount of background than the SR. The CRs that have high purity in a single background and high statistics will have much stronger constraining power on the amount of background than the lower statistics SR.

#### 14.5 EXCLUSION FIT AND EXCLUSION LIMIT CALCULATION

The exclusion fit is performed as a simultaneous fit to all CRs and SR. The signal sample is included in both CR and SR and normalized to a signal strength parameter. The signal strength parameter can be varied but is constrained to be non-negative. The five bins in  $R_{\text{ISR}}$  is simultaneously fitted in the SR for exclusion.

The best fit signal strength is found when the negative log likelihood (NLL) is at a minimum after fitting to data. As the signal strength deviates from the best fit value, the NLL increases and we are more confident that the signal strength is not supported by data. The NLL's variation and the statistical significance should be related to one another by a parabola if the statistics in SR is high enough. The signal strength corresponding to when the NLL is 1 above the minimum NLL corresponds to the 1 sigma confidence interval on signal strength. The signal strength corresponding to when the NLL is 4 above the minimum NLL corresponds to the 2 sigma confidence interval on signal strength and so on.

In other words, we use the difference in NLL as our test statistic and the relationship between the test statistic and statistical significance approaches the asymptotic case of a parabola at high

statistics.

In this way we can find the 95 percent confidence interval on the signal cross-section. If the high end of the 95 percent confidence interval on signal cross-section is less than the production cross-section of a particular signal model then that signal model has been excluded to at least 95 confidence.

Alternatively we can calculate the NLL corresponding to the nominal signal strength of each signal model and compare it with the fitted minimum NLL. The difference in the two NLLs can be converted into the statistical significance using the parabolic relationship between the two. The statistical significance of the nominal signal strength for a particular model is the exclusion p-value for the model. If the exclusion p-value is below 5 percent then the signal model has been excluded to 95 confidence.

We calculate the exclusion p-value corresponding to a grid of signal models each with a different stop and neutralino mass. The p-values are plotted in a 2D graph with the stop mass along the x-axis and the neutralino mass along the y-axis. These p-values are then interpolated over to form a 2D contour plot. The contour corresponding to the 95 percent exclusion limit is then drawn.

#### 14.6 DISCOVERY FIT AND DISCOVERY SIGNIFICANCE CALCULATION

The discovery fit is also performed as a simultaneous fit to all CRs and SR. The signal sample is included only in the SR but not to the CR in the fit. This choice of excluding the signal sample from the CR gives a more conservative estimate of the discovery significance. If a signal is present in na-

ture, the signal contamination in the CR would still exist in data. We essentially over-estimate the amount of background by counting any potential signal contamination in the CR as background. Again, a well designed CR has little signal contamination so the difference between this approach and exclusion fit should be small. Our signal contamination is less than 15 percent for all signal samples that we are sensitive to but have not been excluded by previous 8 TeV ATLAS analysis. The signal contamination is less than 10 percent for all stop masses above 300 GeV.

We do not statically combine the 5  $R_{\text{ISR}}$  bins for the discovery fit. Instead a single  $R_{\text{ISR}}$  bin is fitted at a time and the bin with the best significance is used as the discovery significance for the signal model. Again this is a conservative approach and gives us worse discovery significances but it makes the analysis less sensitive to shape uncertainties in signal.

We also use the difference in NLL as our test static for our discovery fit. The signal strength and background normalization that best fit the data is found at the minimum NLL. Then we calculate the NLL with a signal strength of zero. The difference between the NLL with a signal strength of zero and the best fit NLL is our test statistic. The relationship between the test statistic is given by a parabola in the asymptotic high statistics case. We assume we are in the asymptotic case and derive the statistic significance of the zero signal strength fit.

The statistical significance of the zero signal strength fit represent the amount of disagreement between data and the no signal case. In other words, the statistical significance of the zero signal strength fit is the p-value of the no signal hypothesis test. This p-value is the discovery significance for the analysis. If the discovery significance is above 5 sigma then discovery can be claimed.

# 15

## Results

Unblinded signal region distributions of the kinematic variables with the most discrimination power are shown in figure 15.1. The plots correspond to  $36.47 \text{ fb}^{-1}$  of data. The expected background yield have been normalized to all control regions using the background only fitting procedure described in section 14.4.

Signal region yields with  $36.47 \text{ fb}^{-1}$  of data can be seen in table 15.1 and 15.2. No significant excess

SRC yields	SRC <sub>1</sub>	SRC <sub>2</sub>	SRC <sub>3</sub>
Observed events	20	22	22
Fitted bkg events	$20.56 \pm 6.62$	$27.54 \pm 4.89$	$18.86 \pm 3.53$
Fitted TTbar events	$12.85 \pm 5.87$	$22.05 \pm 4.19$	$14.57 \pm 3.23$
Fitted Wjets events	$0.81 \pm 0.37$	$1.93 \pm 0.48$	$1.91 \pm 0.63$
Fitted Zjets events	$0.00 \pm 0.00$	$0.00 \pm 0.00$	$0.00 \pm 0.00$
Fitted TtbarV events	$0.29 \pm 0.18$	$0.59 \pm 0.38$	$0.56 \pm 0.31$
Fitted SingleTop events	$1.67^{+2.02}_{-1.67}$	$1.18^{+1.81}_{-1.18}$	$1.22^{+1.37}_{-1.22}$
Fitted Diboson events	$0.39 \pm 0.33$	$0.21 \pm 0.11$	$0.29 \pm 0.18$
Fitted Multijets events	$4.56 \pm 2.38$	$1.58 \pm 0.77$	$0.32 \pm 0.17$
MC exp. SM events	$25.44 \pm 8.64$	$35.98 \pm 6.11$	$24.21 \pm 4.34$
MC exp. TTbar events	$18.19 \pm 8.07$	$31.20 \pm 5.41$	$20.62 \pm 4.14$
MC exp. Wjets events	$0.64 \pm 0.29$	$1.53 \pm 0.32$	$1.51 \pm 0.44$
MC exp. Zjets events	$0.00 \pm 0.00$	$0.00 \pm 0.00$	$0.00 \pm 0.00$
MC exp. TtbarV events	$0.22 \pm 0.14$	$0.46 \pm 0.28$	$0.44 \pm 0.23$
MC exp. SingleTop events	$1.44^{+1.66}_{-1.44}$	$1.02^{+1.54}_{-1.02}$	$1.04^{+1.11}_{-1.04}$
MC exp. Diboson events	$0.39 \pm 0.33$	$0.21 \pm 0.11$	$0.28 \pm 0.18$
MC exp. Multijets events	$4.56 \pm 2.38$	$1.58 \pm 0.77$	$0.32 \pm 0.17$

**Table 15.1:** Region: SRC. Background-only fit results for an integrated luminosity of  $36.07 \text{ fb}^{-1}$ . The uncertainties are statistical and systematic.

is observed in any region. An under fluctuation of background is observed in the  $R_{\text{ISR}}$  bin between  $0.6 - 0.7$  but is not statistically significant due to the low amount of expected events.

95 percent upper confidence limits on the observed cross-section ( $\langle \varepsilon \sigma \rangle_{\text{obs}}^{95}$ ) and on the number of signal events ( $S_{\text{obs}}^{95}$ ) in each  $R_{\text{ISR}}$  bin is shown in table 15.3. Observed limits are derived using the discovery fit procedure described in section 14.6. Discovery p-values are calculated using the asymptotic assumption.

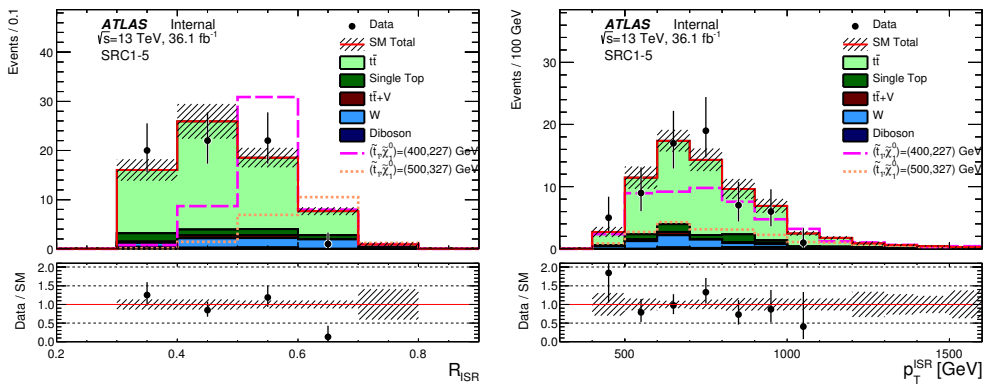


**Figure 15.1:** Unblinded  $R_{\text{ISR}}$  and  $p_T^{\text{ISR}}$  distributions for SRC1-5 for  $36.47 \text{ fb}^{-1}$ .

SRC yields	SRC4	SRC5
Observed events	I	O
Fitted bkg events	$7.69 \pm 1.37$	$0.90 \pm 0.71$
Fitted TTbar events	$4.92 \pm 0.98$	$0.63^{+0.69}_{-0.63}$
Fitted Wjets events	$1.93 \pm 0.45$	$0.21 \pm 0.12$
Fitted Zjets events	$0.00 \pm 0.00$	$0.00 \pm 0.00$
Fitted TtbarV events	$0.08 \pm 0.08$	$0.06 \pm 0.03$
Fitted SingleTop events	$0.72^{+0.77}_{-0.72}$	$0.00 \pm 0.00$
Fitted Diboson events	$0.00 \pm 0.00$	$0.00 \pm 0.00$
Fitted Multijets events	$0.04 \pm 0.02$	$0.00 \pm 0.00$
MC exp. SM events	$9.20 \pm 1.60$	$1.11 \pm 0.99$
MC exp. TTbar events	$6.95 \pm 1.37$	$0.89^{+0.97}_{-0.89}$
MC exp. Wjets events	$1.53 \pm 0.34$	$0.17 \pm 0.09$
MC exp. Zjets events	$0.00 \pm 0.00$	$0.00 \pm 0.00$
MC exp. TtbarV events	$0.07 \pm 0.06$	$0.05 \pm 0.02$
MC exp. SingleTop events	$0.62^{+0.64}_{-0.62}$	$0.00 \pm 0.00$
MC exp. Diboson events	$0.00 \pm 0.00$	$0.00 \pm 0.00$
MC exp. Multijets events	$0.04 \pm 0.02$	$0.00 \pm 0.00$

**Table 15.2:** Region: SRC. Background-only fit results for an integrated luminosity of  $36.07 \text{ fb}^{-1}$ . The uncertainties are statistical and systematic.

Signal channel	$\langle \varepsilon\sigma \rangle_{\text{obs}}^{95} [\text{fb}]$	$S_{\text{obs}}^{95}$	$S_{\text{exp}}^{95}$	$CL_B$	$p(s = o) (Z)$
SRC <sub>1</sub>	0.44	16.0	16.3 <sup>+5.8</sup> <sub>-4.2</sub>	0.47	0.50 (0.00)
SRC <sub>2</sub>	0.35	12.6	15.5 <sup>+5.9</sup> <sub>-4.2</sub>	0.26	0.50 (0.00)
SRC <sub>3</sub>	0.44	15.8	12.8 <sup>+4.7</sup> <sub>-2.7</sub>	0.69	0.30 (0.54)
SRC <sub>4</sub>	0.09	3.1	6.5 <sup>+3.3</sup> <sub>-2.1</sub>	0.02	0.50 (0.00)
SRC <sub>5</sub>	0.06	2.2	2.8 <sup>+2.0</sup> <sub>-1.1</sub>	0.32	0.49 (0.02)

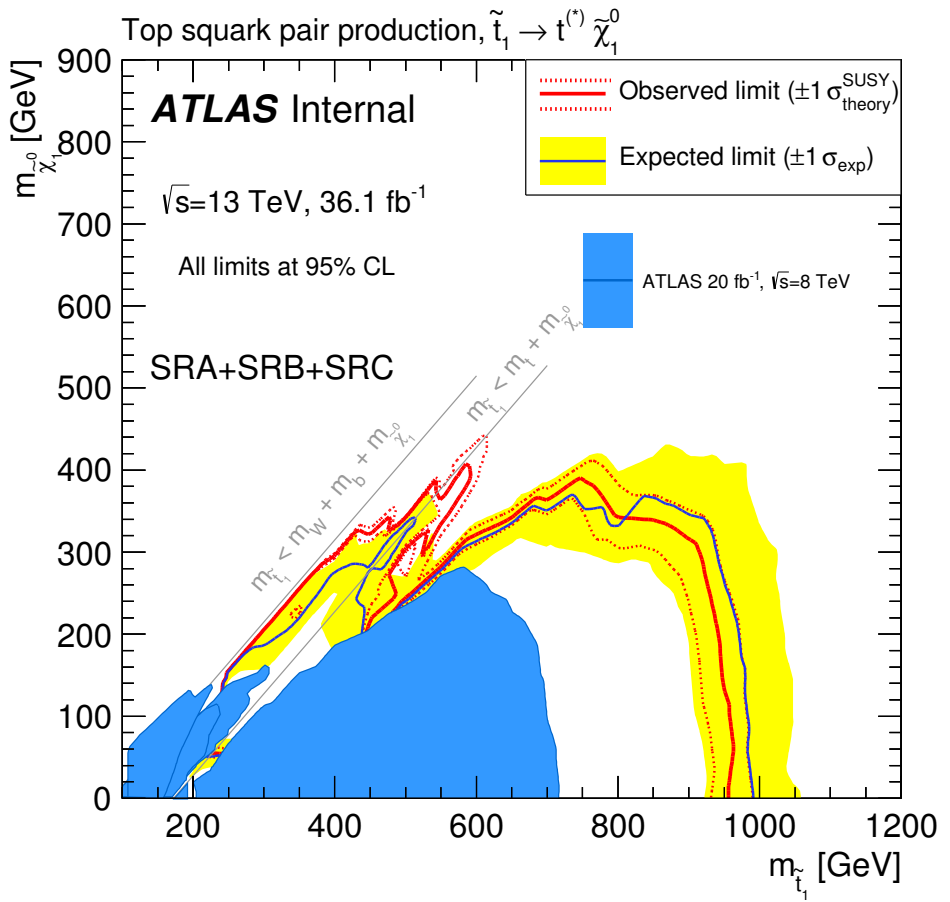
**Table 15.3:** Left to right: 95% CL upper limits on the visible cross section ( $\langle \varepsilon\sigma \rangle_{\text{obs}}^{95}$ ) and on the number of signal events ( $S_{\text{obs}}^{95}$ ). The third column ( $S_{\text{exp}}^{95}$ ) shows the 95% CL upper limit on the number of signal events, given the expected number (and  $\pm 1\sigma$  excursions on the expectation) of background events. The last two columns indicate the  $CL_B$  value, i.e. the confidence level observed for the background-only hypothesis, and the discovery  $p$ -value ( $p(s = o)$ ).

# 16

## Interpretation of Results

Since no significant excesses were observed in the signal region, the results are interpreted as exclusions on stop parameter space. The 95% confidence observed and expected exclusion limit is shown in figure 16.1. The exclusion p-values are derived using the exclusion fit procedure described in section 14.5 where all 5 bins in  $R_{\text{ISR}}$  are simultaneously fitted and statistically combined.

Previous 8 TeV stop exclusion limits are shown in blue for comparison.



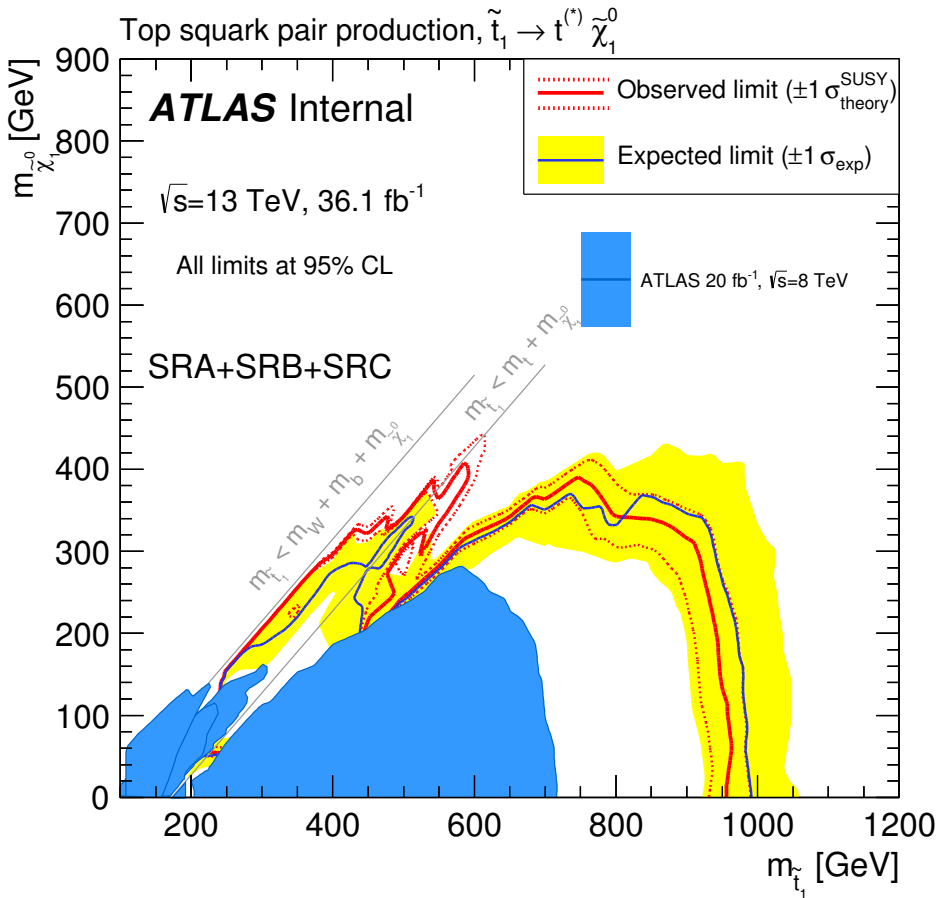
**Figure 16.1:** Results of the exclusion fits in the tN1 grid from a simultaneous fit to the compressed analysis SR

Figure 16.2 shows the compressed stop analysis exclusion limit combined with the bulk region 13 TeV stop o lepton analysis exclusion limit. The bulk stop o lepton analysis targets the high stop masses parameter space with larger mass splitting between stop and neutralino masses. In regions with large mass splitting between stop and neutralinos, the stop decay gives a large amount of momenta to the resulting neutralinos and therefore we expect a large of amount  $E_T^{\text{miss}}$  in signal. The bulk region analysis builds kinematic variables such as  $m_{\text{eff}}$  that uses the large amount of  $E_T^{\text{miss}}$  to separate signal from background. A detail description of the bulk region stop o lepton analysis can be found here<sup>2</sup>.

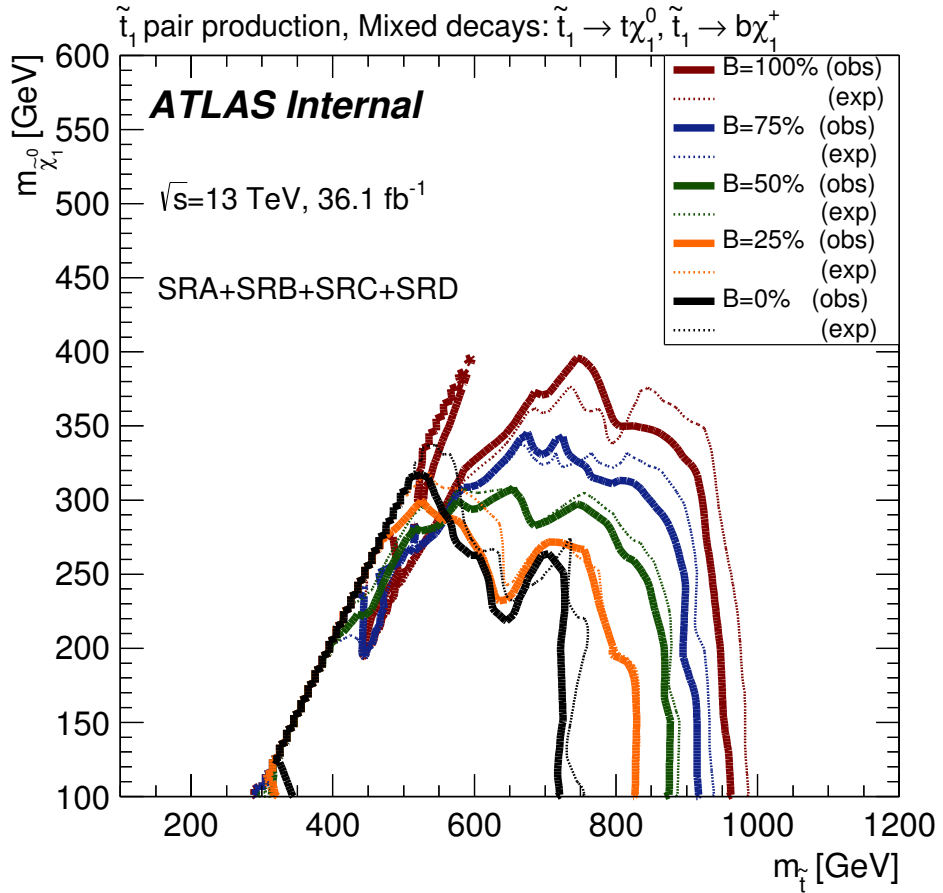
The compressed analysis is exclusively responsible for the exclusion of all stop masses from 225 GeV to 600 GeV along the  $\Delta m = m_t$  diagonal line. We can see the bulk region analysis's sensitivity decrease as the  $\Delta m$  decrease to  $\sim m_t$ .

Figure 16.3 show how the exclusion limit on the stop, neutralino parameter space plane as the branching fraction to  $\tilde{t} \rightarrow t + \tilde{\chi}_1^0$  change from 100% to 0%. As the  $\tilde{t} \rightarrow t + \tilde{\chi}_1^0$  branching fraction decreases, the  $\tilde{t} \rightarrow b + \tilde{\chi}_1^\pm$  branching fraction increases. Another signal region directly targeting the  $\tilde{t} \rightarrow b + \tilde{\chi}_1^\pm$  decay channel SRD is added. Detailed documentation on the mixed decay analysis can also be found in<sup>3</sup>.

Again the compressed analysis is exclusively responsible for the exclusion of all stop parameter space along the  $\Delta m = m_t$  diagonal line when branching fraction to  $\tilde{t} \rightarrow t + \tilde{\chi}_1^0$  is high.



**Figure 16.2:** Results of the exclusion fits in the tN1 grid from the combination of the bulk region stop OL analysis (SRA+SRB) and the compressed analysis (SRC). The bulk region analysis SRA targets high stop masses with large  $\Delta m$  and SRB targets high stop masses with medium amount of  $\Delta m$ . SRC is the compressed region analysis and adds sensitivity to the  $\Delta m = m_t$  diagonal region where SRA and SRB lack sensitivity.



**Figure 16.3:** Results of the exclusion fits in the grid with two stop decay channels:  $\tilde{t} \rightarrow t\tilde{\chi}_1^0$  and  $\tilde{t} \rightarrow b\tilde{\chi}_1^\pm \rightarrow bW^{(*)}\tilde{\chi}_1^0$ , with  $m(\tilde{\chi}_1^\pm) - m(\tilde{\chi}_1^0) = 1 \text{ GeV}$ . The results are shown as a function of the branching ratio to  $\tilde{t} \rightarrow t\tilde{\chi}_1^0$ : 0%, 25%, 50%, 75% and 100%. The results are based on taking the signal region with the best expected  $CL_s$ , using SRA, SRB, SRC, and SRD. SRA and SRB target high stop masses in the  $\tilde{t} \rightarrow t\tilde{\chi}_1^0$  decay channel at high stop masses and moderate to large  $\Delta m$ . SRC is the compressed region analysis that targets  $\tilde{t} \rightarrow t\tilde{\chi}_1^0$  with  $\Delta m \sim m_t$ . SRD targets a mix decay channel with branching fraction to both  $\tilde{t} \rightarrow t\tilde{\chi}_1^0$  and  $\tilde{t} \rightarrow b\tilde{\chi}_1^\pm \rightarrow bW^{(*)}\tilde{\chi}_1^0$ . We can see that the compressed analysis SRC adds sensitivity to the  $\Delta m = m_t$  line when the branching fraction is mainly to  $\tilde{t} \rightarrow t\tilde{\chi}_1^0$ .

# 17

## Conclusion

We performed a search for the superpartner to the top quark using  $36.47 \text{ fb}^{-1}$  of 13 TeV LHC data collected by the ATLAS detector. The analysis was able to rule out stops between masses of 225 and 600 GeV if the  $m_{\tilde{t}} - m_{\text{ninoone}} = m_t$  and the stop decayed with 100 percent branching ratio to  $\tilde{t} \rightarrow \tilde{\chi}_1^0 + t$ . No previous analysis was able to gain sensitivity to this experimentally difficult region of phase space. Traditional analysis strategy that focused on large amounts of  $E_T^{\text{miss}}$  failed due

to low momenta imparted onto the neutralinos from the stop decays alone. The lack of  $E_T^{\text{miss}}$  made distinguishing between stops and the dominant SM ttbar background difficult. We demonstrated that by targeting events with strong initial state radiation and using the correlations between ISR and  $E_T^{\text{miss}}$  we are able to separate signal from ttbar and other SM background. Specifically the ratio between  $E_T^{\text{miss}}$  and ISR  $p_T$  called  $R_{\text{ISR}}$  was found to peak at  $m_{\text{ninoone}}/m_{\tilde{t}}$  for signal. The spread of the peak is only 8 percent including detector resolution effects.

As part of this project, we developed a new and extremely accurate ISR identification algorithm. We were able to achieve 9 percent uncertainty on ISR  $p_T$  in both signal and ttbar background if the event contained at least 400 GeV of true ISR pt. The uncertainty includes detector resolution effects and is derived using Monte Carlo simulation. The algorithm uses the axis of maximum back to back  $p_T$  called the thrust axis, to separate the event into an ISR hemisphere and a sparticle hemisphere. In events with strong ISR, the back to back recoil between the particles produced in the hard scattering event and ISR should represent the single largest back to back kick in the event. Therefore, the axis of maximum back to back  $p_T$ , the thrust axis, will mimic the axis of the back to back recoil between the particles produced in the hard scattering interaction and the total ISR system. The method is completely generalizable for both exotic signal and SM background. For stop signal, the thrust axis approximates the axis of recoil between the stops and the ISR. For ttbar produced with strong ISR, the thrust axis approximates the recoil between ttbar and ISR.

Using properties of both the sparticle and ISR hemispheres and the correlation between ISR and  $E_T^{\text{miss}}$  in signal we are able to achieve better than 2 to 1 signal to background for stop masses between 250 and 400 GeV. The background is 70-90 percent SM ttbar depending on the  $R_{\text{ISR}}$  region. The

signal region specifically targets events with strong ISR in both signal and background and 90 percent of all ttbar which survives the signal region selection have  $> 500$  GeV of true ISR pt. Other background include  $W+jets$ ,  $Z+jets$ , and single top at high  $R_{ISR}$  and QCD multijet at low  $R_{ISR}$ .

Total background systematics are between 15-25 percent in bins with appreciable expected background statistics. Of this only 10 percent is associated with the systematic uncertainty on ISR/FSR generation on ttbar. The low ISR/FSR systematic uncertainty is due to the control region in ttbar which directly estimates the amount of ttbar plus strong ISR pt. There is no extrapolation across ISR pt between CR and SR and the distributions of true ISR pt is nearly identical between SR and CR for SM ttbar. The other largest systematic uncertainties include uncertainties on ttbar matrix element and parton shower calculations and theory uncertainty between the interference of SM single top and SM ttbar, each at about 10 percent. The uncertainty on ISR and partons showers are also small due to the fact that the ISR identification algorithm identifies entire ISR systems instead of individual jets. As such, the algorithm is insensitive to uncertainties associated with an ISR parton splitting into multiple jets during fragmentation and hadronization.

This analysis serves also as a demonstration of the general strategy of using events with strong ISR to search for exotic signatures with  $E_T^{\text{miss}}$ . There will always be strong correlation between ISR and  $E_T^{\text{miss}}$  as long as a particle's decay products gain little  $p_T$  from the particle decay alone. ISR identification algorithm is also completely generalizable because the thrust axis will mimic the back to back recoil between ISR and any particles so long as the ISR is strong enough to represent the largest single back to back kick in the event. This gives potential application to other searches in SUSY and exotic particles searches including searches on Higgsinos, Charginos, and other ISR assisted searches

such as monojet searches for dark-matter. Even if the algorithm doesn't improve separation power between signal and background when compared to other ISR based searches, we still expect to have significantly smaller ISR/FSR uncertainty because the ISR algorithm identifies entire ISR systems and is insensitive to uncertainties associated with a hard ISR parton splitting into multiple jets.

At the same time, the accurate ISR identification algorithm can also be used to identify SM processes with strong ISR  $p_T$ . The algorithm is able to separate ttbar produced with at least 500 GeV of ISR  $p_T$  from ttbar with little ISR  $p_T$  as demonstrated in the SM ttbar CR. This represents a new method to measure SM differential cross-sections. Current ttbar ISR  $p_T$  differential cross-section measurements at ATLAS first attempt to reconstruct tops and identify all non-top jets as ISR jets. Hadronic top reconstruction efficiency is extremely correlated with top  $p_T$  with a top reconstruction efficiency of only 30% at top  $p_T = 200$  GeV. This means that ttbar ISR  $p_T$  measurements that require the reconstruction of tops are inherently biased towards events with high hadronic top  $p_T$ .

Because the ISR algorithm primarily uses the thrust axis and properties of the entire di-top system, we can avoid reconstructing individual tops but still identify a region with high purity of ttbar plus strong ISR. This gives a more independent measurement of the ttbar ISR  $p_T$  distribution and avoids any top reconstruction inefficiencies.

# A

## Sanity Checks

# References

[IBL]

- [2] (2010). *Properties of Jets and Inputs to Jet Reconstruction and Calibration with the ATLAS Detector Using Proton-Proton Collisions at  $\sqrt{s} = 7 \text{ TeV}$* . Technical Report ATLAS-CONF-2010-053, CERN, Geneva.
- [3] (2013). *Pile-up subtraction and suppression for jets in ATLAS*. Technical Report ATLAS-CONF-2013-083, CERN, Geneva.
- [4] (2014). *ATLAS Run 1 Pythia8 tunes*. Technical Report ATL-PHYS-PUB-2014-021, CERN, Geneva.
- [5] (2014). *Tagging and suppression of pileup jets with the ATLAS detector*. Technical Report ATLAS-CONF-2014-018, CERN, Geneva.
- [6] (2015a). *Data-driven determination of the energy scale and resolution of jets reconstructed in the ATLAS calorimeters using dijet and multijet events at  $\sqrt{s} = 8 \text{ TeV}$* . Technical Report ATLAS-CONF-2015-017, CERN, Geneva.
- [7] (2015b). *Determination of the jet energy scale and resolution at ATLAS using  $Z/\gamma$ -jet events in data at  $\sqrt{s} = 8 \text{ TeV}$* . Technical Report ATLAS-CONF-2015-057, CERN, Geneva.
- [8] (2015). *Expected performance of missing transverse momentum reconstruction for the ATLAS detector at  $\sqrt{s} = 13 \text{ TeV}$* . Technical Report ATL-PHYS-PUB-2015-023, CERN, Geneva.
- [9] (2015). *Expected performance of the ATLAS b-tagging algorithms in Run-2*. Technical Report ATL-PHYS-PUB-2015-022, CERN, Geneva.
- [10] (2015). *Jet global sequential corrections with the ATLAS detector in proton-proton collisions at  $\sqrt{s} = 8 \text{ TeV}$* . Technical Report ATLAS-CONF-2015-002, CERN, Geneva.
- [11] (2015). *Monte Carlo Calibration and Combination of In-situ Measurements of Jet Energy Scale, Jet Energy Resolution and Jet Mass in ATLAS*. Technical Report ATLAS-CONF-2015-037, CERN, Geneva.

- [12] (2015). *Properties of Jets and Inputs to Jet Reconstruction and Calibration with the ATLAS Detector Using Proton-Proton Collisions at  $\sqrt{s} = 13$  TeV*. Technical Report ATL-PHYS-PUB-2015-036, CERN, Geneva.
- [13] (2015). *Selection of jets produced in 13 TeV proton-proton collisions with the ATLAS detector*. Technical Report ATLAS-CONF-2015-029, CERN, Geneva.
- [14] (2015). *Vertex Reconstruction Performance of the ATLAS Detector at  $\sqrt{s} = 13$  TeV*. Technical Report ATL-PHYS-PUB-2015-026, CERN, Geneva.
- [15] (2016). *Electron and photon energy calibration with the ATLAS detector using data collected in 2015 at  $\sqrt{s} = 13$  TeV*. Technical Report ATL-PHYS-PUB-2016-015, CERN, Geneva.
- [16] (2016). *Electron efficiency measurements with the ATLAS detector using the 2015 LHC proton-proton collision data*. Technical Report ATLAS-CONF-2016-024, CERN, Geneva.
- [17] (2016). *Optimisation of the ATLAS b-tagging performance for the 2016 LHC Run*. Technical Report ATL-PHYS-PUB-2016-012, CERN, Geneva.
- [18] (2016). *Photon identification in 2015 ATLAS data*. Technical Report ATL-PHYS-PUB-2016-014, CERN, Geneva.
- [19] (2016). *Prospects for a search for direct pair production of top squarks in scenarios with compressed mass spectra at the high luminosity LHC with the ATLAS Detector*. Technical Report ATL-PHYS-PUB-2016-022, CERN, Geneva.
- [20] (2017). *Trigger Menu in 2016*. Technical Report ATL-DAQ-PUB-2017-001, CERN, Geneva.
- [21] Achenbach, R., Adragna, P., Andrei, V., Apostologlou, P., Åsman, B., Ay, C., Barnett, B. M., Bauss, B., Bendel, M., Bohm, C., Booth, J. R. A., Brawn, I. P., Thomas, P. B., Charlton, D. G., Collins, N. J., Curtis, C. J., Dahlhoff, A., Davis, A. O., Eckweiler, S., Edwards, J. P., Eisenhandler, E., Faulkner, P. J. W., Fleckner, J., Föhlisch, F., Garvey, J., Gee, C. N. P., Gillman, A. R., Hanke, P., Hatley, R. P., Hellman, S., Hidvégi, A., Hillier, S. J., Jakobs, K., Johansen, M., Kluge, E. E., Landon, M., Lendermann, V., Lilley, J. N., Mahboubi, K., Mahout, G., Mass, A., Meier, K., Moa, T., Moyse, E., Müller, F., Neusiedl, A., Nöding, C., Oltmann, B., Pentney, J. M., Perera, V. J. O., Pfeiffer, U., Prieur, D. P. F., Qian, W., Rees, D. L., Rieke, S., Rühr, F., Sankey, D. P. C., Schäfer, U., Schmitt, K., Schultz-Coulon, H. C., Schumacher,

- C., Silverstein, S., Staley, R. J., Stamen, R., Stockton, M. C., Tapprogge, S., Thomas, J. P., Treffzger, T., Watkins, P. M., Watson, A., Weber, P., & Woehrling, E. E. (2008). The atlas level-1 calorimeter trigger. *Journal of Instrumentation*, 3(03), Po3001.
- [22] An, H. & Wang, L.-T. (2015). Opening up the compressed region of top squark searches at 13 tev lhc. *Phys. Rev. Lett.*, 115, 181602.
- [23] Ball, R. D., Bertone, V., Carrazza, S., Deans, C. S., Del Debbio, L., Forte, S., Guffanti, A., Hartland, N. P., Latorre, J. I., Rojo, J., & Ubiali, M. (2015). Parton distributions for the lhc run ii. *Journal of High Energy Physics*, 2015(4), 40.
- [24] Besjes, G. J., Baak, M., Côté, D., Koutsman, A., Lorenz, J. M., & Short, D. (2015). Histfitter: a flexible framework for statistical data analysis. *Journal of Physics: Conference Series*, 664(7), 072004.
- [25] Borschensky, C., Krämer, M., Kulesza, A., Mangano, M., Padhi, S., Plehn, T., & Portell, X. (2014). Squark and gluino production cross sections in pp collisions at  $\sqrt{s} = 13, 14, 33$  and 100 tev. *Eur. Phys. J.*, C74(12), 3174.
- [26] Cacciari, M., Salam, G. P., & Soyez, G. (2008). The catchment area of jets. *Journal of High Energy Physics*, 2008(04), 005.
- [27] Capeans, M., Darbo, G., Einsweiller, K., Elsing, M., Flick, T., Garcia-Sivieres, M., Gemme, C., Pernegger, H., Rohne, O., & Vuillermet, R. (2010). *ATLAS Insertable B-Layer Technical Design Report*. Technical Report CERN-LHCC-2010-013. ATLAS-TDR-19.
- [28] Collaboration, A. (2014). Electron and photon energy calibration with the atlas detector using lhc run i data. *The European Physical Journal C*, 74(10), 3071.
- [29] Collaboration, A. (2016a). Measurements of the higgs boson production and decay rates and constraints on its couplings from a combined atlas and cms analysis of the lhc pp collision data at  $\sqrt{s} = 7$  and 8 tev. *Journal of High Energy Physics*, 2016(8), 45.
- [30] Collaboration, A. (2016b). Muon reconstruction performance of the atlas detector in proton–proton collision data at  $\sqrt{s} = 13$  tev. *The European Physical Journal C*, 76(5), 292.
- [31] Collaboration, A. (2016c). *Performance of the ATLAS Trigger System in 2015*. Technical Report arXiv:1611.09661. CERN-EP-2016-241, CERN, Geneva.

Comments: 76 pages in total, author list starting page 60, 50 figures, 1 table. Submitted to Eur. Phys. J. C. All figures including auxiliary figures are available at <http://atlas.web.cern.ch/Atlas/GROUPS/PHYSICS/PAPERS/TRIG-2016-01/>.

- [32] Collaboration, T. A. (2008). The atlas experiment at the cern large hadron collider. *Journal of Instrumentation*, 3(08), S08003.
- [33] Cornelissen, T., Elsing, M., Fleischmann, S., Liebig, W., Moyse, E., & Salzburger, A. (2007). *Concepts, Design and Implementation of the ATLAS New Tracking (NEWT)*. Technical Report ATL-SOFT-PUB-2007-007. ATL-COM-SOFT-2007-002, CERN, Geneva.
- [34] Czakon, M. & Mitov, A. (2014). Top++: A Program for the Calculation of the Top-Pair Cross-Section at Hadron Colliders. *Comput. Phys. Commun.*, 185, 2930.
- [35] Evans, L. & Bryant, P. (2008). LHC Machine. *JINST*, 3, S08001.
- [36] Fruhwirth, R., Waltenberger, W., & Vanlaer, P. (2007). Adaptive vertex fitting. *J. Phys.*, G34, N343.
- [37] Hoecker, A., Speckmayer, P., Stelzer, J., Therhaag, J., von Toerne, E., Voss, H., Backes, M., Carli, T., Cohen, O., Christov, A., Dannheim, D., Danielowski, K., Henrot-Versille, S., Jachowski, M., Kraszewski, K., Krasznahorkay, Jr., A., Kruk, M., Mahalalel, Y., Ospanov, R., Prudent, X., Robert, A., Schouten, D., Tegenfeldt, F., Voigt, A., Voss, K., Wolter, M., & Zemla, A. (2007). TMVA - Toolkit for Multivariate Data Analysis. *ArXiv Physics e-prints*.
- [38] Illingworth, J. & Kittler, J. (1988). A survey of the hough transform. *Computer Vision, Graphics, and Image Processing*, 44(1), 87 – 116.
- [39] Jackson, P., Rogan, C., & Santoni, M. (2017a). Sparticles in motion: Analyzing compressed susy scenarios with a new method of event reconstruction. *Phys. Rev. D*, 95, 035031.
- [40] Jackson, P., Rogan, C., & Santoni, M. (2017b). Sparticles in motion: Analyzing compressed susy scenarios with a new method of event reconstruction. *Phys. Rev. D*, 95, 035031.
- [41] Lai, H.-L., Guzzi, M., Huston, J., Li, Z., Nadolsky, P. M., Pumplin, J., & Yuan, C.-P. (2010). New parton distributions for collider physics. *Phys. Rev. D*, 82, 074024.
- [42] Macaluso, S., Park, M., Shih, D., & Tweedie, B. (2016). Revealing compressed stops using high-momentum recoils. *Journal of High Energy Physics*, 2016(3), 151.

- [43] Martin, S. P. (1997). A Supersymmetry primer. [Adv. Ser. Direct. High Energy Phys.18,1(1998)].
- [44] Owen, S. (2012). *Data-driven estimation of the QCD multijet background to SUSY searches with jets and missing transverse momentum at ATLAS using jet smearing*. Technical Report ATL-PHYS-INT-2012-008, CERN, Geneva.
- [45] Pequenao, J. & Schaffner, P. (2013). An computer generated image representing how ATLAS detects particles.
- [46] Pumplin, J., Stump, D. R., Huston, J., Lai, H.-L., Nadolsky, P., & Tung, W.-K. (2002). New generation of parton distributions with uncertainties from global qcd analysis. *Journal of High Energy Physics*, 2002(07), 012.
- [47] Skands, P. Z. (2010). Tuning monte carlo generators: The perugia tunes. *Phys. Rev. D*, 82, 074018.
- [48] Verkerke, W. & Kirkby, D. (2003). The rooffit toolkit for data modeling. *eConf*, C0303241, MOLT007.